IMPROVED UNDERSTANDING OF EXTENT AND SIZE OF TSUNAMIGENIC EARTHQUAKES THROUGH GEODETIC AND TSUNAMI DATASETS

A Dissertation
Presented to
The Academic Faculty

by

Amy L. Williamson

In Partial Fulfillment
of the Requirements for the Degree
Doctor of Philosophy in the
School of Earth and Atmospheric Sciences

Georgia Institute of Technology
May 2018

IMPROVED UNDERSTANDING OF EXTENT AND SIZE OF TSUNAMIGENIC EARTHQUAKES THROUGH GEODETIC AND TSUNAMI DATASETS

Approved by:

Dr. Andrew Newman, Advisor
School of Earth and Atmospheric Sciences
Georgia Institute of Technology

Dr. Hermann Fritz
School of Civil and Environmental Engineering
Georgia Institute of Technology

Dr. Zhigang Peng
School of Earth and Atmospheric Sciences
Georgia Institute of Technology

Dr. Phil Cummins
Research School of Earth Sciences
Australian National University

Dr. Ken Ferrier
School of Earth and Atmospheric Sciences
Georgia Institute of Technology

Date Approved: March 16th, 2018

In loving memory of Nancy Snider

ACKNOWLEDGEMENTS

I am incredibly grateful for the research and teaching opportunities that I have received during my PhD and want first to express gratitude to my advisor, Andy Newman for all of the encouragement that he has provided over the past five years. I am especially grateful to him for promoting a research independence and curiosity over my research topic. I also want to express gratitude to the rest of my dissertation committee: Zhigang Peng, Phil Cummins, Hermann Fritz, and Ken Ferrier for their time and their valuable feedback on this dissertation and their support over my time here at Georgia Tech.

I am also thankful for my friends in the department who made Atlanta home. A special thanks to Tiegan Hobbs for all your motivational pep talks and friendship, even when I broke the air conditioning in the office to replicate dry season in Costa Rica. Thank you, Lucas Liuzzo for all your support and for putting up with many early morning and long nights talking about my project. I also want to thank Louisa Barama, Jacob Buffo, Hamid Karani, Justin D. Lawrence, Chenyu Li, Emily Saad, and the rest of the Seismo-tectonics group for their support and friendship through this process.

Lastly, I would like to thank my family for their support over the past few years. To my mom and dad, thank you for always encouraging me and pushing me to try new things, travel to new places, and pursue my dreams. I would not be where I am today if it were not for you.

TABLE OF CONTENTS

LIST OF FIGURES

SUMMARY

Some of the largest earthquakes yet observed occur along the broad interface between two converging tectonic plates called the megathrust. The extent of the megathrust and its associated seismicity differs with each subduction zone, but typically crustal deformation related to the rupture extends both in submarine and terrestrial environments. On land, this coseismic deformation is commonly observed with stationary instruments such as Global Navigational Satellite Systems (GNSS) or through satellite imagery using Interferometric Synthetic Aperture Radar (InSAR). In submarine environments, directly viewing seafloor displacements is more challenging. While seafloor geodetic devices do exist, their sparsity prohibits their integration into most rupture models. In order to infer seafloor crustal deformation and relate it to fault slip, a proxy needs to be used. The best option is to incorporate tsunami waveforms as measured by open-ocean pressure gauges into earthquake source models. Since the tsunami is thought to be directly related to the rapid deformation of the seafloor, its relationship to fault slip can be examined and used in earthquake studies.

This dissertation seeks to constrain the rupture size and magnitude of tsunamigenic earthquakes through the inclusion of data from both traditional geodetic instruments and recently deployed open-ocean tsunami gauges. By collecting and processing on-land geodetic data and offshore tsunami waveforms, data sensitive to a larger region of the megathrust can be incorporated into finite-fault inverse modeling than if using only a single dataset. First, the sensitivity of the subduction zone model space to geodetic and tsunami waveform data is assessed. This provides a picture of where we can and cannot resolve

rupture models when data is limited. It also highlights the issues that can ensue if poorly constrained models are used to study earthquakes. Second, I conduct an event-based joint inversion incorporating both geodetic and tsunami data for the 2015 Illapel, Chile earthquake. This includes merging codes for tsunami propagation, fault deformation, and linear inversions. The result of the joint inversion is a model space that is not only resolved near the coastline where geodetic data exists, but also near the trench where tsunami data is significantly more sensitive. The third component of this dissertation is an analysis of the feasibility of open-ocean data for rapid source inversions. This builds on current tsunami warning center methodologies but with a focus on the time constricted scenarios of a near-field warning from a local tsunami source. Here I analyze four different regions for their tsunamigenic potential as well as their potential to have instrumentation that will provide enough lead time during a local event to record data that is meaningful for disaster management and hazard warnings. The combination of these different aspects of tsunami-geodetic joint inversions illustrates both the improved model resolution and understanding of what was once a poorly constrained problem.

CHAPTER 1. INTRODUCTION

1.1 Motivation

At approximately 8:00 am on December 26, 2004, the western coastline of Sumatra suddenly lurched seaward. Over a period of 8 minutes 1,300 km of the Sumatran megathrust ruptured into a M_w 9.3 earthquake [*Ishii et al.,*2005]. The substantial damage that accumulated over the nearly 10 minutes of shaking was compounded by a destructive tsunami. The inundation caused by the tsunami devastated the nearby coasts of Sri Lanka, Thailand, and Indonesia. As the tsunami continued its path across the Indian Ocean, it continued its destruction along coastlines. Coastal tide gauges reported wave amplitudes of 59 cm near the Cocos Islands (Australia), 261 cm at Salalah, Oman, 100 cm at Lamu, Kenya, and 20 cm at Jackson Bay, New Zealand [*Rabinovich and Thomson*, 2007; *Titov et al.,* 2005]. The devastation caused by the earthquake and tsunami resulted in over 250,000 casualties.

One factor that led to the large degree of casualties following the 2004 Sumatra earthquake was the lack of warning for mid and far field coastal communities about the imminent tsunami. At the time, there was not a tsunami warning center that focused on events in the Indian Ocean. In addition, an internal framework to accommodate the dissemination of warnings to other countries did not exist [*Bernard and Titov,* 2015]. Even if there is a strong oral tradition to evacuate the coastlines following strong shaking, the lack of perceived shaking along many mid-field coastlines meant that the tsunami arrived with little warning.

At the time of the event, the Indian Ocean did not have any instrumentation that directly sampled the tsunami in the open-ocean. While the JASON-1 satellite serendipitously sampled the passage of the tsunami mid-way through the Indian Ocean basin, the satellite, which primarily is employed to study long-term global sea level change, is not designed for sampling tsunami for forecasting purposes. The best way to measure tsunami with the cleanest signal is through instrumentation located in the open-ocean. While prototypes for deep-water pressure gauges and cabled networks had been deployed for operational testing in the northern Pacific, the 2004 Sumatra earthquake acted as the impetus for further development and deployment of instrumentation to monitor and warn communities about potential tsunami hazards [*Bernard and Titov,* 2015]. In addition to forecasting benefits, offshore stations also provide a rich dataset that can be used to better understand slip from offshore earthquakes. When combined with on-land coastal instrumentation, tsunami data can help bridge a gap in understanding of co-seismic deformation across the entire seismogenic portion of the subduction zone.

In this dissertation, I present work focusing on the merging of open-ocean tsunami waveform and on-land static geodetic offsets for coseismic rupture. I also present and comment on the utility of tsunami datasets for its potential early warning capabilities. This work is divided into four sections. This first chapter presents background information relevant to the projects encompassed in the chapters 2, 3, and 4. This includes background of both datasets used and finite-fault models. The second chapter discusses the sensitivity of geodetic and tsunami waveform datasets in the inversion process with a special focus on tsunami data sensitivity. This study is the first, to my knowledge, to look at the sensitivity of tsunami data for the finite-fault problem. The third chapter presents a case study of the

use of a tsunami-geodetic joint inversion for the 2015 Illapel, Chile earthquake and tsunami. This applies the joint inversion process for a scenario where tsunami data provides additional and much needed resolution to the offshore environment. Finally, the fourth chapter discusses the potential benefits that a tsunami dataset can provide to localized tsunami early warning for the near-field environment.

1.2 Tsunami

Tsunamis are a series of long waves generated either seismically from submarine earthquakes, or non-seismically from submarine landslides, asteroid impacts, volcanic eruptions, or any other event that rapidly disturbed the water column over a large spatial scale. Typical tsunamis fall into the category of shallow-water waves. This means the wavelength of the tsunami (horizontal scale) is significantly larger than the water column (vertical scale). For example, a typical tsunami can have a wavelength upwards of 100 km as it propagates through a basin with an average water column depth of 3 km. As a shallow water wave, a tsunami will propagate through the open-ocean with an approximate phase velocity of:

$$v = \sqrt{gh} \tag{1}$$

where v is the wave velocity, g is acceleration due to gravity (often simplified to 9.8 m/s^2), and h is the water column height. This means for a tsunami moving through the Pacific Ocean, with an approximate water depth of 3 km, the tsunami itself will travel at about 615 km/hr. As a reference point, a Boeing A380 at cruising speed tops out around 900 km/hr. As the tsunami enters shallower water, the speed decreases. With a coastal water depth of

20 m, the wave slows to about 50 km/hr, about the speed of an automobile stuck on the interstate in Atlanta rush hour traffic. Another phenomena of tsunami approaching the shoreline is shoaling. Shoaling is the transformation of waves as they enter a shallow water environment, often increasing amplitude and decreasing the wavelength of the feature. While wave amplitudes in the open ocean are approximately one meter or less (in most cases), as the wave reaches the shore, the amplitude increases as the wavelength decreases.

The initiation of seismically generated tsunamis is often approximated as an instantaneous seafloor uplift caused by the rupturing fault plane. Because the rupture velocity of the earthquake is much greater than the propagation velocity of the tsunami, this approximation holds for all but the largest of earthquakes and is a useful simplification for tsunami source inversion. Furthermore, by maintaining measurements in the open ocean, the relationship between wave propagation and slip on any discrete patch of a fault can be modeled as a linear process [*Wei et al.,* 2003]. For a pre-defined and discretized fault plane, a catalog of synthetic waveforms at the location of open-ocean gauges and related to each section of the fault can be used to approximate the right locations and amounts of slip that best recreate the observed waveform. This is the basis for the Short-term Inundation Forecasting for Tsunami (SIFT) database used by NOAA for real-time tsunami inundation warnings following subduction zone earthquakes [*Gica*, 2008; *Titov*, 2009]. Each unit source in SIFT has a 100 km by 50 km source dimension, equivalent to a M_w 7.5 earthquake. While this is too coarse to determine most features in a post-event survey, the simplicity is vital for quick warnings to far-field communities, where specific tsunami source properties are less important [*Titov et al.,* 2001]. However, for detailed

post-event studies, the fault plane discretization would ideally be computed on a much finer scale, to allow for greater detail in the inverted slip pattern.

1.3 Tsunami Datasets

1.3.1 Tide Gauge

Some of the earliest quantitative observations of tsunamis were recorded at coastal tide gauges. These gauges, oftentimes situated within harbors and near the shoreline periodically measure the water column height for purposes of reporting tides. They can be affected by varying coastal morphology, the influence of wind waves, harbor resonance, signal clipping, and aliasing [*Rabinovich and Eble*, 2015], which can be difficult to reliably filter out of the original waveform without analyst input [*González et al*., 2005]. Despite these negatives, tide gauges are the most ubiquitous dataset that records tsunami and in some locales, the only dataset. Furthermore, the basis for tsunami source inversions started with tide gauge data [*Satake*, 1987]. The data is still incredibly useful both in source inversions and also for forward validation of rupture models. Peak amplitudes from tide gauges can also be used to model the coastal response of the tsunami and as a tool in post-event surveying.

1.3.2 DART

In the mid-1990s, the U.S. National Tsunami Hazard Mitigation Program (NTHMP) led an effort to deploy a network of bottom pressure recorders for use as tsunameters [*Mungov et al.*, 2013]. These gauges eventually earned the name of Deep-ocean Assessment and Reporting of Tsunami (DART) gauges. Following the 2004 Sumatra

earthquake and tsunami, the United States facilitated the deployment of DART gauges within the Pacific and Atlantic for the purposes of providing warning to the US about

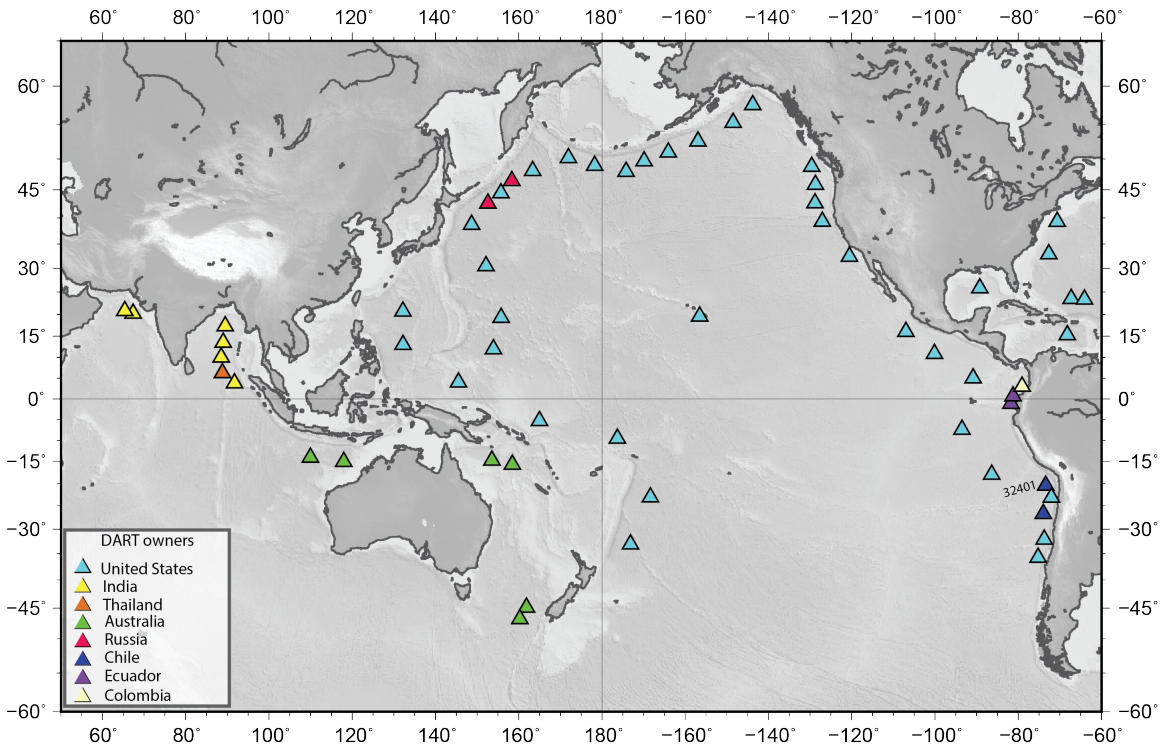

Figure 1.1. Global array of DART gauges as of Spring 2018.

tsunami threats from both local and distant earthquakes. Australia, Thailand, and India also have deployed stations for use within the Indian Ocean. Other countries that have deployed DART sensors since 2004 include Chile, Colombia, Ecuador, Japan, and Russia. Currently there is a global array of over 60 DART gauges managed in part by the National Data Buoy Center (NDBC), Figure 1.1.

Each gauge consists of two main components: the seafloor pressure gauge and the surface buoy. The pressure gauge, which also keeps internal measurements of temperature and salinity, relays data to the buoy through a cable-less acoustic channel. Data on the water pressure, which is translated to water column height through a constant of 1 psi =

670 mm, is relayed from the buoy to data centers via satellite and is openly available in semi-real time [*Meining et al.,* 2005]. While each gauge has a sample rate of 1 sample every 15 seconds, which is stored internally, the amount of data that is relayed via satellite is dependent on the status of the device. In a standard mode, data is transmitted with a 15-minute sample frequency every six hours [*Bernard and Meinig,* 2011]. In an event mode, data is relayed at its full sample rate and then at 1 minute averaged samples.

Open-ocean pressure sensors provide a 'clean' dataset that directly records the passage of tsunami waves; DART record tsunami with a high signal to noise ratio. The open-ocean location removes the problems of harbor and shelf resonance, which are typically recorded at coastal tide gauges. The sample rate of the gauges and the long wavelength of tsunami in open-ocean means that the chances of aliasing, or misrepresenting the waveform through too-low of a sample rate, are low. Because tsunami waves have a low amplitude in open water, clipping of the signal is not an issue either. The largest signal that needs to be removed from open-ocean tsunami waveforms stems from tides. While there are a few different methodologies for filtering tides out of the waveform, as discussed in *Percival et al.* [2015], in some cases a relatively simple high-pass filter or polynomial fitting scheme can suffice.

Figure 1.2 shows a sample recording from DART gauge 32401, located off the coast of Northern Chile following the 01 April 2014 Iquique earthquake and tsunami. The 'raw' waveform shown in the top panel is dominated by a lower period oscillation due to tides. The raw data has a variable sample rate, with 15-minute data prior to the event, then 15 second and one-minute data. First the time series is interpolated to a consistent one-minute sample rate. Then the tidal signature is removed through a high-pass filter that removes

energy with a period greater than 240 minutes. If desired, additional filters can be used to remove the aliased surface waves that are recorded at the station prior to the tsunami's

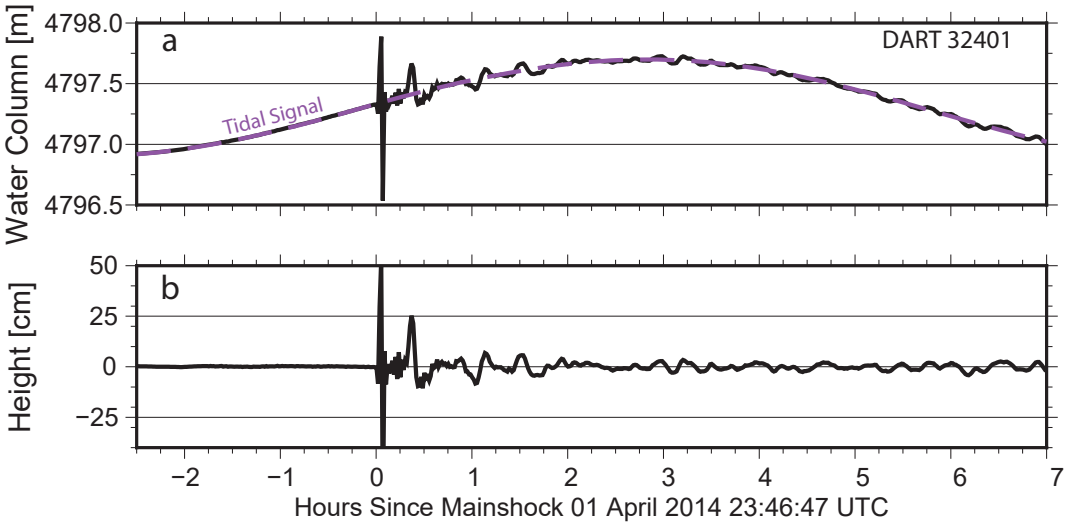

Figure 1.2. a. Raw tsunami signal from gauge 32401, located off the coast of Northern Chile. B. Signal with tidal signature removed.

arrival. In this example, the tsunami signal begins about half an hour after the mainshock rupture. The signal continues past the seven hours shown in the time series as the wave train continues to reflect off nearby coastlines.

Most currently deployed gauges sit far from potential tsunami sources. Newer DART 4G instruments, which are in test operations offshore Oregon and Chile, are capable of up to a 1 Hz sampling frequency [*Rabinovich and Eble*, 2015; *Tang et al.,* 2016] and are deployed closer to the trench and potential tsunami sources. This potentially earlier arrival of the tsunami to the sensor may make it possible to warn communities closer to the epicenter of the tsunami threat without a complete reliance on seismic approximations.

1.3.3 Cabled Arrays

An alternative to the free-standing DART gauge is a denser and more localized array of stations joined through a cable line. There are three locations that currently have seafloor cabled arrays, Japan, Canada, and Oman. The former two's arrays are briefly discussed below. While data from these arrays has not been explicitly applied to finite-fault modeling work in this dissertation, they have similar capabilities to DART gauges and provide a dataset worth incorporating for real-time tsunami analysis.

Japan has 11 different cable lines incorporating open-ocean pressure instrumentation. Three of the largest cabled arrays within the country are DONET-1, DONET-2, and S-NET. DONET-1 and DONET-2 both contain clusters of instrumentation including seismometers, accelerometers and bottom pressure gauges, deployed offshore of the Kii Peninsula and within the Nankai seismic zone [*Rabinovich and Eble*, 2015]. S-Net (Seafloor Observation Network for Earthquakes and Tsunami) was deployed off the Japan trench to provide real-time earthquake detection for events affecting the Japanese mainland [Rabinovich and Eble, 2015]. The S-Net array is included for reference in Figure 4.3.

The Canadian North-East Pacific Underwater Networked Experiments (NEPTUNE) is a cabled observatory within Ocean Networks Canada with six bottom pressure gauges connected in a loop. Almost immediately after deployment, the network observed the passage of the tsunami generated from the 2009 Samoa earthquake. The network sits on the accretionary prism offshore from Vancouver Island and provides an intermediate dataset between open-ocean sensors and coastal tide gauges that can be used for localized warning.

The cabled networks discussed involve clusters of instrumentation tasked with making various measurements (temperature, shaking, salinity, pressure) which can be employed for a host of geological questions in addition to tsunami science. Each instrument is connected to the next in series through a cable which is then linked to a coastal site, allowing for data relay without sea-surface buoys.

1.4 Geodetic Datasets

Global Navigation Satellite System (GNSS) data can be used to determine the exact location of a receiver with up to millimeter levels of accuracy. GNSS can be used as a general term for a few different global positioning constellations, including the familiar (Global Positioning System) GPS, but also the Russian GLONASS and the European Galileo systems, to name a few. GPS, specifically uses a constellation of 24 satellites to ensure that any receiver always has the minimum number of four satellites to accurately determine its position. The overall cost of GNSS receivers is low compared to other geophysical instrumentation and deployment is fairly simple, making dense networks sampling deformation related to the seismic cycle feasible [*Blewitt*, 2015].

For use in earthquake modeling, GNSS instruments, placed over the seismic cycle of one region, can measure many aspects of the seismic cycle. In the case of the Nicoya peninsula, located in Costa Rica and the site of the 2012 M_w 7.6 Nicoya earthquake, GPS was used to measure the accumulation of strain before an earthquake [*Feng et al.,* 2012], the coseismic deformation [*Protti et al.,* 2014], and the post-seismic relaxation of the crust after the earthquake [*Wang et al.,* 2012; *Hobbs et al.,* 2017]. Some countries have dense GNSS arrays installed, aiding in the detection of and modeling of earthquakes. Japan's

GPS Earth Observation Network (GEONET) consists of over 1,300 continuous sites providing position data in real time. GEONET effectively captured the on-land deformation during the 2011 Tohoku earthquake, showing a wholesale seaward motion of the sensors with horizontal motions of up to 5 m and vertical subsidence of 1.2 m in some coastal locations [*Nishimura et al.,* 2011]. Dense arrays of GNSS near the Cascadia subduction zone monitor not only strain accumulation from inferred plate locking, but also motions associated with slow slip events [*Rogers and Dragert*, 2003]. Studies have also been completed assessing the applicability of GNSS data for rapid fault plane solutions that can be used in hazard warnings [*Blewitt et al.,* 2102; *Crowell et al*., 2012].

Interferometric Synthetic Aperture Radar (InSAR) is another method used to determine crustal deformation. A single satellite carrying synthetic aperture radar equipment can scan the ground, recording the travel time and phase information between satellite source and reflector. Coseismic deformation, measured on a pixel by pixel bases over a broad swath of land, can be determined assuming there is sufficient imagery before and immediately after the event and assessing the change in phase, which is related to the change in path length between antenna and reflector. Changes in phase can be unwrapped and geocoded to determine deformation in the line-of-sight direction of the satellite.

This technique has been common for assessing coseismic deformation as it provides a dense dataset of deformation, so long as there are good reflectors (i.e. exposed rock) [e.g. *Simons et al*., 2002; *Pollitz et al.,* 2012; *Simons and Rosen*, 2015]. One drawback to InSAR is it cannot be used to assess deformation occurring under water, and it is dependent on having a satellite pass both before and earthquake and within a short period after the earthquake (to lessen the effects of after-slip and aftershocks).

1.5 Assessing Slip on Fault Planes

1.5.1 Finite-Fault

Finite-fault models (also called kinematic models) are used to characterized coseismic slip from earthquakes by discretizing pre-determined fault geometries into gridded model domains. Through observations of the earthquake and its coseismic deformation, fine scaled features outlining the spatial extent of rupture can be achieved. These slip models can be compared with previous assessments of fault locking and be used to infer stress on the rest of the fault [e.g. *Moreno et al.,* 2010, 2011; *Lorito et al.,* 2011]. Often the fault geometry in question is constructed as an *a priori* constraint using locational clues such as surface ruptures or past studies of regional fault interfaces. Other times, the shape and location of the fault used is an additional unknown parameter to be solved for [e.g. *Gusman et al.,* 2018]. One common set of fault geometries used for finite fault modeling of subduction zone events is the Slab 1.0 model developed by *Hayes et al.,* [2012]. These models primarily approximate the megathrust environment. Earthquakes are also possible along splay faults within the sedimentary wedge or on the outer rise of the subducting plate.

Finite fault models can incorporate data from a wide range of instruments. Rupture extent through seismic waveforms is one of the oldest and most common datasets. Geodetic instrumentation like GNSS and InSAR can also be successfully incorporated. Tsunami waveforms can be an extremely useful tool for earthquakes with a large component of rupture underwater and is becoming more a more commonplace tool as the number of reliable open-ocean instrumentation has been increasing over the past two decades.

1.5.2 Tsunami Propagation Models

One of many tsunami propagation schemes is the Method of Splitting Tsunami (MOST) model, a finite difference model that solves the non-linear shallow water wave equations [*Titov & González,* 1997]. The model was first developed in the USSR before further development in the United States [*Titov et al.,* 2016b]. It is currently an operational tool at the NOAA Tsunami Warning Centers and at the NOAA Center for Tsunami Research.

An additional tsunami propagation code, JAGURS, has been developed recently to include additional parameters that may play an important role in far-field tsunami modeling. JAGURS, developed by *Baba et al.* [2015] and incorporating works by *Allgeyer and Cummins* [2014], is a finite difference method code that in addition to solving the non-linear shallow water wave equations, has the capabilities to incorporate elastic loading, seawater compressibility, gravitational potential change and Boussinesq dispersion into the simulation. These additional parameters included in JAGURS are useful for modeling tsunami propagating into the far-field.

CHAPTER 2. LIMITATIONS OF THE RESOLVABILITY OF FINITE-FAULT MODELS USING STATIC LAND-BASED GEODESY AND OPEN-OCEAN TSUNAMI WAVEFORMS

2.1 Abstract

Finite-fault slip inversions are a commonly employed following large earthquakes to understand the nature of slip along a fault plane. Using multiple datasets, such as static offsets from on-land geodetic instruments and wave heights derived from open-ocean waveforms, a comprehensive view of slip across most of the seismogenic zone can be created. This merging of land and ocean based data is particularly advantageous along subduction zones where direct measurement of seafloor deformation is currently limited. This study analyzes the model resolution attained individually from geodetic and tsunami datasets. We constrain the importance of distance between estimated parameters and observed data and how that varies between land-based and open ocean datasets. For on-land static offsets, we find that the maximum distances possible to retain high model resolution can be as low as 40 km for some fault geometries. Open-ocean time series, on the other hand, is less dependent on the distance between data and model and more on the length of time series used, which is often limited through processing and uncertainties in tsunami propagation modeling. The effect of model resolution based on data type is explored in this study through multiple synthetic fault plane tests to highlight the benefits and limitations of each data type.

2.2 Introduction

The long, inter-plate boundary within a subduction zone, called the megathrust, produces some of the largest yet observed earthquakes. This environment poses a great threat not only from damaging localized ground shaking, but occasionally through coastal inundation caused by tsunami. Kinematic models (also called finite-fault models) of coseismic slip are routinely employed following many large earthquakes to better understand tectonic strain release across an approximated fault. When focusing on coseismic strain release along subduction zones, geodetic datasets, such as Global Navigation Satellite System (GNSS) and Interferometric Synthetic Aperture Radar (InSAR) are some of the most common instruments used to determine precisely the extent of ground deformation. This surface deformation is then related to slip along an *a priori* fault geometry within the megathrust. Tsunami datasets such as tide gauge records, costal run-up observations, and open-ocean waveform records can also all be used to provide additional data on the rupture if there is a substantial submarine component. Post-event rupture analysis using geodetic and tsunami datasets have been common in many recent studies of large (M > 8) subduction zone earthquakes including the 2017 Chiapas, Mexico earthquake [*Gusman et al.,* 2018; *Ye et al.,* 2017], the 2015 Illapel, Chile earthquake [*Heidarzadeh et al*., 2016; *Melgar et al.,* 2016; *Williamson et al.*, 2017], and the 2014 Iquique, Chile earthquake [*An et al.,* 2014; *Gusman et al.,* 2015].

One prevalent problem with finite-fault modeling along subduction zones is acquiring sufficient data to confidently resolve the observed slip behavior. When data is limited to on-land geodesy, slip occurring off-shore will have resolvability that decreases with seaward distance. This is inherently problematic for tsunamigenic earthquakes that propagate large slips in the near-trench region which can be far from the nearest approach

by land. This is illustrated in Figure 2.1, where the trench-to-shoreline distances vary among major seismically active subduction zones. For each of these locations, the expected seismogenic zone along the megathrust contains a substantial offshore component. When data limited, there becomes a point where near-trench slip is too far to be adequately resolved by solely on-land data. How far is too far is a topic of discussion in this study.

Seafloor geodetic techniques such as GPS-acoustic or absolute pressure instrumentation [e.g. *Gagnon et al.* 2005 *Chadwick et al.* 2012], can potentially increase resolvability by allowing much more localized observations, however those data are currently uncommon, in large part due to current costs [see *Newman,* 2011]. In the meantime, the current lack of widespread and localized measurements offshore leads to a substantial difficulty in determining the extent of slip offshore and therefore the hazard of these near-trench subduction zone environments.

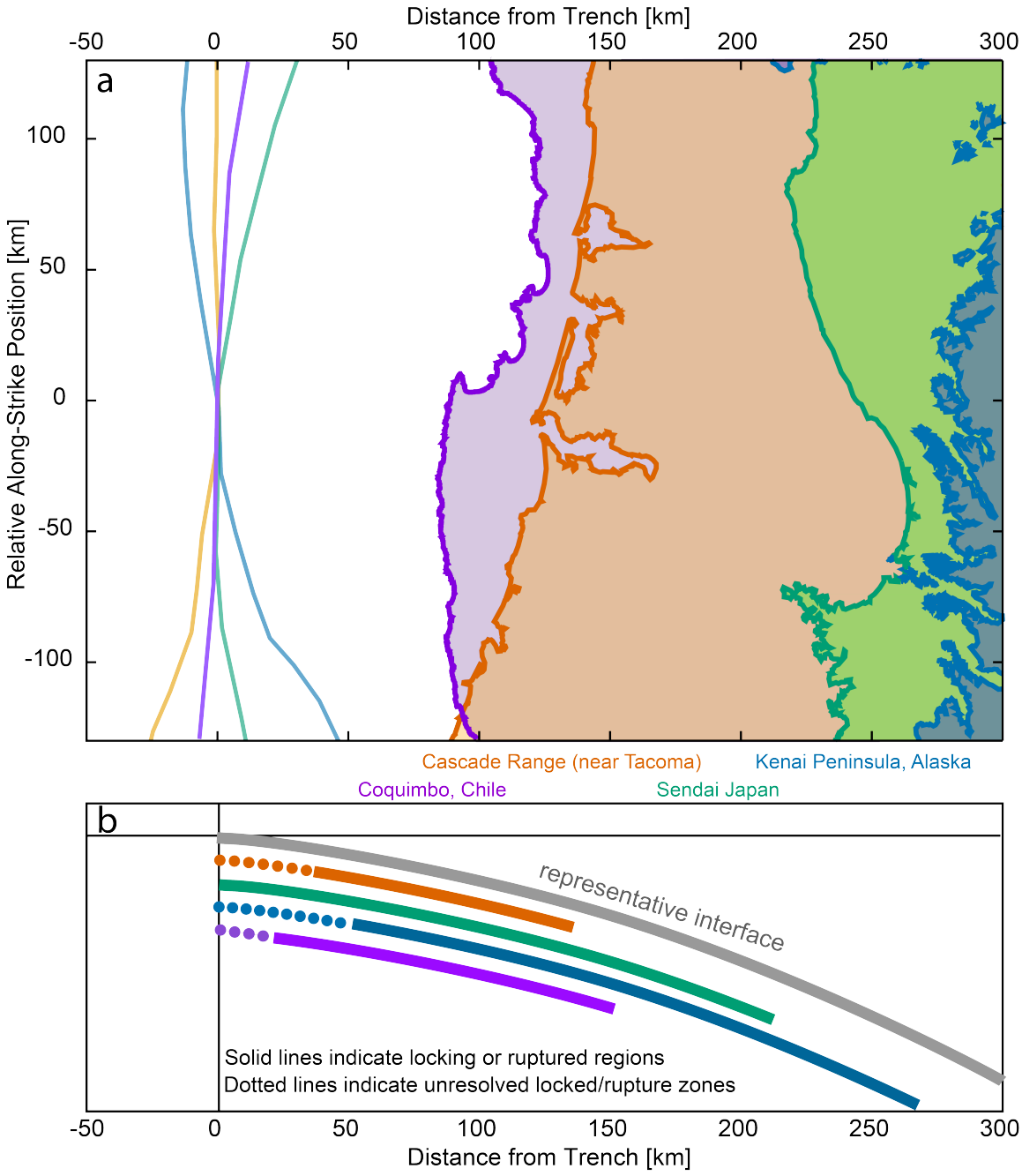

Figure 2.1. A. Comparison of coastline to trench distances for four subduction zone regions of interest. Trench locations for each region determined from *Bird and Kagan*, [2004] and aligned to a centralized point to assess relative distances. B. Inferred regions of locking for each region using a representative interface. Cascadia locking inferred from *McCaffrey et al.* [2007] and *Schmalzle et al.* [2014]; The up-dip extent of rupture for Japan is from *Wei et al.* [2014] and *Fujii et al.* [2011] and the lower limit is based on coupling models by *Loveless and Meade* [2011]; Extent of the Kenai Peninsula is extrapolated from the 1964 rupture zone as published in *Li et al.* [2013]; The Coquimbo locking is inferred from the rupture and coupling models published in *Metois et al.* [2012], *Tilmann et al.* [2016] and *Williamson et al.* [2017].

The present solution to this problem of geodetic data scarcity is to utilize currently deployed, offshore sensitive datasets. This includes the few GPS-A instruments, when available, but also open-ocean tsunami data. Tsunami gauge data provides a wealth of information concerning the offshore component of rupture. However, unlike on-land geodetic datasets, the sensitivity of these offshore pressure gauges to the model resolution are not yet well understood. In this study, we analyze the contribution in resolution the open-ocean tsunami waveform provides to the inverse problem and how it compliments geodetic datasets for use in subduction zone finite-fault problems. First, we illustrate the difficulty in attaining high model resolution offshore when using solely land-based geodetic datasets in a subduction zone setting. Second, we qualify the model resolution attained through open-ocean waveforms for the same inverse problem. Third, we make recommendations for the minimum amount of offshore data necessary to sufficiently resolve finite-fault spatial domains based on event size and fault discretization. We conduct this study using synthetic fault models, allowing us to test the effect that the number of offshore sensors, and their location relative to the model space affects the model resolution.

2.3 Data

2.3.1 Geodetic Data

Geodetic data like GNSS can directly measure coseismic deformation on land in three-components. This dataset is useful as unlike seismic strong-motion data, it does not 'clip' or alias if placed near the source and provides a direct assessment of deformation. Measurements from ascending and/or descending InSAR imagery provide phase changes between two time-separated passes of the same region with the same look direction. The

phase changes at a pixel level can be translated into line-of-sight (LOS) deformation. While both of these methods are commonly used in event-based modeling, they can only measure deformation occurring over land. GPS-acoustic devices, where available, can provide points of reference on the sea-floor to measure seafloor deformation. In this study, we use synthetic three-component static offsets as would be measured through GNSS instrumentation to assess the change in resolution with distance from data.

2.3.2 Tsunami Data

Open-ocean data can stem from a few different sources. The most widespread and openly available source is from the Deep Ocean Assessment and Reporting of Tsunami (DART) gauges. This array consists of a global distribution of 60 pressure gauges situated near many of the world's subduction zones [*Bernard and Meinig* 2011; *Mungov et al.,* 2013; *Rabinovich and Eble*, 2015]. Other smaller or more localized pressure gauge arrays are included in the cabled networks located offshore of Canada and Japan, respectively [*Barnes et al.,* 2013; *Rabinovich and Eble*, 2015]. While these cable networks are dense and highly localized, they have been incorporated into study of far-field tsunamigenic events. The Canadian North-East Pacific Underwater Networked Experiments (NEPTUNE) observatory's six pressure gauge stations observed the passage of the 2009 Samoa earthquake's tsunami, prior to its arrival on the British Columbian shore [*Thompson et al.,* 2011]. Japan's S-NET and DONET cabled networks are deployed between the shoreline and Japan (S-NET) and Nankai (DONET) trenches [*Rabinovich and Eble*, 2015]. The location of cabled arrays along the continental shelf makes it a useful intermediary between deep-water DART and coastal tide gauges. The cabled arrays and DART gauges both operate through similar instrumentation. In this study we focus primarily on the use

of DART gauges, which are typically located > 200 km away from a megathrust earthquake source, however methodologies for assessing resolution can also easily be applied to time series derived from cabled arrays.

2.4 Methods

2.4.1 Finite-Fault Inversions

The generalized damped inversion that we employ assumes a linear system of equations described by:

$$\begin{bmatrix} \mathbf{d} \\ \mathbf{0} \end{bmatrix} = \begin{bmatrix} \mathbf{G} \\ \boldsymbol{\kappa}^2\mathbf{D} \end{bmatrix} \mathbf{m} \tag{2}$$

where data vector, **d**, (length *n*) and the model parameters vector, **m**, (length *m*) are related through a Green's Function matrix, **G** (size *n* x *m*). In this study, the Green's Function is the approximate linear relationship between the free-surface deformation and the thrust component of finite-fault motion on a megathrust (low-angle) fault. For a joint inversion, **G** contains the merger of tsunami and geodetic model responses. To ensure the model is over-determined ($n > m$), a set of regularization equations are added, so that the 'roughness' between adjacent model patches is minimized through a Laplacian smoothing parameter, **D**, and a smoothing constant, κ. The degree of smoothing is determined through an evaluation of the relative increase in misfit obtained for successively larger κ values, yielding 'smoother' model surfaces. Such trade-off curves often have a tell-tale kink where misfits grow rapidly, and hence models are frequently called the 'L-curve test' [*Harris and Segall,* 1987].

The geodetic component of **G** is calculated using the Okada relations for rectangular dislocations in an isotropic and elastic half space [*Okada,* 1985]. The tsunami component of **G** is defined as the open-ocean station response to the same rectangular dislocations. This requires the additional step of modeling the tsunami from source to receiver. To model open-ocean tsunami waveforms, we use the MOST (Method of Splitting Tsunami) model, which solves the non-linear shallow water wave equations [*Titov & Gonzalez, 1997*]. We first determine the instantaneous surface deformation from *Okada* [1985] for each fault patch as an initial condition to the tsunami model. We then sample the tsunami's passage at the location of the open-ocean receiver to generate the tsunami waveform incorporated into **G**. Because the waveforms are sampled in the open-ocean, linearity between the waveform and magnitude of slip along the subfault is maintained [*Wei et al.,* 2003; *Percival et al.,* 2011; *Yue et al.,* 2015]. Therefore, both the geodetic and tsunami Green's Functions can be combined in **G** for the inversion process. To solve the inversion, we modified the Matlab package, *GTdef*, developed by *Chen et al.* [2009], that utilizes a bounded least-squares algorithm.

2.4.2 Model Resolution

Most commonly, resolution assessments of finite fault inversions employ a "checkerboard test", as it provides a visual aid in assessing resolution [e.g. *Chen et al.,* 2009*, Moreno et al.,* 2010; *Romano et al.,* 2012; *Yue et al.*, 2014]. It is natural that most finite-fault models will not have enough data of the right type in the right locations to fully resolve a model over the entirety of the model space- particularly with a finely and uniformly gridded domain. The output of a checkerboard test can differentiate areas with good resolution, giving more confidence to model results over the same area, and highlight

areas with low resolution where modeled features may be artifacts. The assessment of good and bad resolution stems from how well the output checkerboard model resembles a known input- often of alternating 'checkers' of slip. The checker is of a size consistent with the size of smallest feature to be modeled. While a well-resolved region will recreate the input, a poorly resolved model will not—either the checker shape will be smeared, or the result will be an incoherent arrangement of slip.

An alternate method of evaluating finite fault resolution is done by building the model resolution matrix as a product of the model inversion process [*Menke,* 1989]. While the method has been used in some past geodetic studies [*Page et al.,* 2009; *Barnhart and Lohman*, 2010; *Atazori and Antonioli*, 2011; *Kyriakopoulos and Newman*, 2016], our study is the first known application to the tsunami wavefield.

Once the Green's Function matrix is compiled, the model resolution matrix is determined by solving

$$\boldsymbol{R} = [\boldsymbol{G}^{\boldsymbol{T}}\boldsymbol{G}]^{-\mathbf{1}}\boldsymbol{G}^{\boldsymbol{T}}\boldsymbol{G} \tag{3}$$

for the inverse problem [*Menke,* 1989]. The matrix, **R**, contains information on the resolving power of the model for each parameter to be estimated. In an ideal case, where the model is fully resolved, **R** = **I**, the identity matrix. In reality, however, this is not the case and the diagonal components of the matrix will be less than one with off-axis values indicating the interdependence between model components. The values obtained for the model resolution will depend on data type, location, and model, but not on the individual values of the data.

Past studies analyzed the limits of model resolution for the purposes of kinematic modeling of land-based geodetic data. Non-uniform grid algorithms built to match spatial resolving power of geodetic data to subfault size have been developed and were applied to events such as the 2004 Parkfield earthquake [*Page et al.,* 2009] and the 1995 Antofagasta, Chile earthquake *[Barnhart and Lohman,* 2010]. Areas with low resolving power dictate the necessity of coarse patches while areas with higher resolution are resolved with a finer grid. [*Atazori and Antonioli*, 2011]. This discretization reduces the influence of artifacts in the model results—unfortunate products common in the deeper, less resolved, portion of models.

2.5 Results

2.5.1 Geodetic Resolution

While some attention has been given to the general use of the resolution matrix in subduction zone settings for specific earthquakes [*Barnhart and Lohman*, 2010; *Kyriakopoulos and Newman*, 2016], it is also useful to look at the optimal attainable model resolution through synthetic testing. First, such synthetic tests allow for the reduction of uncertainties that are present in event-based modeling by the creation of simple known forward models. This allows for a comparison between a result and its synthetically-generated 'true' slip distribution, which is impossible to determine for real-world cases. Secondly, and pragmatically, such synthetic models are useful for understanding the limits and options available for instrument network design.

To analyze the general subduction zone resolution problem with GNSS static offset data, we first create a simple checkerboard input. Then, datasets at varying locations can

be used to assess the change in the ability of the model configuration to recreate the original checker configuration. The spatial domain approximates a subduction zone with a shallow dipping megathrust that is discretized into small 10x10 km cells. A checker pattern with a 30 x 30 km pattern of slip alternating between 0 and 1 m of pure thrust is used as a forward input **(**Figure 2.2a). The output of the test, shown in Figure 2.2b-d is the inversion result using synthetic three-component GNSS data. The synthetic data used has noise added amounting to 5% of the signal for horizontal and 10% for vertical components. In each case, the checkerboard output illustrates a loss of resolution over a large spatial domain as data location varies. In Figure 2.2b, where data is densely distributed over the entire rupture plane, the checkerboard pattern is recreated throughout the spatial domain. A small smearing of the checkers occurs in the down-dip direction where resolution is reduced due to increased distance between the surface data and the model interface at depth. Figure 2.2c and d show the resolution as the GNSS dataset locations are transposed 50 and 100 km in the down dip direction. The near-trench resolution is lost as the data is transposed, resulting in an incoherent fault plane solution where the checker pattern is no longer recreated. These near-trench model parameters sit in a null-space where the data is insensitive to the values of the parameter. These null-space solutions, particularly when they look physically feasible in source inversions, run the risk of being interpreted as real features of the model.

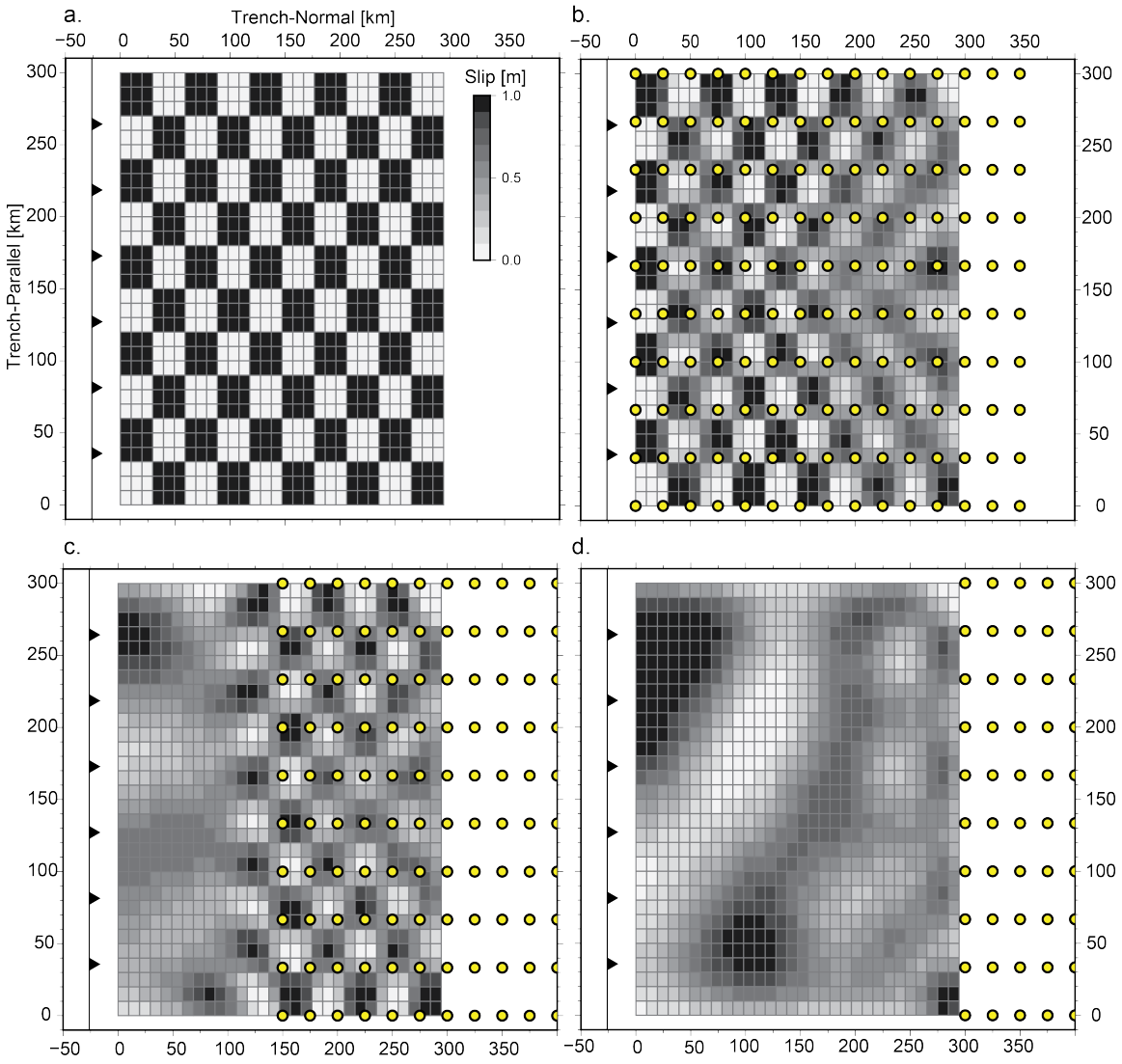

Figure 2.2. Checkerboard resolution for a planar buried fault with a 15-degree dip and synthetic 3-component GNSS using static offsets. A. Checkerboard input using 30x30 km checkers of alternating 1m and 0m of pure thrust. B. Checkerboard results using a dense array of GNSS sensors (red circles) that cover the entire spatial domain. C. Checkerboard results using an array of GNSS with the same density as B. but transposed 150 km in the trench-normal (down-dip) direction. D. Same as C. but with the array transposed 300 km in the trench-normal direction.

While checkerboard tests provide a visual representation of how well a model can recreate results, the model resolution matrix provides quantitative assessment of fault

recoverability. The change in the model resolution along a trench-normal transect of the subduction zone, with variable GNSS data distance is shown in Figure 2.3. Each diagonal component, *i*, of the model resolution matrix **R**, representing the resolution of each fault patch along the transect, is plotted. The same model geometry as shown in Figure 2.2 is used, focusing on the first 100 km in the trench-normal direction. The location of the GNSS dataset retreats in the down-dip direction over each iteration of the inversion in 20-km increments. When data coverage is high and located near the model space, the diagonal component of **R** approach one. As the data coverage in the near trench environment gets worse, the diagonal components of **R** decrease. In the case where the only data available is far from the trench, the diagonal components of **R** approach zero.

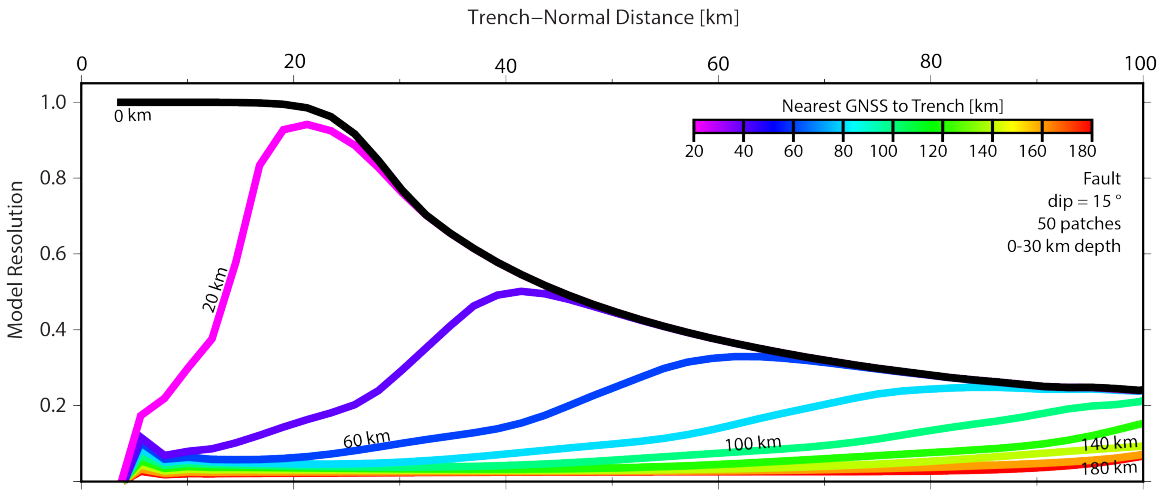

Figure 2.3. Transect in the trench-normal direction for the first 100 km of a shallowly dipping interface, approximating a subduction zone. Model resolution in the trench-normal direction is plotted for 10 scenarios (colored lines). The location of the GNSS dataset retreats in the down-dip direction over each iteration of the inversion in 20-km increments.

There are two factors displayed in Figure 2.3 that affect the resolution of GNSS data: the increasing depth of the fault plane to the surface dataset, and the distance between the data and potentially offshore model parameters. The effect of fault depth is shown by the "0 km" black line in Figure 2.3. In this case, GNSS data is present over the entire trench-normal profile where at 0km the fault intersects the surface, and just past 100 km, the fault reaches a depth of 30 km. For the first 20 km along the profile, representing the shallow and near-trench environment (between 0 and 5 km depth), the diagonals of **R** approach one. After this point, the resolution begins to visibly diminish where $R_i = 0.98$, but superb resolution is still maintained. At 40 km from the trench, the depth to the fault reaches 10 km, and the model resolution is halved ($R_i = 0.5$). At 75 km from the trench, the fault depth increases to 20 km and the resolution decays further ($R_i = 0.28$). As the depth of the interface continues to increase from 20 km to 30 km, the model resolution continues to lower, but at a slower decay than in the near trench environment. The effect that fault depth has on the resolution is most pronounced in the shallow environment, where every 1 km increase in depth is associated with a decrease in R_i of 0.07. Past 40 km depth, an increase in depth has a negligible effect on model resolution where every 1 km in depth is associated with a decrease in R_i of 0.02. If the dip angle in this model is increased from 15 degrees to 30 degrees then the near-trench resolution is even lower as the depth from data to model space increases.

The change in resolution associated with the distance between the data and potentially offshore model parameters is encompassed in the colored lines in Figure 2.3. Each line highlights the one-sided problem of on-land only geodetic data by the march back of data availability from the trench in 20 km increments. Almost immediately, as data is removed

from the immediate near-trench vicinity, we lose resolvability. More resolution is lost due to distance in the trench-normal direction than with the same distance from surface to fault depth. When data is located 20 km away from the trench, the decay in model resolution in the seaward direction is substantial. When using the "20-km" dataset (pink line) at a trench-normal distance of 20 km, $R_i = 0.94$. However, resolution of the model space just 10 km trenchward leads to $R_i = 0.35$, or a 63% reduction in resolution. This same trend continues with each scenario where data is located progressively further down-dip with progressively less resolution up-dip.

As potential data is over 60 km away from the trench, the resolution everywhere in the presumed seismogenic environment remains low and nowhere is **R** near one. Even between 60 and 100 km the resolution is reduced as the depth to the fault plane is greater. A solution that raises the values of **R** is to increase the size of fault patches used in the inversion to match the level of data availability. By analyzing the resolution spread, or the smallest recoverable feature as a function of local model resolution, areas that consistently show poor resolution can be re-gridded to a coarser configuration. This can also reduce the chance of modeling artifacts that are not well represented in the data. The use of resolution spread will be discussed in further detail in the tsunami data section of this study.

The illustrated case of resolution loss with data offset from the model are indicative of the real world problem of offshore data sparsity along subduction zones. Figure 2.1 shows the distance between coast and trench for four different regions. In some regions along the Pacific Northwest, the distance between the coastline and the trench approaches 130 km, well past the resolvable zone highlighted in Figure 2.3. The coastline near Honshu, Japan – close to the 2011 Tohoku-Oki earthquake and tsunami- is nearly 200 km away from the

trench. Even in areas with relatively narrow margins, like off the coast of Chile, the distance can exceed 75 km. While the resolving power of the model near coastlines can be maintained, a dataset that is sensitive to near-trench slip can greatly increase the resolving power over this part of the spatial domain. In the absence of seafloor geodetic data, tsunami waveform datasets will likely provide much improved resolution over this environment.

2.5.2 Tsunami Resolution

Because of the low amplitude and long wavelength nature of tsunami in deep-water, open-ocean gauges can accurately measure the entire tsunami signal without clipping. The first arrival of the tsunami at pressure gauges is usually free of coastal reflections and harbor effects. Therefore, the recording is only dependent on the initial seafloor deformation and any deep-ocean propagation path effects, and suffers from few non-linear effects, particularly in the first 1000 km, or so of wave propagation. As such, many studies treat the tsunami as a linear extension of the slip along the fault [*Wei et al.,* 2003; *Percival et al.,* 2011; *Yue et al.,* 2015]. Coastal tide gauges can also measure tsunami, but in general, are noisier and have a larger potential to clip or under-sample the shoaling wave [*Bernard et al.,* 2006]. This adds greater uncertainty to the model than do open-ocean data.

In this study, we use synthetically generated tsunami waveforms for an array of theoretical pressure gauges to assess the same model resolution parameters as was shown for the geodetic data. The pressure gauge locations for which waveforms are calculated are kept between 500 and 800 km seaward from the source zones, simulating typical distances found in some recent studies using tsunami data for source inversions [e.g. *An et al.,* 2014; *Williamson et al.,* 2017; *Adriano et al.,* 2018]. Here, we use the same fault geometry as

used in the geodetic analysis (Figure 2.2), however the cell size is increased from 10x10 km to 30x30 km. This coarsening of the cells allows for each individual cell to be large enough to create a tsunami that will satisfy the linear shallow-water wave equations where the tsunami wavelength must be substantially larger than the water depth [*Satake,* 1987]. The subfault size is also within range of the dimension used in past tsunami inversion studies [e.g. *Fujii et al.,* 2011; *Heidarzadeh et al.,* 2016; *Yoshimoto et al.,* 2016].

Key questions about tsunami model sensitivity include a) how the resolution changes based on number of gauges used and b) how the resolution changes with gauge location. For geodetic static offsets, the data location is very important to the overall resolution. One station can only resolve features in its immediate vicinity but a distributed array can provide adequate resolution over a much larger region. Since each tsunami waveform is a time series, one station is potentially sensitive over a larger region than static offsets from GNSS, which are sensitive to slip in the immediate vicinity. Figure 2.4 illustrates this concept by looking first at an idealized waveform inversion using tsunami data and a second at a more representative result with a realistic handling of the dataset.

Because the tsunami data used is a time series, the observed waveform includes data from slip on each of the subfaults, assuming that the waveform has a high enough sample frequency and duration. We focus our tsunami study on open-ocean data derived from DART gauges, which has an event mode sample rate of 15-seconds and then averaged 1 minute samples, well above the Nyquist frequency of an open-ocean tsunami wave [*Meinig et al.,* 2005]. Figure 2.4a shows the model resolution using one synthetic gauge and the entire recorded waveform with a sample frequency of 60 seconds and an added noise of 10% of the signal. In this end member case, one waveform is sensitive to all of the

subfaults, therefore the entire fault plane has nearly perfect resolution, where **R** approaches the identify matrix, **I**. Likewise, the checkerboard tests using the same dataset (Figure 2.5) appears to replicate the original checker pattern. However, it is important to note that this well-resolved result is an idealized scenario and does not include effects that are seen in real tsunami signals, leading to a physically improbable result.

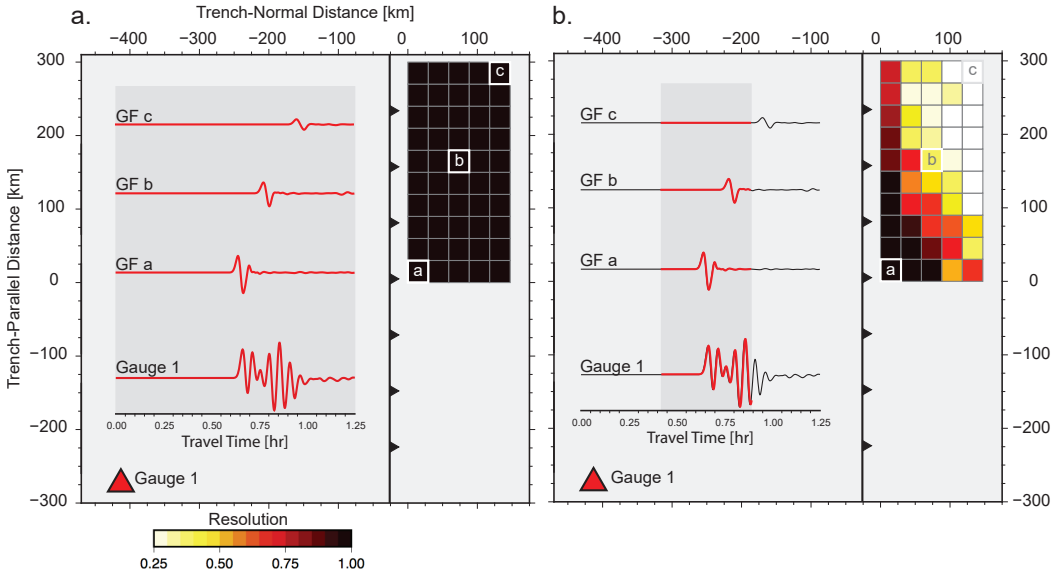

Figure 2.4. The model resolution for each subfault using only an open-ocean tsunami dataset. **A.** Inversion using the full highlighted waveform from gauge 1. The observed waveform, as well as the Green's functions for subfaults a, b, and c are highlighted. **B.** Inversion using a windowed portion of the time series observed at gauge 1. Windowing removes currently unsolvable effects such as costal reflections and complex bathymetry. Windowed portion incorporated into inversion is the observed waveform is highlighted in red. The same Green's functions as shown in panel A. are also shown, but highlighting the windowing process. Note how Green's function "c" is not included in the window, leading to the poor resolution.

A typical 'real' tsunami signal will likely include effects that are difficult to adequately model through linear approximations. One of the largest sources of uncertainty is the loss of energy due to coastal reflections which affects the latter part of the wave train at open-

ocean gauges. For the purposes of illustrating an ideal case, these effects are ignored in Figure 2.4a. Real data is typically treated through filtering to remove signals at a higher frequency than the subfault size as well as to remove long period tidal signatures. Windowing of the tsunami time series is also extremely common. Windowing typically crops the desired time series to the tsunami arrival at the gauge in addition to the first few wavelengths of the tsunami. Later phases are discarded to reduce the impact of un-modeled effects. Unfortunately, at times useful primary fault slip information is also thrown out with these data. We focus on the effect that data loss due to windowing has on the resolvability of a model space. The effect of filtering of tides and the uncertainties that can be accrued have already been summarized in great detail in *Percival et al.* (2015).

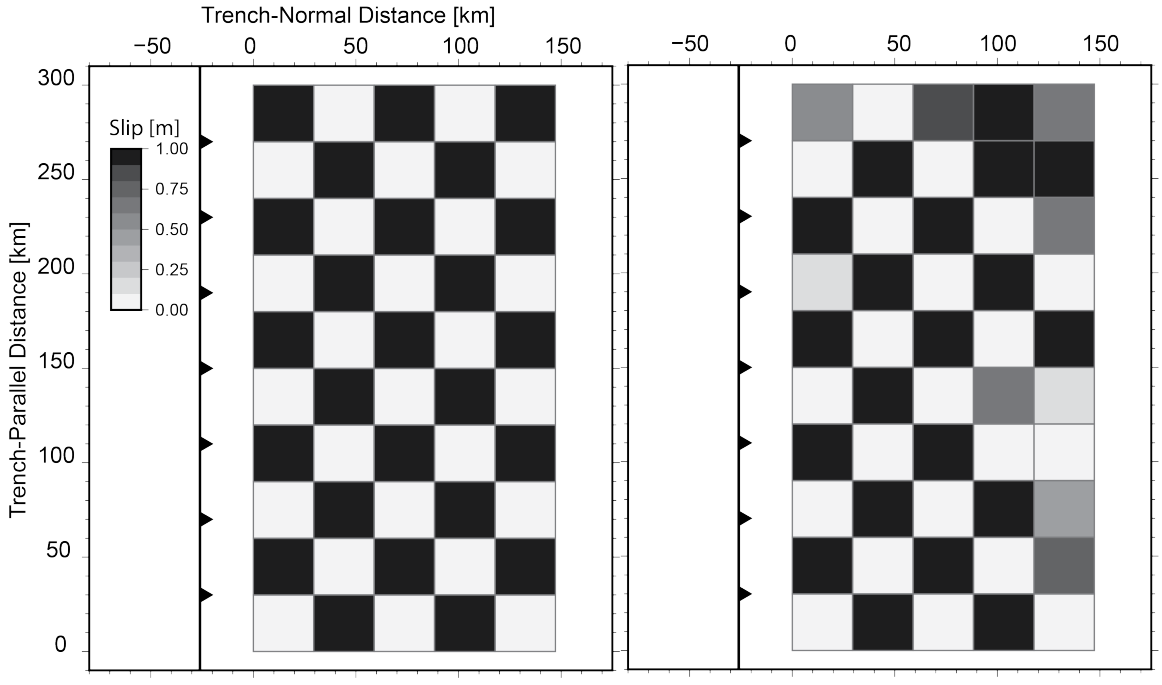

Figure 2.5. Tsunami Checkerboard test results for unwindowed (left) and windowed (right) data.

To better replicate the limitations of real tsunami data, we illustrate using a windowed time series. In Figure 2.4b, the same gauge is used as in Figure 2.4a but within a window that only includes the first few wavelengths of the waveform—a windowing length that is typical in recent tsunami modeling studies [*An et al*, 2014; *Gusman et al*, 2014; *Li et al.*, 2016; *Williamson et al.,* 2017; *Adriano et al.,* 2018]. After the latter part of the time series has been removed it is only sensitive to part of the spatial domain. Therefore, the location of the gauge with respect to the fault plane affects the resolution. The subfault generated Green's Functions containing waves with the earliest travel-time to the gauge will maintain high resolution, as they are retained in the time series window. In contrast, waveforms that are sensitive to subfaults further away may no longer be included when using short windowed observations. Checkerboard tests using windowed tsunami waveforms also highlight the variability in resolution through a loss in the coherent checker pattern (Figure 2.5).

If one station is too few to resolve the spatial domain, then a second gauge (if available) should be included. However, if the additional station is from the same azimuth as the first station, it will likely be windowed over the same region to exclude propagation uncertainties and therefore will be sensitive over a similar region. If possible, a secondary station from a different azimuth should be used to increase the sensitivity of the areas excluded from the first station. The exact difference in azimuth required to be sensitive to different parts of a model space is highly dependent on the model geometry, the location of the first gauge, and the location of possible nearby coastlines and should be treated on a case by case basis. In Figure 2.6 a second open-ocean gauge located 90 degrees from the

first gauge (with respect to the center of the fault plane) is included to highlight the increase in resolution that can be attained.

In real finite-fault models, data availability is a factor that is largely outside of the modeler's control. While a single DART gauge can be sensitive over a larger region than a single GNSS station, at 60 stations worldwide, there are significantly fewer DART gauges. Even if cabled arrays such as those offshore Japan and Canada are included in the analysis, the number of available stations is still highly location limited. In the Pacific, DART gauges are present in a nearly continuous arc from the Kuril Islands across the Aleutian Islands and south towards central Chile. The benefit of this density is that most of this arc includes a DART gauge every 100-200 km. Assuming reliable instrument performance, any earthquake rupturing in these regions should be within range of two obliquely located sensors, providing sufficient resolution. However, tsunamis generated near southern Chile and New Zealand only have possible data sources in one direction.

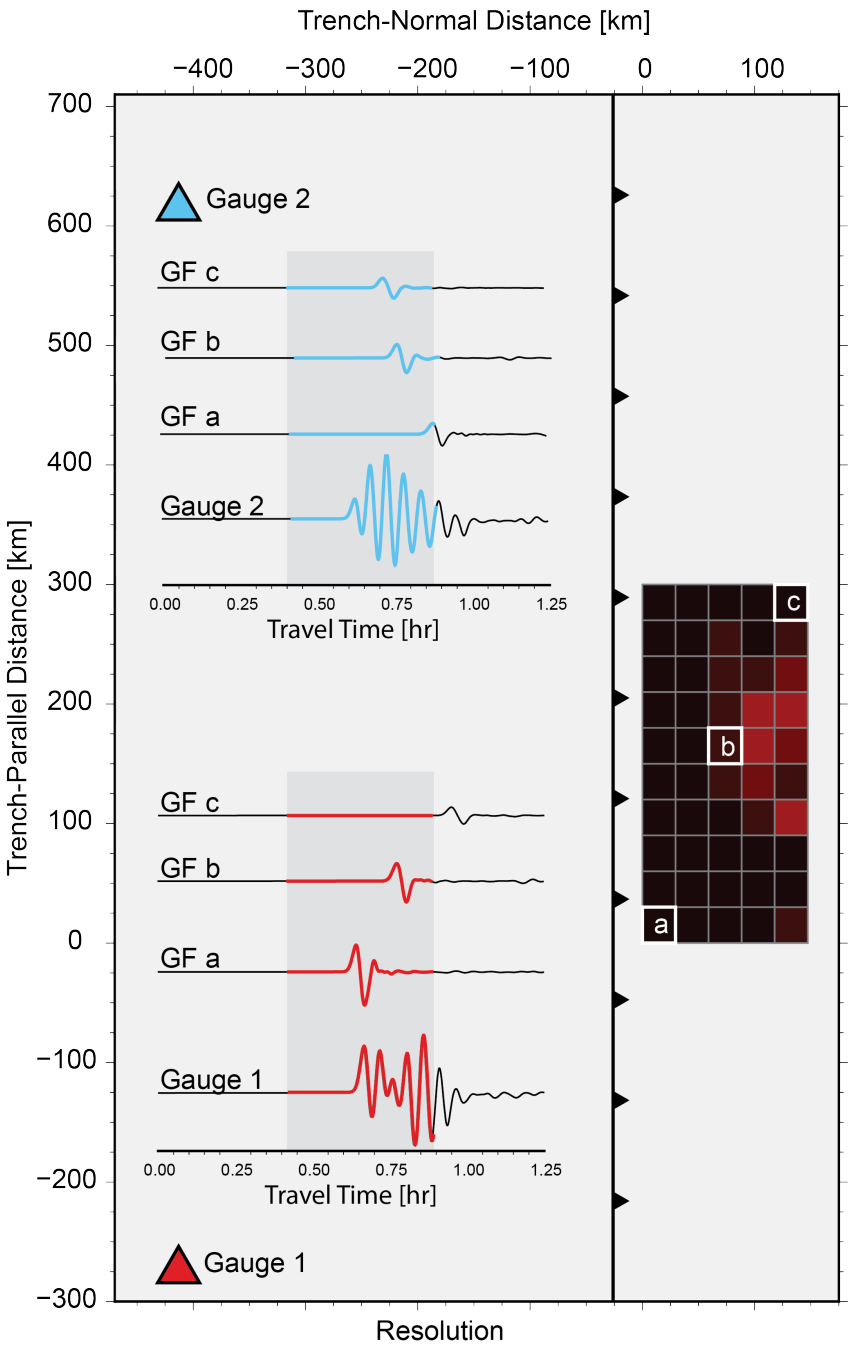

Figure 2.6. Resolution achieved through a multiple gauge tsunami inversion. The same windowed data from Gauge 1, shown in Figure 3b is used. In addition, the waveform from gauge 2- located at a different azimuth is also incorporated. The observation at gauge 2 as well as the windowed time series from each of the three subfaults (a,b, and c) are shown in blue.

Just as prior work has constrained the size of resolvable features for geodetic datasets [*Page et al.,* 2009; *Barnhart and Lohman*, 2010; *Atzori and Antonioli*, 2011], tsunami data can be assessed per model to determine the scale of resolvable features. The spread of values on the off-diagonal components of **R** indicate the interdependence of adjacent parameters to the one analyzed. For finite-fault studies, this amounts to the dependence of the subfault analyzed to the slip on the surrounding subfaults. For a fully resolved parameter, the interdependence with the surrounding subfaults is zero. But for a poorly resolved parameter, the interdependence will extend over a wide area around the subfault in question [*Funning et al*., 2007]. This limits the size of features in the slip model that can be resolved to the size of the spread.

Rather than exhaustively analyze the interdependence of each subfault to its surroundings, a general resolution spread can be easily derived. The use of the resolution spread parameter, r_i, quantitatively indicates the smallest resolvable feature in the model through:

$$\boldsymbol{r_i = \frac{L}{\sqrt{R_i}}} \tag{4}$$

Where L is the length scale of the subfault and R_i is the diagonal component of the matrix corresponding to the i^{th} parameter [*Funning et al.*, 2007]. A perfectly resolved model can determine features equal to the size of the discretized subfault. A poorly resolved area will only be able to resolve coarser features. A poorly resolved model is analogous to the highly interdependent case using the off-diagonals of **R**.

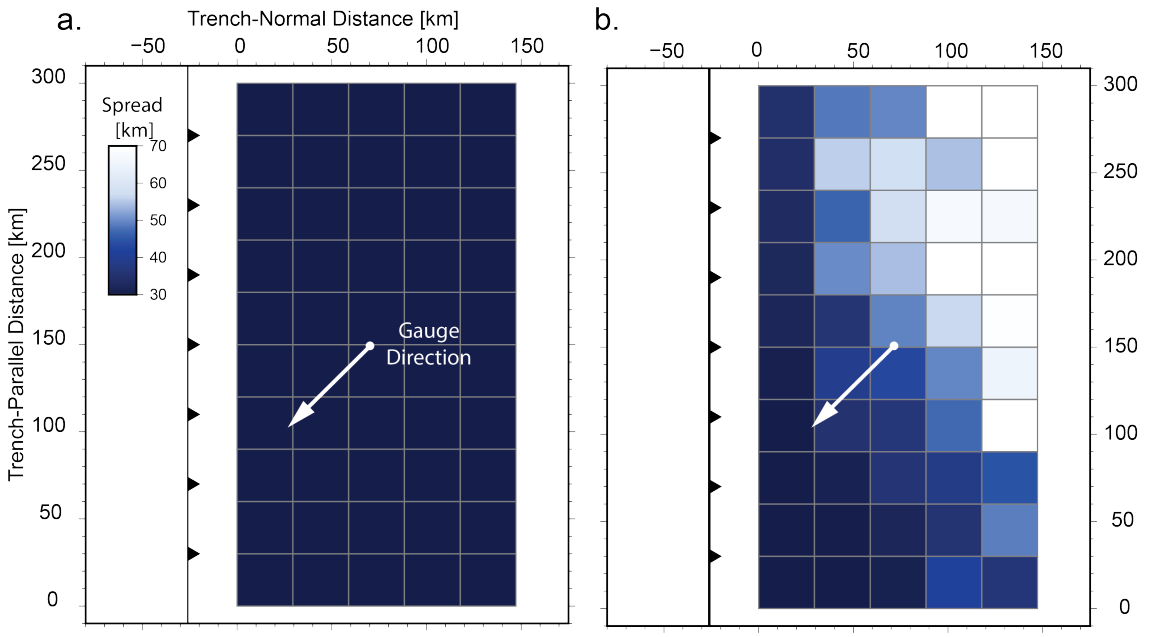

Figure 2.7. Resolution spread, r_i, achieved from the tsunami inversions highlighted in Figure 2.4. A. Resolution spread achieved in the 'idealized' dataset case- spread equates to 30 km (same as subfault size) across spatial domain. B. Resolution spread in windowed time series inversion. Lighter colors indicate a greater spread. The greater the spread, the less detail that can be resolved.

The resolution spread parameter is applied to the two scenarios discussed from Figure 2.4 and presented in Figure 2.7. For the ideal, yet physically improbable case of a fully resolved spatial domain, as shown in Figure 2.7a, the smallest resolvable feature over the entire spatial domain is the size of the subfaults being used (Where R_i approaches 1). Further testing in any model can be achieved by reducing the *a priori* subfault size and reassessing the resolution spread until the smallest subfault size is equal to the smallest possible spread for any area. This is particularly true for geodetic data, which do not have a subfault size limitation as is true with tsunami data. When windowing the tsunami time series, the resolution spread becomes extreme in the furthest reaches away from the instrument (Figure 2.7b) as resolution is low. While the most ideal resolution for this subfault size is 30 km, in poorly resolved zones, the smallest resolvable feature equates to

over 70 km. A poorly resolved zone that has a large dependence on adjacent subfaults can still produce a solution with fine-scaled features. But those fine scale features should not be considered reliable.

2.6 Discussion

Not highlighted thus far in this study, is the open-ocean tsunami waveform sensitivity to subfaults that occur under land. In these instances, the deformation generated at the surface will have little effect on the water column as the primary zones of deformation are subaerial. As these rupture zones largely lie near deeper contacts along the subduction megathrust interface, fault rupture that occurs under land and along the megathrust, in most environments will likely be deeper (>40 km) and surface deformation will be distributed over a rather large area, making independent smaller subfaults more difficult to independently resolve. While tsunami waveform data would still be limiting here, on-land geodetic data can potentially have a high resolution of larger subfaults, if available.

In earthquake rupture studies, where the 'true' slip distribution is unknown, one widely used metric for determining model correctness is data misfit. A poorly resolved model may appear to adequately fit the data (of which it is insensitive to), but will not necessarily be correct. A multitude of non-unique and highly diverse slip-distributions could equally fit the data [e.g. *Olsen and Apsel*, 1982; *Beresnev,* 2003] if a substantial portion of the model is in null space. Even though a 'true' slip distribution will never be known, knowledge of the model resolution to avoid putting confidence in null-space solutions is key.

The continued use of slip models following their publication highlights why resolution tests are vital for interpreting finite-fault model results. Understanding which

areas in the model have poor resolution can provide insight as to which slip features can be confidently trusted, and which features may be artifacts. If part of the model space is of too low a resolution, then parameters there are not sensitive to the dataset and should be disregarded. Solutions in these low-resolution zones (null-spaces) can vary from incoherent patterns to large, improbably scaled levels of slip, all of which will have no bearing on the overall fit of the data. Therefore, erroneous interpretation of solutions from the null-space in a final finite-fault result should be avoided. Without careful consideration of model resolution, finite-fault results incorporating data-insensitive zones of slip can easily shape our understanding of subduction zone seismicity. It is common following large earthquakes to assess the change in stress in the area surrounding the rupture zone [*Luttrell et al.,* 2011] as well as how modeled slip behavior affects the presence of seismic gaps [*Lorito et al.,* 2011; *Moreno et al.,* 2012; *Métois et al.,* 2016] with the aid of slip models. These models, without proper data handling, could be potentially dangerous if used by non-experts for regional interpretation of seismic or tsunami hazard.

While tsunami datasets lack resolution on land and geodetic datasets largely are insensitive to far offshore slip, the increasingly popular joint inversion of both datasets provides a potentially rich dataset that can be used to better understand of slip over the entire seismogenic zone. This can refine our understanding of where we do and do not see slip, particularly in the shallow semi-aseismic portion of the megathrust. It is important to point out that earthquake ruptures rarely behave as fully off-shore or fully under-land events. Both datasets, geodetic and tsunami, will be sensitive to at least a small portion of the rupture domain. Outside of each dataset's region of sensitivity, resolution does not abruptly end but does become limited.

2.7 Conclusion

Many studies integrate multiple new datasets in finite-fault source inversion to allow for better understanding of slip distribution along subduction zones. With the addition of off-shore datasets, such as open-ocean tsunami waveforms, it is important to understand not only the benefits the data provides to a model, but also the limitations. This is partially achieved by analyzing how the sensitivity of tsunami and geodetic datasets vary with location and treatment. Geodetic data is highly sensitive to deformation occurring in its immediate (within 40 km) vicinity. However special care needs to be given to modeling megathrust rupture with GNSS data when a) the depth between instrument and fault plane exceeds 30 km and b) the distance between instrument and offshore slip exceeds 40 km. In order to model slip in the near-trench environment with geodetic data, either offshore GPS-acoustic or land proximal to the rupture zone should be employed to maintain resolution. In conjunction with the use of a nearby and sensitive dataset, the scale of fault patches used in finite-fault modeling needs to be coarse enough to reduce the impact of slip artifacts. This can be quantified by analyzing the resolution spread which will vary as subfault size changes.

Open-ocean tsunami data provide excellent resolution offshore when data is available. However, data sensitivity is directly linked to how the data is processed. Windowing, which is employed to reduce un-modeled effects can in the process discard useful information about slip. The smaller the window that is used for the tsunami time series inversion, the small the area on the fault plane that each open-ocean gauge is sensitive to. However, the inclusion of larger windows of the tsunami waveform for inversions introduces uncertainties in the propagation path and un-modeled effects such as

energy loss from coastal reflections. Additional care should be used in the treatment of time series data from gauges located more than 1000 km away from the source zone, as the accumulation of errors in modeling the bathymetry, wave dispersion, and elastic loading can interfere with the model solution [*Watada et al.,* 2014]. A very positive attribute of the tsunami dataset is that despite the limited number of gauges available, only a couple of well-placed sites are necessary to obtain well-resolved fault plane solutions—a number far lower than the number of GNSS stations normally required on-land, while still missing much of the off-shore action.

The understanding of where a model is well resolved is just as important as understanding where it is not. Poorly resolved areas- which may lack data, should be analyzed with the understanding that the scale of features presented in the inversion may not be robust. Through the use of multiple different datasets, particularly through the inclusion of both land sensitive and seafloor sensitive data, a comprehensive understanding of slip from the shallow near-trench environment through the entire seismogenic interface may be achieved.

CHAPTER 3. RECONSTRUCTION OF COSEISMIC SLIP FROM THE 2015 ILLAPEL EARTHQUAKE USING COMBINED GEODETIC AND TSUNAMI WAVEFORMS

3.1 Abstract

On 16 September 2015, a moment magnitude (M_w) 8.3 earthquake struck off the coast of central Chile, generating a large tsunami with nearby coastal wave heights observed on tide gauges in Chile and Peru of up to 4.7 m, and distal observations of over 40 cm in the Kuril Islands across the Pacific Ocean. Through a trans-coastal geodetic study, including tsunami time series recorded at open-ocean pressure gauges, sub-aerial deformation observed through Interferometric Synthetic Aperture Radar (InSAR) from the Sentinel-1 A satellite and continuous GPS, we identify the location and extent of coseismic slip. We find that most coseismic slip was concentrated in a patch immediately offshore, with little modeled slip near the trench. This result satisfies the tsunami waveforms measured in the deep ocean north of the rupture area, with wave heights up to 10 cm. While the event exhibits some features of a slow tsunami earthquake (moderately large tsunami and possible slow second-stage rupture), our inversion results do not require substantial near-trench rupture. However, the prevalence of large and shallow thrust along subduction megathrusts along central Chile raises the question of the likelihood of future such events and the implications for future hazardous tsunamigenic earthquakes.

3.2 Introduction

Over the past century, the Peru-Chile trench has produced many great tsunamigenic earthquakes and has been the focus of several studies of subduction zone earthquake excitation, tectonic strain accumulation, and interseismic coupling [*Vigny et al.,* 2009; *Moreno et al*., 2010; *Moreno et al.*, 2011]. This propensity for large events is in part fueled by the region's rapid plate motion. In the vicinity of central Chile, the Nazca plate subducts

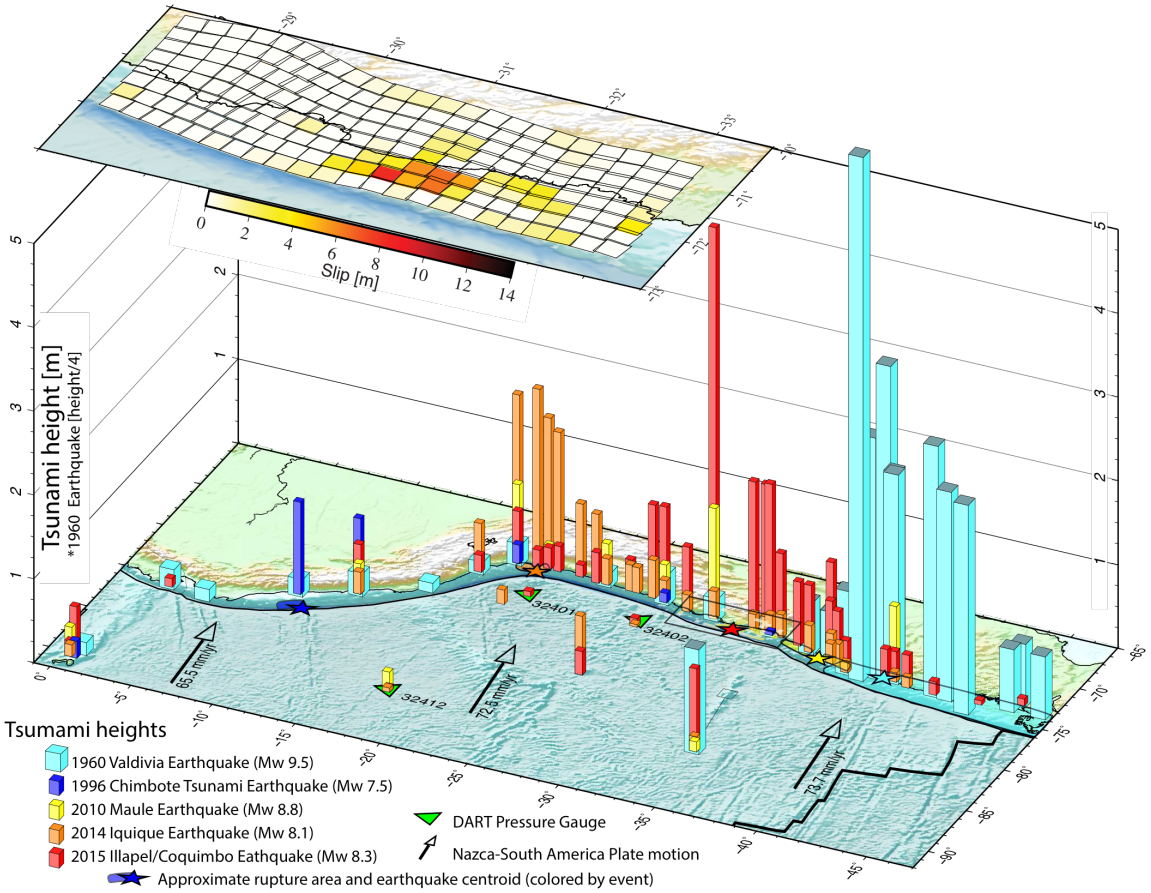

Figure 3.1. Regional map of past tsunamigenic earthquakes and their generated tsunamis. The epicenter of the 1960 and centroid location for later events [*Ekström et al.*, 2012] with the approximate rupture area are shown by colored stars and transparent polygons beneath [*Bourgeouis et al.*, 1999; *Lorito et al.*, 2011; *Hayes et al.*, 2014]. For each event, the regional tsunami wave height measured by local tide gauges and deep-water pressure sensors (green triangles) are shown as columnar bars (1960 is augmented by eyewitness accounts (gray tops, and are all divided by 4 to stay on scale) [*NGDC,* 2016]. The Nazca plate motion relative to a stable South American plate is also shown (black arrows) [*DeMets et al.*, 2010]. Inset figure: preferred fault plane solution using GPS, InSAR, and tsunami datasets.

beneath the South American plate with a rate of convergence of 74 mm/yr [*DeMets et al.,* 2010]. Many of the more recent earthquakes in the region have produced tsunamis that have been recorded at coastal tide gauges as well as at deep ocean pressure sensors as shown in **Error! Reference source not found.**

One problem in determining the extent of slip from megathrust events is having a clearly resolved domain that extends past the coast to the trench. This shallow, submarine zone is oftentimes poorly resolved through purely geodetic datasets, where many different rupture models can provide equally satisfactory fits to observed data. However, the inclusion of tsunami data, particularly as recorded away from the source at deep ocean pressure gauges, adds a resolvability in this shallow zone that is sensitive to tsunami excitation.

The tsunami generated from a large earthquake is a function of the amount of slip occurring underwater, which for many cases translates to the amount of slip occurring within a shallow (< 30 km depth) part of the megathrust. Tsunami waveforms are therefore a good proxy for understanding this shallow, near trench environment, which for many regions lacks direct observation by instrumentation. This can be particularly important for a special subclass of earthquakes, aptly named tsunami earthquakes, which generate a much larger tsunami than expected from the derived magnitude, and are often deficient in radiating seismic energy while maintaining a characteristically slow rupture propagation [*Kanamori,* 1972]. The 1996 Chimbote, Peru earthquake, with a M_W of only 7.8, produced one meter-level waves locally around Peru and Northern Chile, and waves up to 0.3 m near Easter Island, approximately 3800 km away, with up to a maximum run up height of almost 5 m. The disproportionately large tsunami generated by this event is partially a function of

its rupture along the shallow part of the megathrust [*Heinrich et al.,* 1998]. Its source location and its deficiency in radiating high frequency energy led this event to be categorized as a tsunami earthquake by *Newman and Okal* [1998].

However, other tsunamigenic earthquakes in this region were recorded transoceanically without falling into the tsunami earthquake subclass. The largest-ever instrumentally recorded earthquake, occurring near Valdivia, Chile in 1960, generated a large and devastating transoceanic tsunami. Eyewitness observations near the source region suggest 10 to 15 m waves along the coast [*NGDC,* 2016]. On a regional scale, tide gauge recordings near the city of Concepción topped out with zero-to-crest amplitudes of over 2.5 m, and tide gauges in northern Chile and Peru (2,000 to 3,000 km away) recorded waves between 0.5 and 1 m in height [*NGDC,* 2016].

More recently, the 2010 M_W 8.8 Maule earthquake ruptured a patch of the megathrust just to the north of the 1960 Valdivia earthquake. In the near field, tide gauges recorded waves with amplitudes around 1 m, with the largest wave = 1.3 m occurring in a bay near the city of Coquimbo. Far field recordings in Peru were less than 0.5 m. Maximum on-land run-up heights reached 29 m at Tirua, 250 km from the source region. Nevertheless, the earthquake and tsunami created over 30 billion dollars in damage and resulted in over 500 causalities in Chile [*USGS report; Fritz et al.,* 2011]. Additionally, in 2014, the M_W 8.1 Iquique earthquake in northern Chile, while smaller, also produced a regionally observable tsunami [*An et al.,* 2014; *Gusman et al.,* 2015].

The latest tsunamigenic addition to the Peru-Chile catalog is the 16 September 2015 M_W 8.3 Illapel earthquake. This event nucleated offshore from Coquimbo Province

(approximately 31.57° S and 71.67° W) at approximately 22:54:32 UTC. While the earthquake was smaller in size compared to other contemporary tsunamigenic earthquakes near Chile, including the 2010 Maule earthquake just to the south, it produced a locally large tsunami (up to 4.7 m near Coquimbo as measured by a local tide gauge). The tsunami was transoceanic, with tide gauges recordings throughout the Pacific basin, including Oahu, Hawaii (0.23 m), Kuril Islands, Russia (0.44 m), and Aburatsu, Japan (0.22 m).

The wide spectrum of tsunami generated by earthquakes on the Peru-Chile trench provides a rich and often under-utilized dataset for static source inversions. While previous studies of the Illapel earthquake have incorporated data from the tsunami, either from the nearby deep ocean pressure gauges, or the numerous tide gauges along the coast, this data has been used exclusively through forward models as a constraint on seismic or geodetic inversions or as a validation of a particular model [*Calisto et al.,* 2016; *Heidarzadeh et al.,* 2015; *Li et al.,* 2016*; Tilmann et al.,* 2016]. However, for many model results, the forward projection of the model results as a tsunami and its comparison to the observed data from deep ocean gauges is out of phase with observations by a few minutes and often miscalculates the peak amplitude of the first wave, as was shown well in *Calisto et al*. [2016]. While it is unlikely for any one model to well fit all datasets, this consistent phase delay should be addressed as it appears to transcend the type of tsunami propagation model used and the handling of the observed data.

To characterize the 2015 Illapel earthquake, we use Line-Of-Sight (LOS) Interferometric Synthetic Aperture Radar (InSAR) observations, static offsets from continuous GPS, and tsunami time series from the four nearest Deep Ocean Assessment and Reporting of Tsunamis (henceforth, DART) pressure gauges. As was originally shown

in a combined tsunami-InSAR inversion by *Gusman et al.* [2010], we find that the combination of both land-based geodetic and tsunami datasets, which span the shoreline, allows for maximum resolution of the earthquake slip environment across the subduction megathrust. As we detail below, through a joint inversion of both data types, we find that the maximum coseismic slip occurred in the down-dip near-coastal environment, providing the best fit in phase and amplitude to deep ocean time series and on-land static deformation. This moves the locus of dominant slip away from the near-trench environment. While this provides a better fit to the tsunami data, it is in contradiction to some past geodetic and seismic studies on the same event [*Heidarzadeh et al.,* 2015; *Lee et al.,* 2016; *Li et al.,* 2016; *Ruiz et al.,* 2016; *Ye et al.,* 2016].

3.3 Data

In this study we incorporate data from four nearby DART pressure gauges. Each gauge records the pressure of the overlying water column and translates this to water column height using a conversion constant at 15 minute, one minute, or 15 second sampling frequencies depending on if each gauge is in standby or a triggered event mode. With a sensitivity of less than one millimeter in deep-water, DART pressure gauges are ideal for measuring long period, low amplitude tsunami waves. Unlike coastal tide gauges which record the tsunami as it interacts with the coastline, leading to non-linear effects such as harbor resonance, DART gauges, because they are located in the deep-ocean, are largely immune to small scale bathymetric changes. We removed tides recorded at each station through polynomial fitting, then filtered the signals to remove high frequency surface wave energy. Additionally, we windowed each time series to only include the tsunami's arrival and first wavelength in the signal used for the inversion. This is of particular importance

for the two nearest stations, where waves reflected from the coast appear early on in the time series.

We also use the LOS displacement field derived from a pair of descending track scenes (24 August and 17 September 2015) recorded by the Sentinel-1A SAR satellite, and processed by the European Space Agency [*Copernicus Service information,* 2015]. The resultant InSAR image shows a maximum of 150 cm of ground deformation in the LOS direction. While we correct for changes in LOS look angle, we also tested a constant angle of 41° off nadir, near the maximum deformation and found the difference to be negligible.

Because the data density and interdependence of pixels is extremely high (on the order of 10^7 pixels per image), it was necessary for us to down-sample the field of data to make the image manageable for computational inversions. To do so, we use a two-dimensional Quadtree decomposition similar to *Jónsson et al.* [2002], that retains more information in environments that have more significant change. We require that each geographically oriented quadrangle containing InSAR signals is split into four smaller quadrangles whenever the variance in LOS displacement is greater than a set tolerance level (5% difference). For the remaining 1,200 boxes, we assign the average displacement to the 'center of mass' position of coherent pixels. The resulting down-sampled image, overlaying the original displacement field, is shown in Figure 3.2. Because the second pass follows one day after the event, any post-seismic signal is likely to remain small. Furthermore, because most observations of early afterslip occur primarily up-dip of the

main rupture along subduction zones [e.g. *Hsu et al.,* 2006; *Malservisi et al.,* 2015], we suspect the land-based data to be more representative of co-seismic rupture.

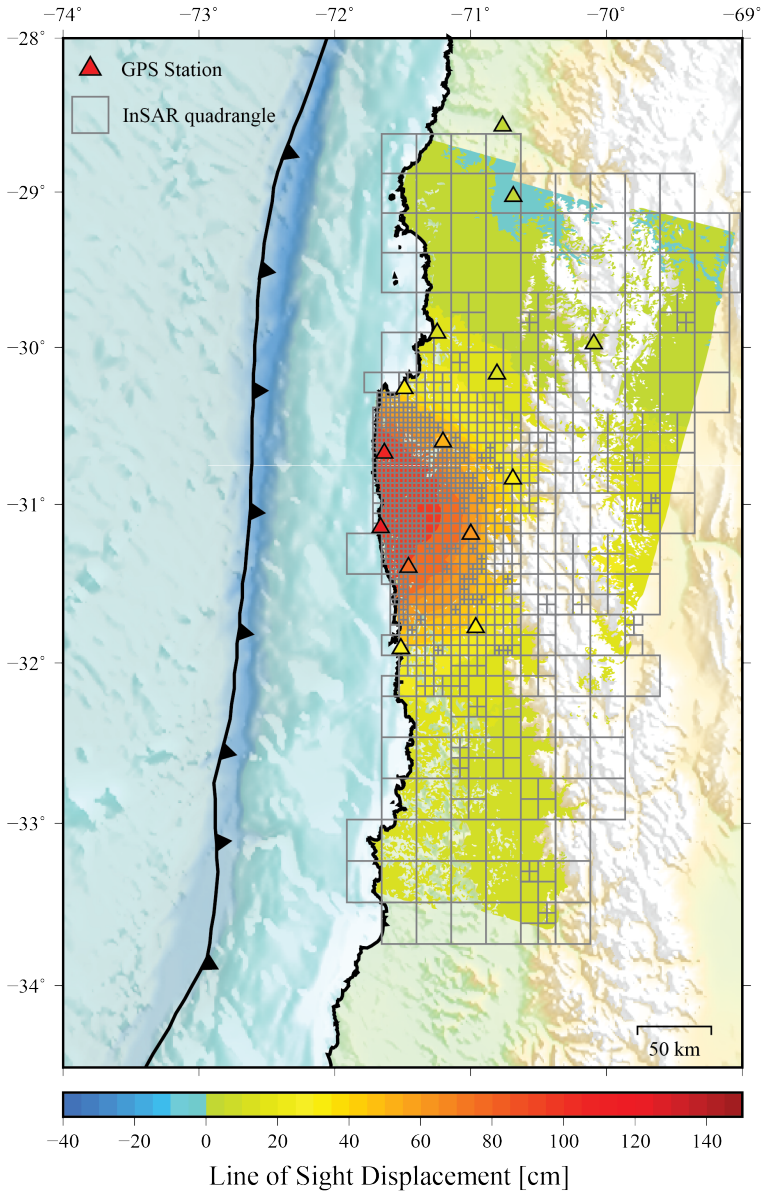

Figure 3.2. Regional InSAR derived displacements in the direction of satellite line-of-sight with Quadtree discretization (grey boxes). Each box represents one point used in the inversion. Triangles indicate the location of the nearby GPS stations. The color of each triangle is the magnitude of displacement of the three component GPS when translated into the line-of-sight direction. The matching colors between the InSAR displacement field and the GPS shows that both datasets are consistent with each other.

Additionally, we incorporate static offsets from sixteen three-component continuous GPS stations, located in central Chile, operated by the National Seismological Center of the Universidad de Chile, with static displacements reported in *Ruiz et al.* [2016]. The dataset shows a consistent seaward motion by all stations and a small, but complex and comparably small vertical signal of uplift and subsidence at the coastal stations.

When constrained to the use of only land-based geodetic instruments such as GPS and InSAR, the shallow subduction zone region is generally too far offshore to be resolvable in distributed-slip (i.e., "finite fault") inversions. While seafloor geodetic instruments are feasible, they are often cost prohibitive and thus few regions currently have the infrastructure in place, causing many communities to forgo their use [*Newman,* 2011]. This leads to difficulty in constraining slip in this highly hazardous, but in these cases poorly resolved, zone. By supplementing this dataset with ocean-based observations, like tide gauge or pressure gauge time series, we find that spatial resolvability of the offshore region increases substantially (see Model Resolution, below).

3.4 Methods

3.4.1 Model Geometry

We describe the source region with a three-dimensional curvi-planar fault geometry. We then discretize the modeled fault plane into a 575 x 200 km surface, consisting of a 23x8 grid, with individual patches of dimensions 25 km along strike and 25 km along dip. The strike and dip of the fault interface vary for each patch, approximating

the profile created from Slab 1.0 [*Hayes et al.,* 2012]. While the inclusion of a strike variability does cause a small amount of overlap of patches, the total overlap is negligible in calculating the seismic moment.

3.4.2 Inversion Techniques

We calculate Green's functions for InSAR LOS displacements and GPS static offsets through an analytic solution to the elastodynamic equations for rectangular dislocations in an elastic half space [*Okada,* 1985]. For DART data, we generate Green's functions relating fault slip by combining the vertical surface deformation from Okada [1985] with the tsunami propagation model, JAGURS [*Baba et al.,* 2015; *Allgeyer and Cummins* 2014]. JAGURS is a finite difference method model that, in addition to solving the non-linear shallow water wave equations, has the ability to incorporate elastic loading, seawater compressibility, gravitational potential change and Boussinesq dispersion into the propagation simulation. In order to account for hydrodynamic effects that alter the pattern of displacement transmitted from the seafloor to sea surface, we applied a smoothing filter [*Kajiura,* 1963] was applied to the seafloor displacement of each subfault before it was translated to the sea surface. Finally, we perform a linear inversion for positive dip-slip motion (thrust) along our fault geometry, bounding to be less than 20 meters per fault patch. While the tsunami propagation code is non-linear, it is well behaved for open-ocean tsunami propagation, particularly in the near-field, making it amenable for inclusion in a bound linear inversion.

We relate our geodetic and tsunami Green's functions to fault interface slip through the model GTdef developed by *Chen et al.* [2009] and following *Jónsson et al.* [2002]. The model solves the linear system of equations using

$$\begin{bmatrix} w\,d \\ 0 \end{bmatrix} = \begin{bmatrix} w\,G \\ \kappa^2 D \end{bmatrix} m \tag{5}$$

where d is the observed data vector, G is the Green's function matrix, m is the vector of unknown slip on the fault, D is a finite difference smoothing operator that relates each patch with a weight regulated by κ. The Green's function matrix is composed of tsunami waveforms and static offsets from both LOS InSAR measurements as well as horizontal and vertical GPS measurements. Both the observation vector and the Green's function matrix are modified with a coefficient, w, representing measurement errors associated with each type of observation and a weight relating the different datasets. The total contribution of each dataset varies, with the number of discretized tsunami waveform data (10,800 points) exceeding Quadtree down-sampled InSAR data (1,200 points) and GPS data (16 sites x 3 components). To ensure comparable sensitivity between the tsunami and land-based geodetic data, we weighted the cumulative datasets equally for the inversion.

We regularize our solution using κ to force an interdependence between adjacent slip patches [*Harris and Segall,* 1987]. An increasing smoothing factor, acts as a trade-off with the misfit of the model. The misfit is determined as the root-mean square (RMS) of the weighted-residual sum of squares (WRSS). While an unconstrained model where each patch acts independently of its surrounds would theoretically provide the best fit to the observed data, solutions would be non-unique and would potentially provide unrealistically

rough results. Instead, we evaluate a range of unique models constrained by increasing κ (Figure S1), before choosing our preferred model, determined by evaluating the trade-off between model misfit and roughness.

3.5 Model Resolution

We approximate the spatial resolvability of our model using a "checkerboard test," consisting of 50 km by 50 km blocks with alternating predefined uniform slip magnitudes between 0 and 1 meter (Figure 3.3). Using these patches as input, we predict deformation at each data point for InSAR, GPS, and tsunami datasets as well as the combination of all three. We subsequently invert these synthetic data with our observed data error, and compare our inverted with our initial models. In areas where the checkerboard is retained, we have high resolvability.

The spatial resolution of the study region is assumed to vary due to a non-uniform distribution of observations. For geodetic (InSAR and GPS) checkerboard results, the best resolution is centered at 71.5° W and 31°S, about where the largest change in deformation both in InSAR and GPS offsets occurs. However, resolution is limited offshore and does not extend along strike through the study area. The tsunami dataset checkerboard result shows an excellent recreation of the checkerboard pattern offshore, but resolution is quickly lost for fault patches located under land, where slip would minimally affect the water column. The checkerboard for the combined dataset has good resolution for almost the entire study region, excluding a patch down-dip and to the north of the main region of deformation, where there are few GPS stations and a small amount of change in the InSAR

image, thus a smaller dataset. However, for the combination image, the checkerboard pattern was recovered for the region where we expect to see most slip from this earthquake.

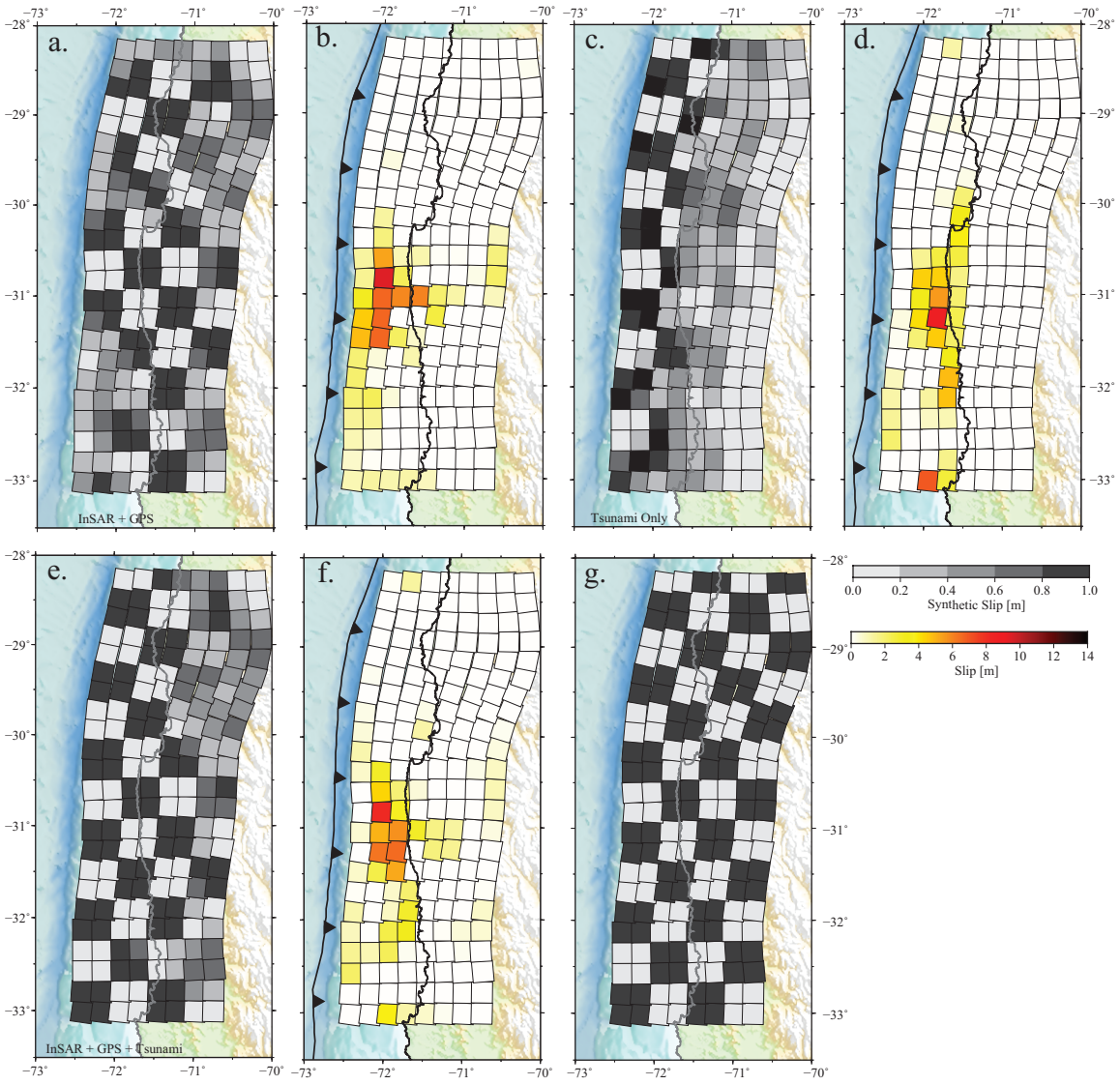

Figure 3.3. "Checkerboard" resolution tests. (a) geodetic only checkerboard solution, using only the InSAR and GPS datasets; (b) preferred model results from an InSAR and GPS dataset; (c) checkerboard solution incorporating only DART tsunami waveforms; (d) preferred model results from a tsunami dataset; (e) checkerboard solution using all available data. (f) preferred slip solution using all data; (g) initial checkerboard input with 50 x 50 km checkers alternating between 0 and 1 meter of dip slip; Solutions in b & c illustrate the spatial variability and limitations of using geodetic and tsunami datasets, respectively.

3.6 Results

The majority of slip occurred in one main patch immediately offshore but not reaching the trench axis. The peak slip in our preferred model reaches 11 meters, while the main patch of consistent slip extends about 125 km along strike and 50 km along dip. This peak slip measurement is an estimate of the slip in the smoothed model, the value has the potential to change with a different smoothing factor. Forward projections of the GPS displacement vectors, InSAR LOS displacement fields, and tsunami waveforms are shown in Figure 3.4, Figure 3.5, and Figure 3.6.

Our model is in good agreement with tsunami time series recorded at four nearby DART gauges (Figure 3.5), with little phase delay between the modeled tsunami arrival and the observed time series, and a consistent peak amplitude for the initial part of the tsunami, before the inclusions of coastal reflections. The fit of the model at the nearest gauge, DART 32402, also partially recreates the wave trough that was recorded about 50 minutes after the earthquake. This feature was not modeled in studies assessed in *Calisto et al.* [2016], *Heidarzadeh et al.* [2016], or *Tang et al.* [2016]. While the later, trailing part of the tsunami is not consistently recreated across all DART gauges, this part of the time series includes modulations of the tsunami from coastal reflections and inundation, which we do not confidently recreate in our tsunami Green's functions or forward tsunami model.

Forward projections of the geodetic data, both for the GPS stations and a recreation of the InSAR deformation both yield good results. The largest misfit within the geodetic

datasets occurs close to the coastline where the preferred model slightly under predicts deformation.

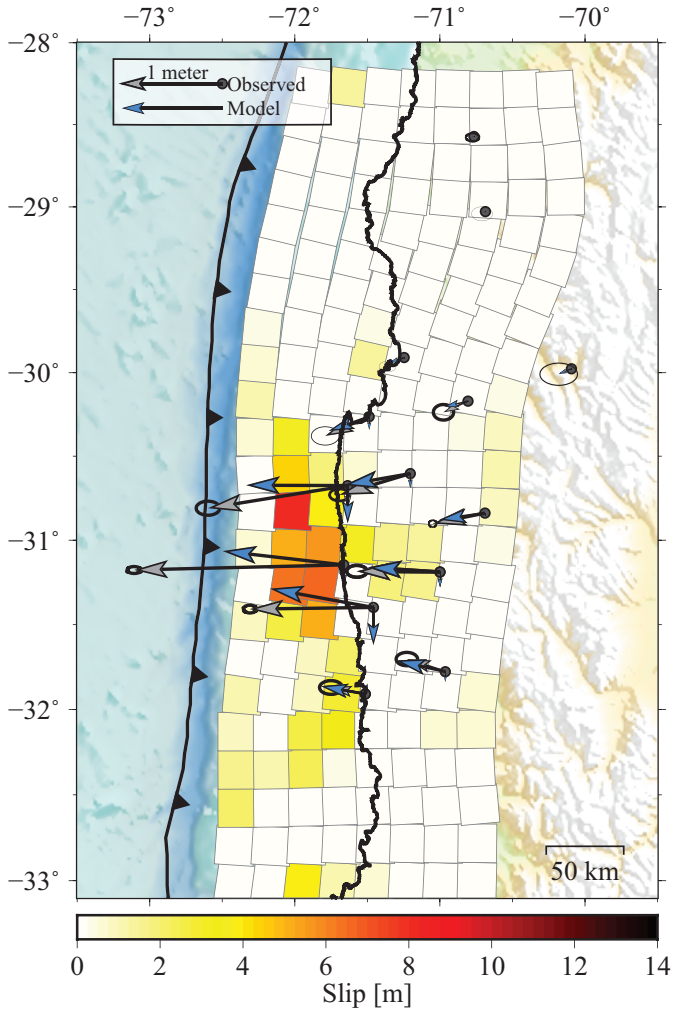

Figure 3.4. Observed (gray) and modeled (blue) horizontal and vertical coseismic GPS coseismic displacements superimposed on the preferred slip model

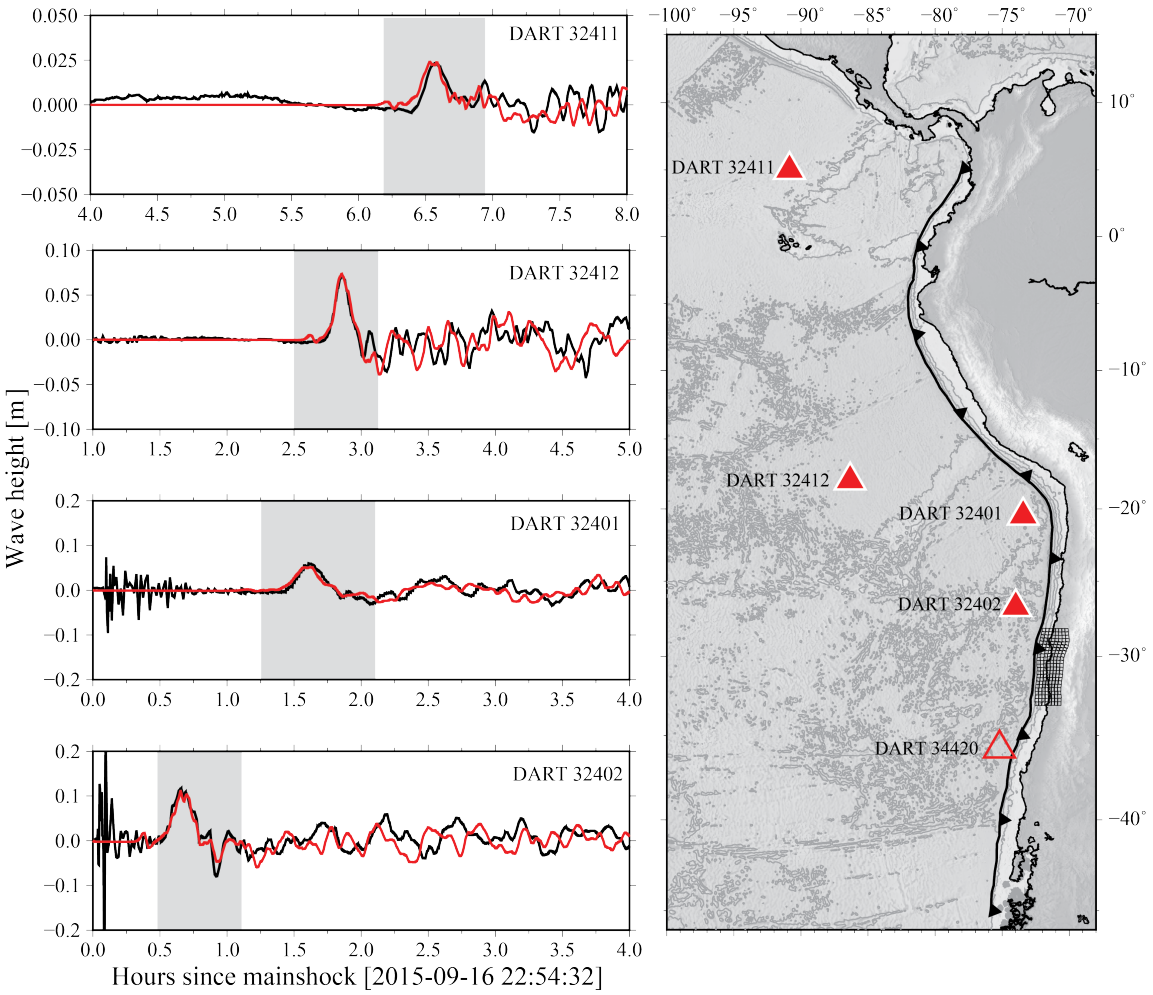

Figure 3.5. (a) Black line: recorded tsunami waveforms from the four nearest and active DART pressure gauges with timing relative to the mainshock. Red line: forward simulated tsunami result for preferred model. The gray boxes in each of the four subplots highlights the windowed region used in the inversion process. Regions were picked to include the first and largest amplitude part of the tsunami while excluding surface wave recordings and later coastal reflections. Both of the excluded effects cannot me modeled through our inversion process. (b) Geographic distribution of nearby DART gauges active during the earthquake (red solid triangles). The discretized fault plane is shown near 30°S. The hollow triangle outlined in red is the newest addition to the DART gauge fleet along the Peru-Chile trench, but was not active during the tsunami.

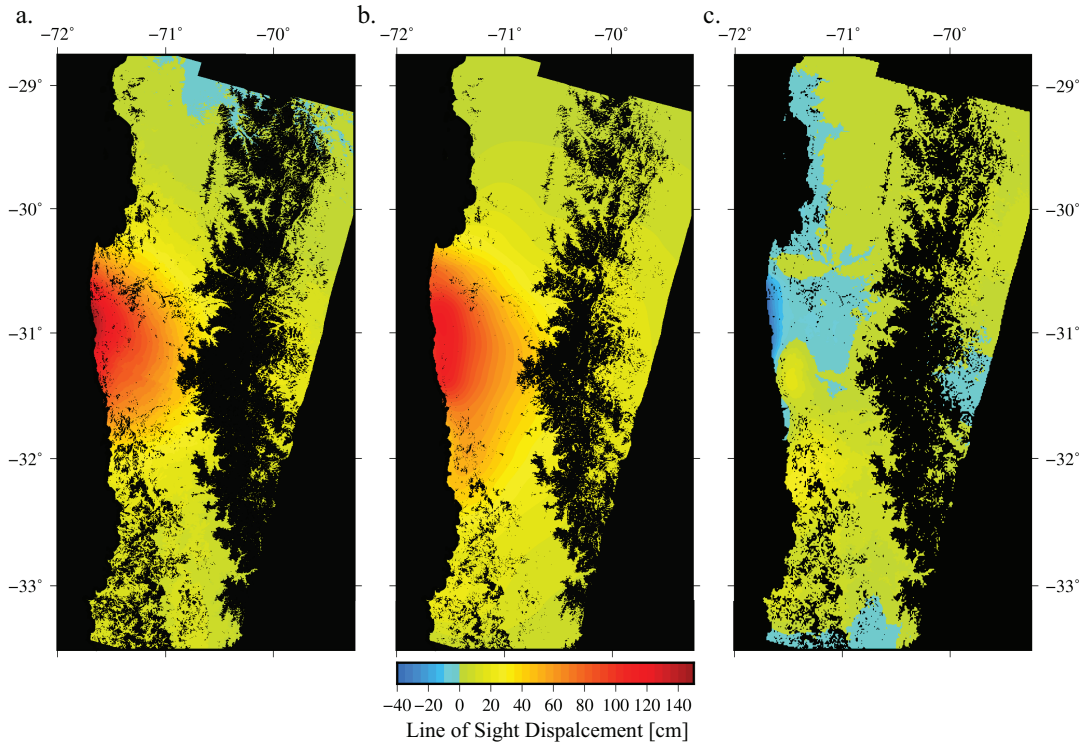

Figure 3.6. Comparison of InSAR line-of-sight (LOS) change for data and our preferred model. (a) Observed LOS displacement, repeated from Figure 3.2. (b) LOS projection of the preferred model results. (c) Residual LOS displacement, determined by removing the predicted (b) from the observed (a) signal.

3.7 Discussion

The addition of a tsunami dataset to the earthquake source inversion adds a spatial resolution to the solution, especially in the near-trench region. This is noticeable when comparing the arrival times of a tsunami at deep water gauges between models and observations. The inclusion of tsunami datasets also assists in constraining shallow slip,

which may not be resolved well with land based datasets, and may also constrain seafloor uplift in a complex and often poorly understood part of the subduction zone.

This region has poor azimuthal coverage of DART gauges, they are only located to the north of the rupture area and oblique to the directivity of the tsunami. While a new station was added directly south of the Illapel earthquake during the fall of 2015, which could potentially aid in constraining the location of slip with further confidence, it was not fully deployed until after the event. Located near the trench axis, the close proximity of the gauge to the megathrust reduced the delay between the earthquake and the arrival of the tsunami at the station, increasing the time available to assess the tsunami for far-field hazard warnings. It also provides an opportunity for real-time or near-real-time source inversions incorporating tsunami data, and possibly supplementing other real-time source characterization methods [*Benavente et al.,* 2016].

Ideally, the inclusion of trans-oceanic DART stations can aid in the modeling of offshore slip through additional observations over a wider azimuth range. However, this also requires the inclusion of the accumulating effects of dispersion and possibly the elastic loading of the seafloor from the propagating wave. These effects not only change the arrival time of the wave at far-field stations, when compared to linear long wave models, but they also distort the waveform itself [*Watada et al.,* 2014]. While it is possible to address some of these distortions [e.g. *Watada et al.,* 2014], we exclude use of the far-field tsunami waveforms because they are expected to have much less sensitivity to the details of the slip distribution than the near-field waveforms used here [*Geist and Dmwoska*, 1999].

Most earthquakes exhibit rupture speeds up to 3km/s in subduction zone environments [e.g. *Bilek and Lay,* 1999]. However, in the case of slow, tsunami earthquakes, rupture can be substantially reduced, down to as little as 1 km/s, greatly

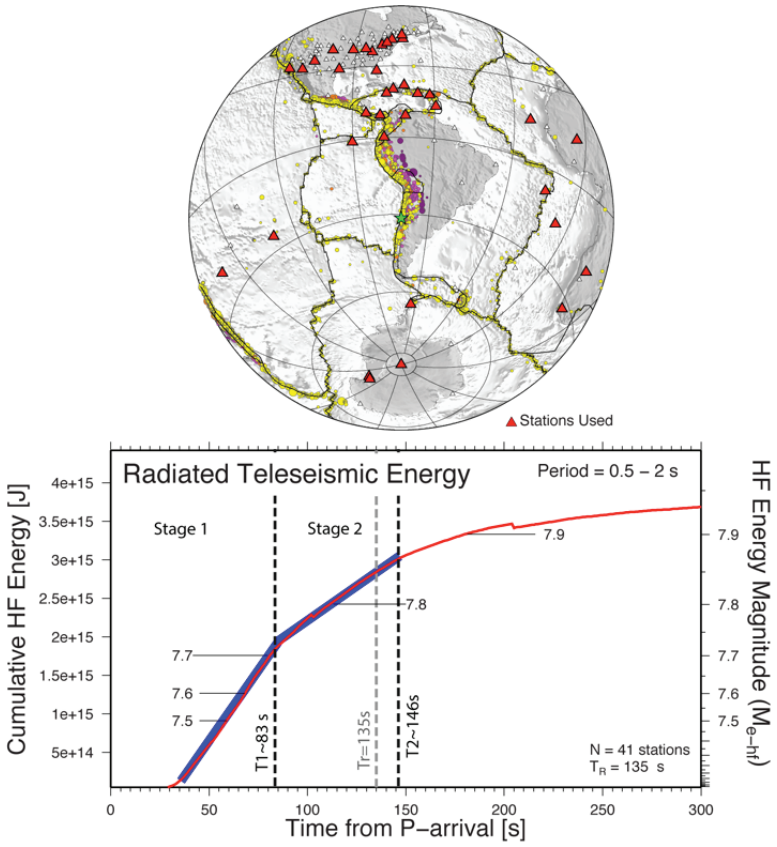

Figure 3.7. The cumulative high-frequency energy radiated from the Illapel earthquake is shown (red line) using data from 41 seismic stations available in real-time (red triangles in map) and automatically processed following *Convers and Newman* [2011]. The automated rupture duration, T_R (dashed gray line), two near-linear periods of growth (denoted by thick blue lines) and their termination times relative to the earthquake nucleation (dashed black lines). The cumulative energy is converted to a high-frequency energy magnitude, which appears deficient for this event, similar but more moderate than slow-rupturing tsunami earthquakes.

extending the duration of rupture [*Kanamori,* 1972], and substantially diminishing the propagated energy, as was the case in the 1996 Chimbote, Peru earthquake (Figure 3.1)[*Newman and Okal,* 1998]. The slowed rupture is sometimes attributed to slip in the shallowest portion of the interface near the trench [e.g. *Bilek and Lay*, 1999; *Polet*

and Kanamori, 2000]. Based on teleseismic energy back-projections, *Yin et al*. [2016] identified a substantial and slow delayed rupture component to the 2015 Illapel earthquake, extending between 80 and 130 s from the initial rupture, with the patch occurring up-dip of the initial nucleation, and very near the trench. Using a teleseismic inversion of the spectral contributions from the Illapel earthquake, *Lee et al.* [2016] similarly found a two-stage rupture process, but with moderately longer durations, the first lasting 100 s, and the second not terminating until about 250 s after the rupture initiation.

Examination of the real-time radiated energy growth, automatically ran at Georgia Tech using RTerg [*Convers and Newman,* 2011], shows that this earthquake does indeed exhibit complex, and delayed energy release that is discernable within the cumulative growth of high-frequency (0.5-2 Hz) teleseismically radiated P-wave energy (**Figure 3.7**). While the automated algorithm estimated the rupture duration, T_R, at 135 s using the cross-over between the rapid initial growth and the later slow-growth of high-frequency energy, the steeply-sloped growth phase uncharacteristically exhibits a break in the linear slope. Unlike most other earthquakes which exhibit a simple singular growth phase, this event has a more-rapid growth period that terminates at 83 s, followed by a more slowly growing phase that terminates near 146 s. *Newman et al.* [2011], using the 2010 Mentawai tsunami earthquake, identified that such a depressed growth is characteristic of slow rupture. Interestingly, these windows correspond well with the two periods found by *Yin et al* [2016], that also identified the second stage as growing more slowly. Furthermore, the real-time energy result culminated in a high-frequency energy magnitude, $M_{e\text{-}hf}$ =7.8 (corresponding to 3.0e15 J), 0.5 units smaller than M_W (8.3) as reported by gCMT. Such a feature is comparable to the deficiency in the Theta parameter ($\Theta = \mathrm{Log}_{10}(E/M_0)$), originally

described as characteristic for slow tsunami earthquakes in *Newman and Okal* [1998]. Thus, while our joint inversion that includes DART data suggests the most up-dip component of the megathrust is not responsible for the tsunami generated, a number of results strongly support the likelihood of a slowed, and possibly near-trench component: 1) the back-projections of *Yin et al.* [2016]; 2) the spectral analysis of *Lee et al.* [2016]; and 3) the slowed secondary growth and reduced overall earthquake energy following *Convers and Newman* [2011]. While it is likely that the second and slowed phase of energy release contributed to the overall tsunami, it is not clear that significant fractions of the slip for this component occurred near the trench. If the slowed phase did occur near the trench, it is possible that the dip angle is so low that it had an inappreciable contribution to tsunami generation.

3.8 Conclusion

We conduct a trans-coastal joint inversion to solve for coseismic slip along the subduction megathrust using deep-ocean pressure gauge tsunami time series, continuous GPS, and Sentinal-1A InSAR data following the 2015 Illapel earthquake. By supplementing the traditional land-based geodetic slip inversion with a tsunami dataset, key information about the region between the trench and the coast can be incorporated, substantially increasing the resolution domain for megathrust events. Our preferred result has a large concentration of slip near the coastline and down-dip from the trench axis, but still under a submarine environment, leading to tsunami excitation. Our model is in good agreement with tsunami time series recorded at four nearby DART gauges, with little phase delay between the modeled tsunami arrival and the observed time series, and a consistent peak amplitude for the initial part of the tsunami, before the inclusions of coastal

reflections. Unlike other models, this result does not require the earthquake to rupture the near-trench region of the megathrust in order to fit the timing or magnitude of the observed tsunami. The incorporation of tsunami data into the inversion processes provides a useful dataset for constraining offshore slip in a region that is otherwise difficult to resolve through geodetic means. Consistent use of tsunami data, when available, for future earthquakes will allow for a clearer understanding of when there is and is not shallow slip on the megathrust. When applied, this data allows for a better assessment of the diverse tsunamigenic behavior of earthquakes along the Peru-Chile trench, but can also be included in studies of other seismically active regions.

CHAPTER 4. SUITABILITY FOR NEAR-FIELD TSUNAMI EARLY WARNING ALONG SEISMICALLY ACTIVE SUBDUCTION ZONES

4.1 Abstract

Over the past decade, the number of open-ocean gauges such as Deep-ocean Assessment and Reporting of Tsunami (DART) and cabled pressure networks has increased steadily through an international effort focusing on recording and transmitting information about passing tsunami. This information is analyzed to disseminate tsunami warnings to affected regions. However, most current warnings that incorporate tsunami data into the source determination are directed to mid and far-field localities. If placed efficiently, gauges deployed in the future could increase the temporal window for tsunami early warning at localities near the initial tsunami nucleation site. The addition of a direct observation of the tsunami reduces the possibility of a misestimate of the hazard at affected nearby communities. In this study we analyze the region surrounding four seismically active subduction zones for their potential to facilitate local tsunami early warning systems. We assess which locations currently have instrumentation in the right locations for direct tsunami observations with enough time to provide useful warning to the nearest affected coastline- and which are poorly suited for such systems. We take into account the effect of tsunami propagation with regard to shallow bathymetry on the fore-arc as well as the effect of earthquake source placement. While it is impossible to account for every type of seismicity or tsunamigenic behavior in every possible location along a subduction zone, this study aims to characterize a typical large tsunamigenic event occurring in the shallow

part of the megathrust as a guide in what is feasible with early tsunami warning. We illustrate that some of our study regions could potentially facilitate local tsunami early warning systems with the addition of only one or two new open-ocean gauges while other areas are poorly suited for early warning even if a dense coastal array were to be installed.

4.2 Introduction

Many tsunami warning centers evaluate the hazard of a tsunami through an assessment of the seismic energy released. Then, if available, additional data about the tsunami are incorporated to update mid and far-field tsunami warnings. While a seismic dataset is valuable for understanding the earthquake source dynamics, the relationship between the seismic energy determined earthquake magnitude and tsunami energy used for event warnings and forecasts is non-linear and poorly understood [*Tang et al.,* 2012]. Even with a well constrained seismically determined magnitude, the application to tsunami hazard is not always absolute. As highlighted in *Titov et al.* [2016a], the tsunami warnings issued for many recent earthquakes based on seismic evaluations did not accurately describe the oncoming wave. In the cases of the 2005 Nias Island earthquake (M_w 8.6) and the 2012 Sumatra earthquake (M_w 8.6), the tsunami threats were overestimated, leading to unnecessary and costly evacuations with little to no eventual damage related to the tsunami [*Song,* 2007]. On the other hand, in the cases of the 2006 West Java earthquake (M_w 7.7), no official tsunami warning was issued despite a run-up of up to 21 meters in Pangandaran [*Okal*, 2015; *Fritz et al.,* 2007]. This earthquake, like the 2010 Mentawai Islands earthquake (M_w 7.8), was a 'tsunami earthquake' [*Newman et al.,* 2011]. Tsunami earthquakes oftentimes produce tsunami that are much larger than seismic models rapidly predict [*Kanamori*, 1972; *Kanamori and Kikuchi,* 1993; *Newman & Okal,* 1998] with slip

concentrated in the shallow megathrust environment [*Polet & Kanamori*, 2000]. While seismic evaluations of the tsunami are valuable- particularly in the near-field where tsunami landfall can be within tens of minutes, a direct measurement of the tsunami for forecasting purposes provides a useful dataset for emergency management. Direct observations lessen the chance of a misestimate of the tsunami, which can be devastating for the near-field environments where the majority of tsunami victims are located [*Titov et al.,* 2016b].

Tsunami forecasts through the United States Tsunami Warning System rely on a series of pre-computed unit sources located along the tsunamigenic portion of the subduction zone coupled with computational models of coastal inundation [*Titov* 2009; *Titov et al.,* 2016b]. The incorporation of pre-computed unit sources as discrete Green's functions allows for computationally quick linear inversions to solve for the tsunami source coefficients, location [*Percival et al.,* 2011], and far-field forecasting, including coastal inundation. This is the basis of the Short-term Inundation for Tsunami (SIFT) framework [*Gica et al.,* 2008; *Titov* 2009]. Unit Sources are combined through a linear least-squares inversion and modified by slip coefficients to best fit the first period of direct tsunami observation with the smallest misfit [*Percival et al.,* 2011]. This approximation is useful for far-field forecasting where the tsunami wave is most sensitive to magnitude and location, while additional fault parameters have a lesser influence [*Titov et al.,* 2001]. In order to provide an informed warning to near-field regions, tsunami early warning would benefit from a direct measurement of a tsunami waveform at one or more gauges preceding the inundation of the nearest coastline. The direct tsunami measurement can be used in conjunction with pre-computed unit sources for rapid community scale warnings. This

direct measurement reduces the chance of a misestimate of the oncoming wave from a miscalculation of the earthquake source.

Unlike far-field warnings where source to arrival is on the scale of hours, near-field warnings need to be computed on a severely abbreviated timeframe. One potential aid is the travel time differential between the open-ocean and shallow coastal environments. In deep water, tsunami propagate with a relatively simple wave velocity that acts as a function of water column height. A tsunami will propagate with a higher velocity in deep water than it will over the shallower continental shelf. This discrepancy was identified for far-field tsunami forecasts in *Titov et al.* [2005] where the placement of sensors in the central Pacific allowed for the computation of lead times between measurement and inundation for the Hawaiian coastal city of Hilo. The efficacy of real-time open-ocean measurements of tsunami generated from far-field sources for forecasts in Hilo was demonstrated through idealized placements of then test-phase tsunameters. Idealized placements allowed for measurement and processing of the oncoming wave prior to inundation at the city- but focused solely on distantly generated events. This study operates under a similar premise as the *Titov et al.,* [2005] study, but with a focus on near-field, rather than far-field generated events over multiple regions where tsunameters could be placed.

After considerable attention on far-field inundation forecasts, near-field early warning is the latest frontier for tsunami warning systems [*Song* 2007; *Titov et al.,* 2016b]. Prior work has assessed the usage of coastal GPS and assimilation of Deep-Ocean Assessment and Reporting of Tsunami (DART) gauges for improved early warning by rapidly approximating tsunami energy [*Titov et al.,* 2016a]. With these prior works in mind, this paper analyzes the suitability for localized near-field tsunami warning systems

incorporating direct open-ocean tsunami observations, like DART. We focus on four seismically-active regions, highlighting unique characteristics to take into account for early warning systems including coastal morphology, subducting plate geometry, and tsunami source–to-landfall travel times. The goal of this study is not to reformat current warning system operations, but to provide a framework for the future possibilities of open-ocean data incorporation. For each region in this study, we analyze the usefulness of currently deployed instrumentation for the specific goal of tsunami early warning as well as highlight coastal areas that could benefit from a tsunami early warning system if new instrumentation were to be deployed in the future. Based on this study, our primary findings are that while some regions are ill-suited for this type of early warning, other localities could incorporate direct tsunami observations into their hazard forecasts with enough lead time to be effective for coastal community emergency response.

The study is divided into the following sections. First we outline currently deployed open-ocean instrumentation and its use in tsunami warning systems. Second we provide our methodology and analysis of the feasibility for localized near-field early warning for our four study regions- Cascadia, Japan, Indonesia, and Chile. Third, we discuss the variability of certain model parameters used in tsunami early warning and how they affect our results.

4.3 Data

Open-ocean pressure sensors provide the cleanest dataset that directly records the passage of tsunami waves. Within the past decade they have been incorporated in real time for tsunami warnings in the United States [*Titov et al.,* 2016b]. In the mid-1990s, the U.S.

National Tsunami Hazard Mitigation Program (NTHMP) led an effort to deploy a network of bottom pressure recorders for use as tsunameters (DART gauges) [*Mungov et al.*, 2013]. Each gauge measures the pressure exerted on a seafloor sensor from the overlying water column, translating it to a water column height. The gauges monitor for not only seismically induced tsunamis [*Wei et al.,* 2014], but also from non-seismic events such as landslide tsunamis and meteotsunamis. Currently there is a globally distributed array of over 60 DART gauges owned by a consortium of countries and managed through the National Data Buoy Center. Data on the water column height from each gauge are transmitted to warning centers via satellite and are openly available in semi-real time, offering a direct observation of a passing tsunami that is incorporated into tsunami warning forecasts. Most currently deployed gauges sit far from potential tsunami sources. Newer DART 4G instruments, which are in test operations offshore Oregon and Chile, are capable of up to a 1 Hz sampling frequency [*Rabinovich and Eble*, 2015; *Tang et al.,* 2016] and are deployed closer to the trench and potential tsunami sources.

It is important to note that DART gauges are not deployed with the goal of providing tsunami forecasts for the immediate near-field. Current station capabilities are tailored for mid- to far-field forecasting. Furthermore, DART gauges are not the only instruments available in the open-ocean for tsunami modeling. Cabled networks that include similar pressure gauge technology exist in a few locations. We highlight the deployment and capabilities of these observatories in subsequent sections of this paper. While this paper looks at near-field warnings using any open-ocean tsunami data, we use the current global distribution of DART as a reference point because of their ubiquity in tsunami modeling.

4.4 Methodology

The most important factor for an effective near-field tsunami warning is the time between tsunami generation and landfall. Immediately after generation, a tsunami will propagate radially. As the tsunami enters deep water, the wave velocity increases. In contrast, as a tsunami enters shallow coastal water, it slows down considerably. This discrepancy in velocity means over the same time frame, a tsunami will propagate a further distance into the open-ocean than it will towards the shoreline [*Titov et al.,* 2005]. With the right geometry, a tsunami can, in theory, be recorded at open-ocean sensors before it makes landfall. If the lead time between recording and landfall is sufficient, the data can be fruitful for early-warning. We focus on finding the locations with the greatest lead time between source and inundation as candidates for tsunami early warning systems.

In order to examine this lead time for a range of environments, we generate a series of discrete trench-parallel synthetic seafloor displacements. For each event, we track the travel time of the crest of the leading wave to determine the difference in travel time towards the open-ocean versus the shoreline (shown in Figure 1). The earliest arrival time of the tsunami at the shoreline is recorded and used to determine the open-ocean boundary of which a station must be placed in order to capture the first one-quarter of the leading wave prior to its coastal inundation. We then highlight zones inside this boundary where a station must be placed in order to record the tsunami with various amounts of lead time. The zones with the highest possible lead time allow for the most time that could be used for data processing and dissemination of tsunami early warnings. By combining the results of multiple sources along the strike of the subduction zone, we can generate a composite view for each of our four study regions, to look at which areas have zones that are ideal for early warning, and which regions inhibit such early forecasts. The sea-surface displacement

generated from each synthetic tsunami source is used as an initial condition for tsunami propagation. Each seafloor displacement is described as a two-dimensional curved surface defined by:

$$H = \frac{1}{4}\left(1 + \cos\left(\frac{\pi x}{L}\right)\right)\left(1 + \cos\left(\frac{\pi y}{L}\right)\right) \quad (6)$$

where L is the diameter of the source and H is the two-dimensional water column profile over a spatial domain governed by x and y [*Hossen et al.,* 2015]. Because we primarily are focusing on the tsunami propagation and the first arrival of the crest of the leading wave at both land and possible nearby receivers, the amplitude of the wave – which negligibly affects the wave velocity, is ignored. We place each of our synthetic sources above the region where we expect the subducting slab to be at 15 km depth using fault geometry estimated from Slab 1.0 [*Hayes et al.,* 2012]. The reasons for this placement are 1) this depth typically considered the upper extent of the seismogenic zone that generates large earthquakes [*Lay,* 2015]; 2) the combination of shallow slip and a deeper water column is preferential for tsunami generation when compared to shallow coastal environments; and 3) the shallow environment is close to what can be expected for tsunami earthquakes.

We model the propagating tsunami from each synthetic event over a regional spatial domain with a 1 arc minute bathymetry. For each synthetic event, we use a model time step of 2 seconds to satisfy the Courant-Friedrich-Levy condition for one hour of tsunami propagation-which in every instance is long enough to model the tsunami at its earliest

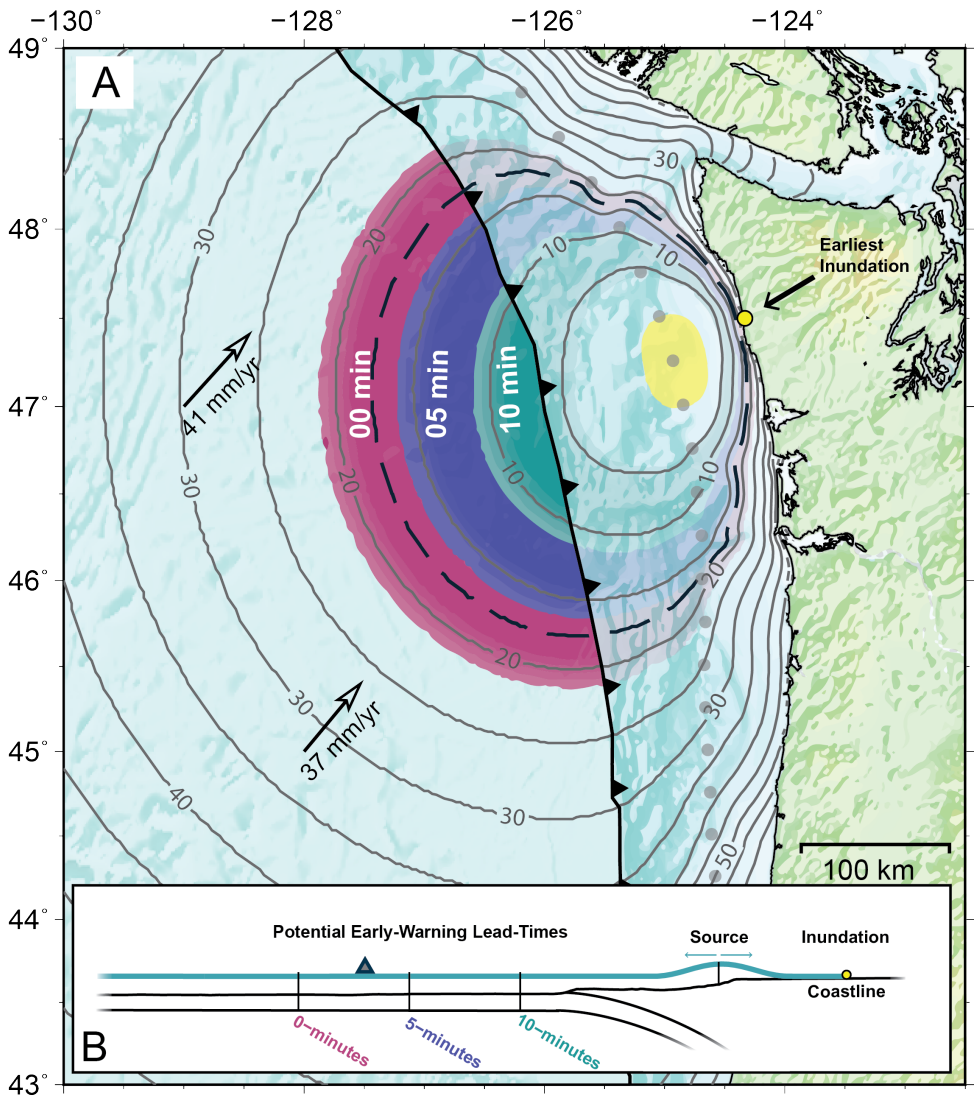

Figure 4.1. A. Propagation of a single synthetic event to determine instrument zones for local early tsunami warning. The synthetic event's source is shown as the light yellow polygon. The travel time, in minutes, of the crest of the leading wave from this source is plotted by the gray contours. The location of the earliest inundation (at 18 minutes) is marked with a yellow dot on the coastline. The location of the tsunami's leading wave at this time is outlined by the black dashed line. The magenta, navy, and aqua shaded regions on the subducting plate indicate 0-, 5-, and 10-minute zones for possible instrument placement. The gray dots along strike of the trench shows the rest of the synthetic locations that will be combined in the composite image (Figure 2). Arrows indicate the plate motion between the Juan de Fuca and North American plates using MORVEL-2010 motions [*DeMets et al.,* 2010]. **B.** Cross-section schematic of the source, inundation, and warning zones for near field tsunami early warning, generalizing the map shown in **A**.

instance of inundation. We run each simulation using the Method of Splitting Tsunami (MOST) model, a finite difference scheme that solves the non-linear shallow water wave equations [*Titov & González,* 1997]. It is currently an operational tool at the NOAA Tsunami Warning Centers and at the NOAA Center for Tsunami Research. The model is used for real-time tsunami forecasting and assessment using SIFT (Short-Term Inundation Forecast) [*Gica et al,* 2008; *Titov,* 2009; *Titov et al.,* 2016b].

An example of our analysis for early warning using a single synthetic source is shown in Figure 4.1. In this example, the earliest landfall of the crest of the leading wave, 18 minutes after nucleation, is recorded for determining instrument warning zones. The simultaneous location of the tsunami's leading wave in open-ocean identifies the furthest extent of the near-field early warning capabilities, or the 0-minute warning, acting as a threshold for instrument placement. The 0-minute warning region means any station placed in this shaded region will be measured at about the same time as landfall. To figure out the possible lead time of any other location for this synthetic event is fairly simple. The lead time amounts to the tsunami travel time subtracted from the earliest coastal arrival time. In this figure, we highlight zones that have 5 and 10 minutes of lead time before coastal inundation. For each of the subsequent composite figures, we draw shaded regions of expected lead times from 0 minutes up to 20 minutes at 5-minute increments, where possible.

It is extremely important to note that the location of our synthetic source has a role in the timing of the earliest inundation on land and this threshold of open-ocean detection. We pick our source location, as mentioned earlier, for its consideration as the 'edge' of the typical seismogenic zone. However, any event rupturing primarily up-dip of this synthetic

event will have a longer time until inundation, and events rupturing primarily down-dip will have a quicker inundation. We stress this variability and uncertainty in source location by creating a 2.5-minute window on either side of our lead-time estimate, as a way to take into account slightly shallower and slightly deeper events. Therefore, each lead time estimate, as shown in Figure 1, is displayed as a zone rather than a single definite line.

Figure 4.1 shows only a single-source solution to demonstrate the methodology, but each final composite image is composed of multiple synthetic events. The spacing of each of these synthetic events is 15' latitude and longitude. At an equatorial site this amounts to one synthetic source about every 30 km along strike. This spacing allows for the characterization of a region for its near-field warning capabilities rather than a focus on just one particular bay or feature. Regional early-warning images in subsequent figures combine many synthetic events into one composite. Each event is weighted equally, where the center of each lead time zone (treated as a polygon shape file) is assigned the value '1' and areas not in the warning zone are assigned a value of '0'. After all of the same lead time zones are combined into the composite and normalized to the number of events used per image, areas lower than a threshold value of 0.1 are discarded. This is to avoid the inclusion of spurious areas that may be considered ideal for only one event but are not ideal for neighboring events, and to smooth small irregularities in lead times. After the composite for each warning zone is created, a final image merges each warning zone together, as shown in Figures 4.2-4.6.

4.5 Results

The results of five composite images for four near-field tsunami warning cases are explored. Each region is picked due to either unique megathrust geometries, coastal morphology, the threat of a future large event, or the preponderance of large tsunamigenic events in the past. We focus entirely on subduction zone megathrust environments because of their tsunamigenic potential due to earthquakes and current open-ocean tsunami instrumentation.

4.5.1 Cascadia

Attention has been focused on the Cascadia subduction zone in recent years in preparation for the possibility of a great tsunamigenic earthquake rupturing along the trench [*Satake et al.,* 1996; *Satake et al.,* 2003]. The most recent large tsunami generated from the region occurred in 1700 A.D., supported from Japanese tsunami deposit records and tree ring analysis along the Pacific Northwest [*Satake et al.,* 1996; *Atwater*, 1992]. Estimated sources of the 1700 tsunami have been modeled to compare with Japanese coastal records, supporting a claim that the earthquake which generated the tsunami ruptured over 1100 km of the megathrust with a magnitude close to 9.0 [*Satake et al.,* 2003]. While the megathrust remains seismically quiet, the region is known for frequent slow-slip events near the deeper portion of the subduction interface [*Rogers & Dragert,* 2003]. Currently, with land-based tools, it is unclear if the shallower portion of this interface is locked, or freely slipping, giving little guidance to the seismic hazard. There have been many recent studies on this matter, producing many models of a possible large megathrust event. These models aid in our understanding of possible hazards associated from the tsunami, such as inundation extent, as well as seismic characteristics, such as

peak-ground-acceleration that could be expected on land [*Witter et al.,* 2013; *Melgar et al.,* 2016].

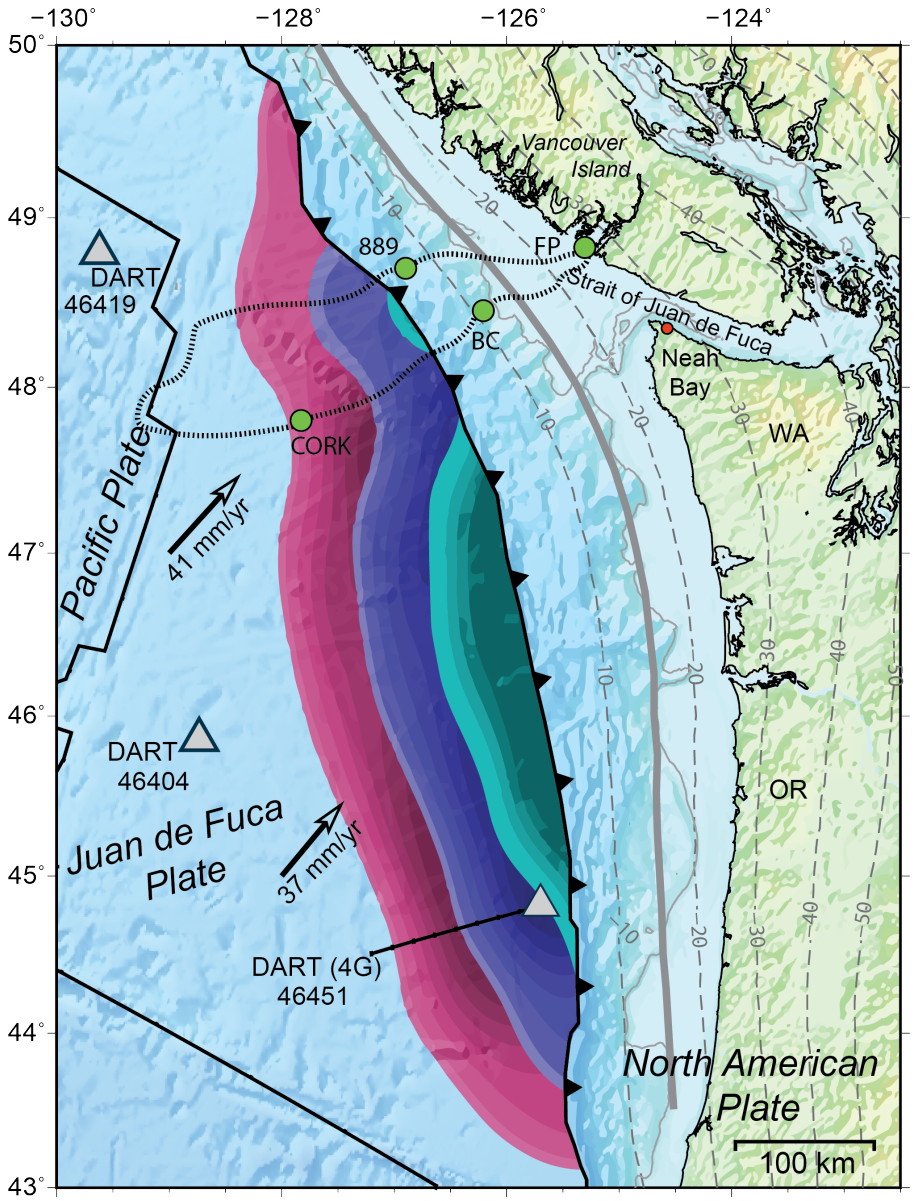

Figure 4.2. Composite view of Cascadia early warning zones. Magenta, navy, and aqua shading refer to 0 minute, 5-minute, and 10-minute lead times respectively. Arrows indicate the plate motion between the Juan de Fuca and North American plates using MORVEL-2010 motions [*DeMets et al.,* 2010], gray triangles show approximate locations of DART gauges, and green dots indicate the location of NEPTUNE bottom pressure sensors used for tsunami studies. The thick, gray line that runs trench parallel shows the location of synthetic sources used in the composite. Unlike subsequent figures, there are no recorded earthquakes greater than M 6 with a thrust focal mechanism to display to illustrate seismicity around the megathrust.

Building on the methodology example from Figure 4.1, Figure 4.2 shows the regional composite view of early warning for the Cascadia subduction zone in the Pacific Northwest. The young Juan de Fuca plate subducts underneath the North American plate at about 40 mm/yr [*DeMets et al.,* 2010]. The off-shore coastal region between the trench and coastline is fairly broad with distances that can exceed 100 km. The regional bathymetry includes a wide and broad continental shelf that extends far off the Oregon and Washington coastlines before tapering towards Vancouver Island and a thick sedimentary wedge extending from trench to shelf. This composite solution merges the warning zones from 22 synthetic trench-parallel events along the megathrust interface. The megathrust interface has a fairly shallow inferred dip, placing the synthetic event boundary close to the continental shelf. Each lead-time zone (0-, 5- and 10- minutes) highlighted in Figure 4.2 is composed by first determining the warning zone on each individual model, as shown in Figure 4.1.

The best zone for near-field deep-ocean instrumentation extends from 44.5° to 47.5° N where a 10-minute lead time is possible for local events. To the south of this zone, land extends further along the interface, precluding shallow earthquakes from displacing enough of the water column be tsunamigenic. Additionally, the continental shelf's width tapers, locally affecting the wave velocity. To the north, the mouth of the Strait of Juan de Fuca inhibits the shoaling and slowing of the tsunami, leading to a quicker inundation at the opening of the strait. Further north along Vancouver Island, the ability to include near-field open ocean datasets declines as the distance to the coast diminishes. Outside of the 10-minute warning, the 5-minute zone extends further towards the open ocean and can accommodate a wider region.

Localized, near-field tsunami early warning that uses direct tsunami observations in Cascadia are likely limited to this region highlighted in green on Figure 2. Areas to the south where the shelf tapers do not have the ability for such localized warnings if a rupture were to occur in the immediate vicinity. However, for regional events- such as a Cascadia rupture that is dominantly to the north on the megathrust, the zoning that allows for a feasible tsunami warning system grows substantially.

The Cascadian subduction zone is heavily instrumented and already has open-ocean stations that may be of use for near-field early warning. Three regional DART gauges are included in the composite image to illustrate current operational gauges (DART 46149 and DART 46404) and the DART 4G sensor (DART 46451) which is currently in a testing phase. The 4G gauge's currently deployed location has the ability to offer a larger lead time in warnings along the coast from Washington to Vancouver Island, than conventional DART, aiding in assessment and evacuation efforts. Instrumentation placed further north of DART 46451 in this same trench-proximal locality would be able to not only provide advanced warning to coastal regions in the Pacific Northwest, but also provide the same mid-and far-field assessments as the older model DART gauges.

In the past decade, the Canadian North-East Pacific Underwater Networked Experiments (NEPTUNE) deployed a cabled network that among other geophysical pursuits, transmits pressure data in real time and can be used for tsunami forecasting [*Barnes et al.,* 2013; *Rabinovich and Eble,* 2015]. The network sits on the accretionary prism offshore from Vancouver Island and provides an intermediate dataset between open-ocean sensors and coastal tide gauges. This network was tested as it recorded the passing of the tsunami generated from the 30 September 2009 Samoa earthquake (M_W 8.1) as it

propagated towards the coast of the Pacific Northwest [*Thomson et al*., 2011]. This additional cabled dataset provides useful near-field information that could be integrated into a local tsunami early warning program outside of the DART framework particularly for events affecting the northern portion of the subduction zone.

4.5.2 Japan

Japan has a strong tradition of tsunami science and hazard resilience, built through centuries of observing local and distantly generated tsunami. The linkage between strong shaking from an earthquake and coastal evacuation from an expected tsunami led to the creation of Japan's first tsunami warning center in 1941 [*Bernard and Titov*, 2015]. This first center in Sendai detected earthquakes to determine if evacuation was necessary in nearby coastal cities. The program was later expanded to all of Japan in 1952 [*Bernard & Titov*, 2015]. In addition to more characteristic megathrust earthquakes, the Japan trench has also hosted at least one tsunami earthquake in its past. The 1896 Sanriku tsunami earthquake caused extensive casualties due to a lack of perceived shaking on land [*Kanamori*, 1972]. The tsunami had estimates of 25- 38 m of run-up despite a surface wave-magnitude estimated at 7.0 [*Tanioka & Satake,* 1996; *Mori et al.,* 2011].

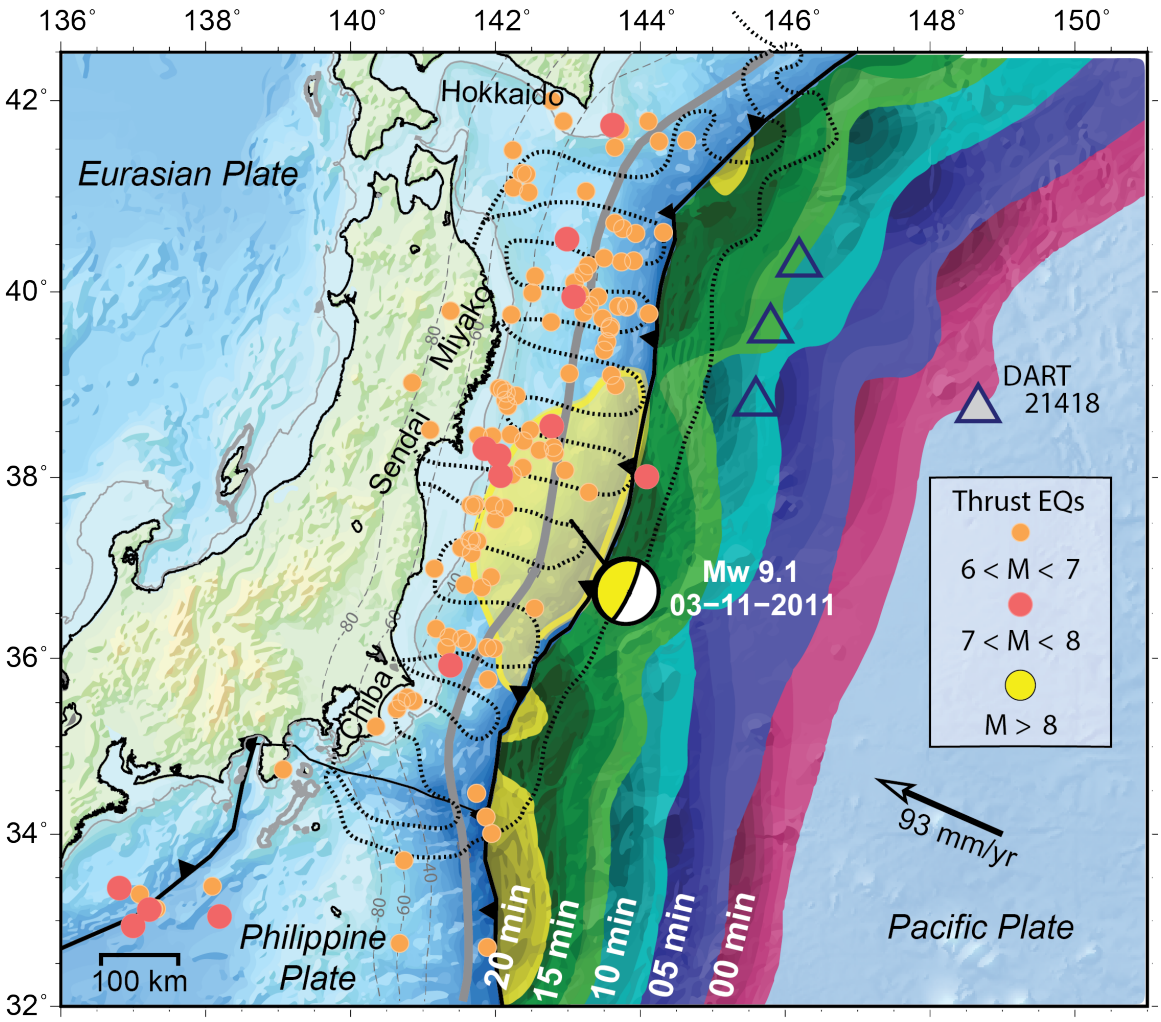

Figure 4.3. Composite view of northern Japan early warning zones. Magenta, navy, aqua, green, and yellow shading refer to 0 minute, 5-minute, 10-minute, 15-minute, and 20-minute lead times respectively. Arrows indicate the plate motion between the Pacific and Eurasian plates using MORVEL-2010 motions [*DeMets et al.,* 2010] and gray triangles show approximate locations of DART gauges. The thick, gray line that runs trench parallel shows the location of synthetic sources used in the composite. Small dots indicate seismicity recorded in the Harvard CMT catalog over the past 25 years. Yellow shaded region is the approximate rupture extent of the 11 March 2011 Tohoku earthquake [*Wei et al.,* 2014]. Hollow triangles indicate DART gauges deployed following the 2011 Tohoku tsunami but have since been decommissioned. Black dashed lines indicate the location of S-net.

Japan's tsunami warning program was put to test on March 11, 2011 during the devastating Tohoku-Oki earthquake and tsunami. The M_w 9.0 earthquake, rupturing at

14:46:24 local time was initially assessed as a M_w 7.9 [*Ozaki*, 2011; *Tang et al.,* 2012]. The Japanese Meteorological Agency (JMA) promptly issued a tsunami warning for nearby prefectures 3 minutes after the earthquake commenced. Then, W-phase estimates conducted by JMA 20 minutes after the event's onset confirmed that the earthquake was much larger- closer to a 9.0 [*Ritsema et al.,* 2011]. However, the first tsunami models of the event were not available during the initial tsunami warning, but rather were created an hour after the fact, once the tsunami reached the nearest open-ocean gauge [*Wei et al.,* 2014]. By this point, the first waves had already reached the coast and additional tsunami information was then put forth for tsunami forecasts for Hawaii and the far-field. It is also important to note this was the first tsunami to ever be modeled in real time for its far-field inundation hazard [*Titov et al.,* 2016b].

After the 2011 tsunami, three DART gauges were temporarily deployed off the coast of Japan. The more recent, but smaller 2012 M_w 7.3 Japan earthquake and tsunami benefited from the proximal DART gauges sitting closer to the trench, allowing for a shorter time between generation and observation [*Bernard et al.,* 2014]. While those three DART sensors have now been removed, a cabled network of 154 seafloor pressure gauges spanning the overriding plate, S-net has been completed [*Baba et al.,* 2014; *Rabinovich and Eble*, 2015]. This network's aim is to provide real-time pressure measurements to aid in tsunami warning. Another cabled-network, the Dense Ocean-floor Network for Earthquakes and Tsunamis (DONET-1 and DONET-2) is a cable network providing pressure gauges and seismometers on the overriding plate to aid in real-time tsunami detection and observation along the Nankai seismic zone [*Baba et al.,* 2014; *Rabinovich*

and Eble, 2015]. Combined, these networks have the possibility of capturing deformation and tsunami generation from locally sourced earthquakes.

Taking into account the plethora of pressure gauges on the overriding plate as well as nearby DART gauges, the Japan trench provides one of the best locations for the implementation of an early warning system, as shown in Figure 4.3. Nowhere else in the world has a network that approaches their offshore instrument density. Japan is already poised to provide rapid direct tsunami observations, possibly aiding in future event forecasts. Additionally, Japan's large distance between trench and coast (100 to 200 km) along most of the Pacific-Eurasian plate interface facilitates a greater area of potential site locations on the subducting plate than other regions. Even along some parts of the subduction zone, where the trench to shoreline distance is narrower, the presence of a shallow and expansive continental shelf can also effectively slow the oncoming wave, allowing for effective open-ocean instrumentation.

One of the best examples of this is near the Chiba peninsula, east of Tokyo, shown in Figure 4.3. The yellow shaded region offshore indicates the instrumentation zone for up to 20 minutes of lead time before inundation. The strong shelf south of Sendai also acts to curtail the tsunami wave. As a contrast, the tapering and disappearance of the shelf north of Sendai near Miyako leads to slightly less lead-time, about 15 minutes. Along the entire strike of the trench from Chiba peninsula to Hokkaido, a 10 to 15-minute lead time is possible.

4.5.3 Peru-Chile

Of the regions analyzed in this paper, the Peru-Chile trench poses the greatest challenge for near-field early warning. The region has a relatively fast plate convergence and a history of great ($M_W > 8$) tsunamigenic earthquakes. The 1960 Valdivia earthquake and tsunami originating off the coast of Southern Chile is the largest instrumentally recorded earthquake (M_W 9.5) generating a trans-oceanic tsunami with local maximum run-up heights ranging from 10-25m [*NDBC*, 2017]. Southern Chile has been fairly quiet in the decades since, with the exception of the December 2016 M_w 7.7 Chiloé earthquake, which ruptured within the 1960 rupture zone [*Ruiz et al.,* 2017]. Additional contemporary earthquakes include the 2010 M_w 8.8 Maule earthquake and the 2014 M_w 8.1 Iquique earthquake, both of which generated tsunami. The most recent addition to the Peru Chile trench sequence is the 2015 M_w 8.3 Illapel earthquake and tsunami. All three of these recent events have included open-ocean DART derived waveforms in conjunction with seismic and/or geodetic observations for detailed analysis of the fault slip post-event, either through timeseries inversion [*Yue et al.,* 2014; *Gusman et al.,* 2015; *Williamson et al.,* 2017] or forward tsunami modeling for model validation [*Heidarzadeh et al.,* 2016; *Li et al.,* 2016]. However, the capability of real-time near field modeling has not yet been explored in great detail.

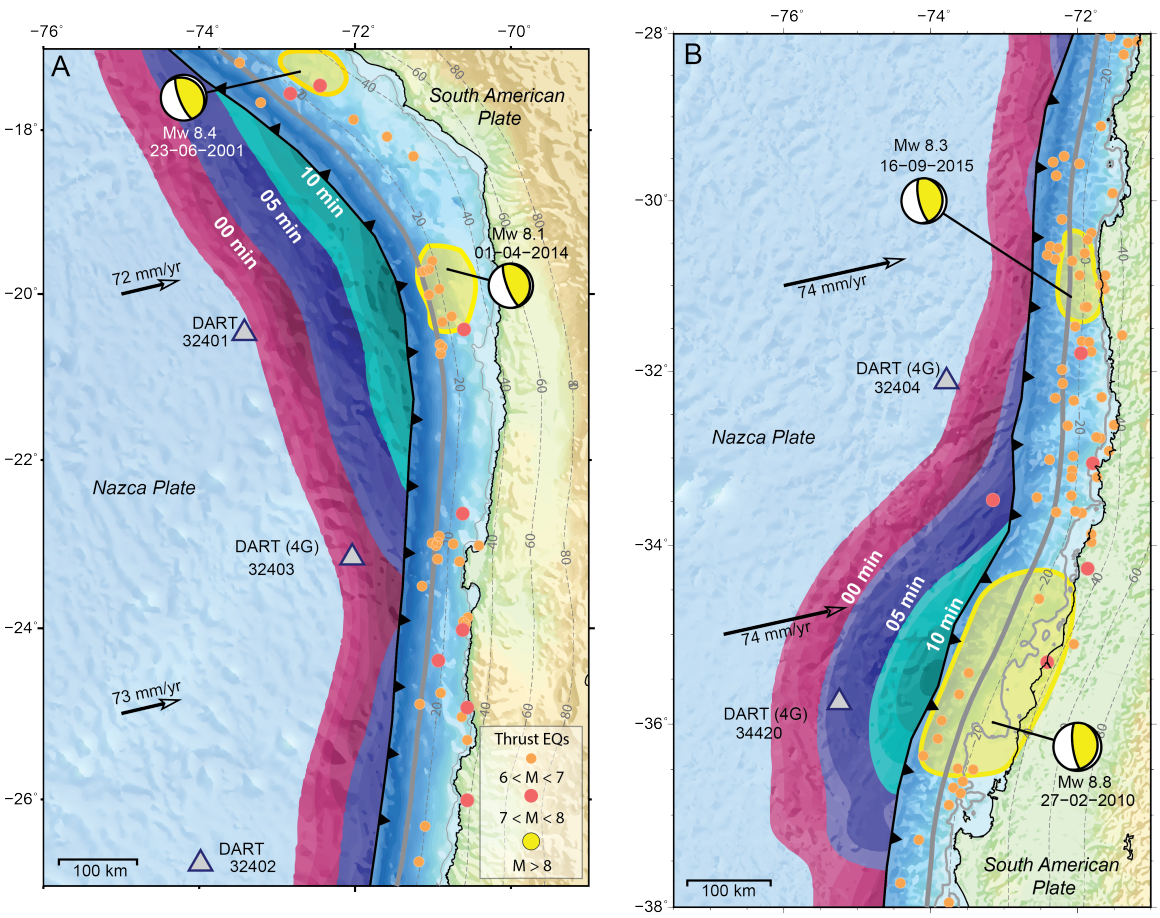

Figure 4.4. Composite view of northern and central Chile early warning zones. Magenta, navy, and aqua shading refer to 0 minute, 5-minute, and 10-minute lead times respectively. Arrows indicate the plate motion between the Nazca and South American plates using MORVEL-2010 motions [*DeMets et al.*, 2010] and gray triangles show approximate locations of DART gauges. The thick, gray line that runs trench parallel shows the location of synthetic sources used in the composite. Small dots indicate seismicity recorded in the Harvard CMT catalog over the past 25 years. A) **Northern Peru-Chile trench: yellow polygons show rupture zones from the 23 June 2001 Peru earthquake [*Bilek and Ruff,* 2002] and the 1 April 2014 Iquique earthquake [*Lay et al.*, 2014].** B) **Central Peru-Chile trench: yellow polygons show rupture zones from the 27 February 2010 Maule earthquake [*Moreno et al.*, 2010] and 16 September 2015 Illapel earthquake [*Williamson et al.*, 2017].**

Near-field instrumentation feasibility for this region is displayed in Figure 4.4. Unlike Cascadia and Japan, the average distance between trench and coastline is small at under 75

km. This shortens the response time before inundation as it places the shallow seismic interface close to shore. The linear coastal morphology with limited and narrow continental shelves does not slow the coastal tsunami propagation as it does elsewhere. Most of the trench only has 5 minutes or less in lead time, which exceptions near the bend in the subduction zone around the rupture area near the Iquique tsunami, and further south in the former Maule rupture area. This makes most of the region prohibitive of open-ocean early-warning. However, the narrow submarine zone means this area is more advantageous for the inclusion of geodetic datasets to aid in early warning.

The Chilean agency that oversees tsunami data and warnings, the Hydrographic and Oceanic Service of the Chilean Navy (SHOA), has deployed three DART 4G gauges in the near-trench environment. The southernmost gauge, DART 34420- is within a 5-minute warning range, however the gauge immediately to the north (DART 32404), placed just south of the Illapel rupture zone is in the 0-minute warning zone. The third gauge, located just south of the Iquique rupture zone, while close to the trench, is also just out of range. It is important to note that these three new sensors, even if not currently suited for direct near-field warning, will provide more open ocean tsunami observations along the strike of the Peru-Chile trench. Before their emplacement, the entire region was served by three older DART sensors (DARTs 32402, 32401, and 32412) located in northern Chile and more distal sensors near Ecuador and Central America. The inclusion of this new dataset, while not ideal for near-field community warnings, could be instrumental in warnings along Chile's extensive coastline outside of the near-field range. The array of DART gauges also provides a useful dataset for far-field warnings affecting Australia and New Zealand.

4.5.4 Java-Bali

Acting as a catalyst for a global approach to tsunami awareness and forecasting, the 2004 Sumatra earthquake illuminated the possibility of large megathrust earthquakes and tsunami generated in the Indian Ocean basin. Additional M > 8 earthquakes have continued to rupture along the southern extent of Sumatra in the years following the 2004 Boxing Day event. Despite their large magnitude, not every large earthquake in the region has generated a hazardous tsunami, making warnings more difficult. Examples include the 2005 Nias earthquake (M_W 8.6). This event, while generating a tsunami that did damage some coastal communities, did not bring the impact that would have been expected of an earthquake rupturing in this region- given the recent 2004 Boxing day earthquake [*Song,* 2007; *Borrero et al.,* 2011]. The distinction between hazardous and non-hazardous activity can be difficult to quickly determine remotely without a direct observation. In addition to being a tectonically active and complex region, half of Indonesia's population resides on the island of Java. The region surrounding Java has not had a great megathrust rupture in recent history but it has had smaller, damaging tsunami earthquakes.

The 1994 Java tsunami earthquake (M_W 7.6) killed over 250 people and was the first thrust mechanism earthquake listed along that region of the Java subduction zone [*Abercrombie et al.,* 2001]. It occurred between 16 and 20 km depth (highlighted in Figure 5) at a far distance from the shoreline. The more recent 2006 Pangandaran tsunami earthquake (M_W 7.8) killed over 600 people. It was particularly deadly because the earthquake was not well felt on land, limiting the reaction time for communities to evacuate from the coastline [*Fritz et al.,* 2008; *Ammon et al.,* 2006]. Both events are rarities- the region produces a high number of normal faulting earthquakes which were less productive

in generating tsunami (however tsunami can be generated from normal faulting events). However, the uncommon occurrence of large thrust events- particularly tsunamigenic events, may give communities a false sense of security up until the next earthquake hits.

The region spanning westward from Java towards Bali poses a difficult challenge for some early warning methodologies. The distance from possible shallow source to land-based receivers is high (> 200 km) and the dip of the subducting plate is steep enough that the entirety of the expected seismogenic zone sits offshore, with megathrust interface depths under land reaching upwards of 80 km. This distance poses a far more difficult challenge when using static geodetic (GPS, InSAR) datasets to resolve deformation and tsunami threat than when compared to other regions, such as the Peru-Chile trench. However, this large distance also increases the travel time between source and shoreline for shallow events making it an excellent candidate for tsunami early warning. The region offshore of Pangandaran, just east of the 1996 tsunami earthquake has the opportunity for a near field tsunami warning system that could be fortuitous for central Java. Synthetic unit

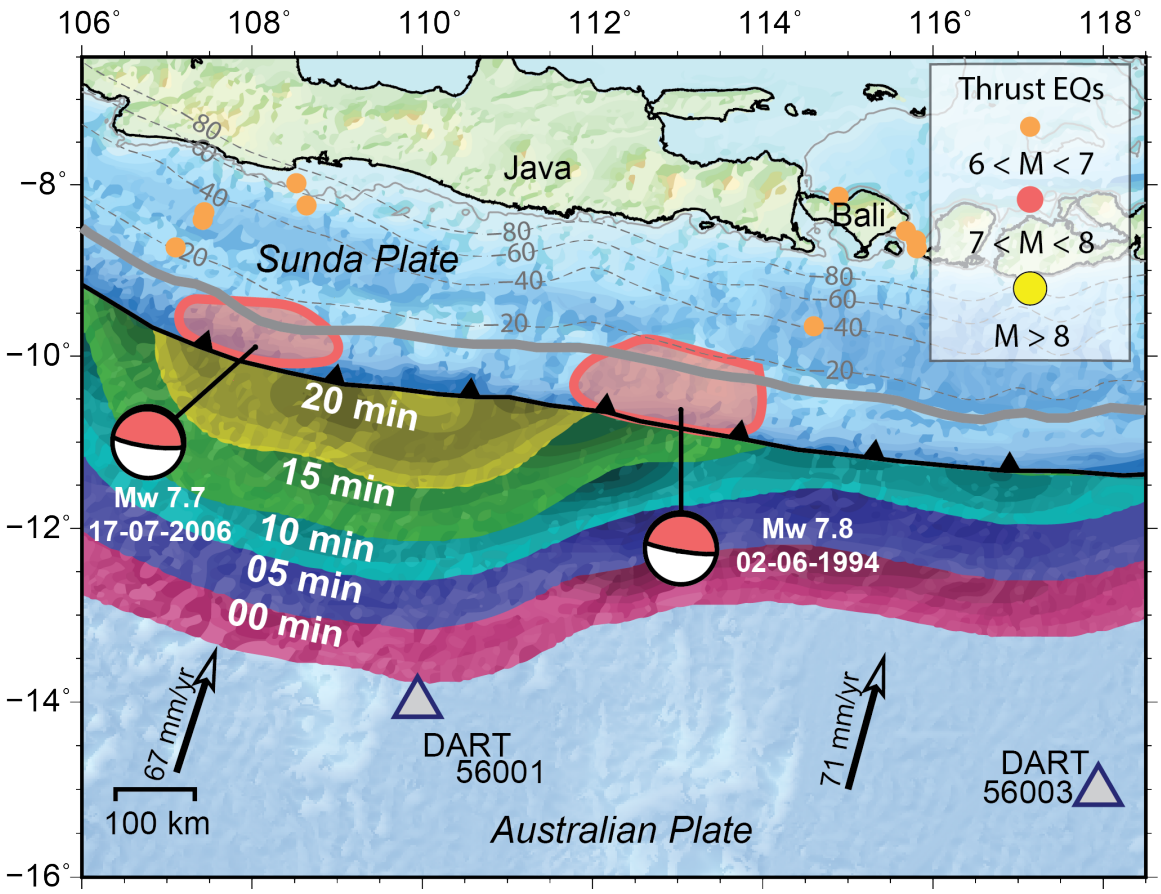

Figure 4.5. Composite view of Java early warning zones. Magenta, navy, aqua, green, and yellow shading refer to 0 minute, 5-minute, 10-minute, 15-minute, and 20-minute lead times respectively. Arrows indicate the plate motion between the Australian and Sunda plates using MORVEL-2010 motions [DeMets et al., 2010] and gray triangles show approximate locations of DART gauges. The thick, gray line that runs trench parallel shows the location of synthetic sources used in the composite. Small dots indicate seismicity recorded in the Harvard CMT catalog over the past 25 years. Pink polygons show the rupture extents from the 2 June 1994 Java tsunami earthquake [*Bilek and Engdahl,* 2007] and the 17 July 2006 Pangandaran tsunami earthquake [*Ammon et al.*, 2006].

sources in this region line-up well with past tsunami earthquakes (Figure 4.5). Within central Java, open-ocean datasets could allow for up to 15-20 minutes of lead time. The main factor that allows for tsunami early warning to be more feasible along central Java and less feasible further east towards Bali is the increase in continental shelf width near Pangandaran. The absence of shallow coastal structures offshore Bali and the rest of the

Lesser Sunda Islands increases tsunami arrival time in comparison. Current instrumentation is limited to two Australian owned DART stations (DART 56001 and 56003). These gauges are located too far to be effective for Indonesian early warning.

Unlike other regions examined in this study where the eventual open-ocean propagation of the tsunami remains unhindered for thousands of kilometers, a near-field tsunami warning system for this region adds additional information that can be used to issue warnings for the nearby northwestern shores of Australia. In the event of a larger tsunami stemming from a large Sumatra-style megathrust earthquake, additional infrastructure beyond Australia's two local DART gauges could provide a quicker initial assessment for the country's northern coastline.

4.6 Discussion

Because the location and structure of the next big earthquake is unknown, global models used for assessing tsunami hazard always need to take into account what model assumptions are made. In this paper, two of the biggest assumptions are in the synthetic event source location and the amount of data that can be efficiently incorporated. The tsunami source location has the largest effect on tsunami travel time. One end member scenario for tsunami early warning is an event rupturing proximal to the coastline with an immediate or close to immediate inundation. The other end member (for megathrust events) is a near-trench rupture typical of tsunami earthquakes. Rather than make a judgement call on the potential future tsunamigenic sources for each of our study zones, we adopted a streamlined approach of placing all of our sources at the 15 km depth contour of the subducting slab's assumed geometry. While some may argue that a particular region

usually ruptures in a certain location, the earthquake catalog of large megathrust events is not so well defined in any given area over time that we can definitively point to a local characteristic earthquake that can be confidently used for modeling future hazard. Our general assumed events allows us to focus on the early-warning potential for the region of the megathrust that has a high tsunami hazard. For the same magnitude of slip, the shallow environment is more productive in deforming the seafloor and nucleating a tsunami than at greater depths. The near-trench environment is also less likely to be resolved form coastal geodetic datasets, lending to the threat of misestimates of tsunami hazard in special tsunami earthquake cases.

We recognize that not all tsunamigenic events occur on the megathrust. Our general source location used for all our regional models also is placed in a way that we can extrapolate the effect of splay faulting on the fore-arc by focusing less on the features any particular faulting pattern and more on the tsunami travel time for a simple disturbed water column. However, steeply dipping splay faults, if activated, have the potential to contribute to large amounts of vertical deformation of the seafloor as has been extrapolated for the Nankai trough [*Moore et al.,* 2007]. Splay faults of this nature, located in the accretionary wedge, have also been identified along the Cascadia subduction zone although their future activity is difficult to constrain [*Geist and Yoshioka,* 1996]. Tsunami generated on the outer-rise, while also less common, poses a threat for tsunami warning. Recent outer-rise events include 2007 Kuril M_w 8.1 event [*Fujii and Satake*, 2008; *Rabinovich et al.,* 2008]. The greater distance between outer rise sources and most coastlines when compared to megathrust events means an extended time before inundation is likely. This should facilitate some of the greatest lead times possible for early warning. Other sources not

considered in this work include non-seismically generated tsunamis- the most common of which are landslide generated tsunami. Without a strong seismic signature or magnitude to relate to, landslide generated tsunami require a direct tsunami observation for an effective tsunami warning.

A second important factor to consider for early-warning feasibility is the timely assimilation of observed data into forecast models. This is dependent on how much data is used. In this study we use the first one-quarter of a tsunami waveform as our threshold for data incorporation. While this is a smaller amount of data than what is currently used to forecast tsunami warnings, the extra error associated with less data is at the trade-off of a quicker warning to affected communities when time is a restricting factor. The use of one-quarter wave periods was assessed for the 2015 Illapel, Chile tsunami with the goal of determining the minimum quantity of open-ocean data required for the earliest possible accurate tsunami forecast [*Tang et al.,* 2016]. In this study, the use of the first one-quarter of the recorded waveform was effectively inverted to determine a source model that could be applied for near-field early warning forecasts. This is an abbreviation of the half-wave model [*Titov et al.,* 2016b], which can also be used and yields a slight improvement to fit. The full-wave inversion provides additional unique information, but only a marginally better forecast at the expense of a longer wait time between source and final recording.

The amount of data used in a rapid inversion also affects the processing required. When handling data derived from the open-ocean, tidal signals need to be removed to provide a meaningful dataset. The uncertainty involved in de-tiding datasets should be low enough that a reasonable forecast can still be made. In *Percival et al.,* [2015], the de-tiding of tsunami signals is assessed with synthetic data to view the degree of error from using

different filtering methods as well as differing quantities of data. An important takeaway from the study is that while the best results are attained by using over one full wavelength of data, methodologies that incorporated only one-quarter of the wavelength did as sufficient of a job at resolving the unknown slip parameters as half- and three-quarter wavelength solutions. While, like *Tang et al.,* [2016] showed, the best possible solutions are attained with the most data, the increased time needed did not substantially change the final results. In terms of early warning, a slight change in the forecast solution at the cost of tens of minutes of warning time may not always be substantiated.

An additional factor that has been omitted from the work thus far is commentary on the cost of deploying new instrumentation in the open-ocean. The deployment and maintenance on any instrument, including ship-time for servicing can be substantial. We do not focus on the deployment logistics of adding new stations further as it is outside the scope of this paper. As mentioned in *Bernard and Titov* [2015] approximated costs of new DART stations can reach $0.5 million per station. Cabled observatories, like those found in Japan have a starting cost of $500 million for the entire network. We do note that by focusing on which regions can facilitate early-warnings, we can reduce the total number of stations that would need to be deployed to be as cost-effective as possible.

4.7 Conclusion

Through this study, we explore four regions to examine where a localized near-field tsunami system would be effective. Ideally this system would incorporate near-trench, open-ocean, tsunami observations, through pressure gauges such as the currently deployed

DART system or through cabled pressure stations. The advantages of direct tsunami measurements over seismic and geodetically focused approaches are listed below:

1. Tsunami datasets do not rely on the accuracy of an earthquake magnitude. This can be particularly important for tsunami earthquakes and large earthquakes with long rupture durations.
2. Using tsunami datasets negates the need to understand exactly the relationship between the transfer of earthquake energy to tsunami energy. This is crucial, because estimates in earthquake energy can vary greatly in the first hour after rupture and so little of that energy (0.1%) is transferred to the ocean [*Titov et al.,* 2016a].
3. Tsunami waveforms can directly observe the oncoming threat for forecasting models without making assumptions on the fault geometry.
4. Recordings of tsunami data incorporate non-seismic contributions to the tsunami wave such as submarine mass failures. As *Bernard and Titov* [2015] have noted- 20% of tsunamis are generated from non-seismic sources.

The main limitation to this direct observation approach is having enough instrumentation to cover high-risk areas near the trench. This is both a resource and financial limitation. If newer DART systems or comparable open-ocean datasets prove robust and yield fruitful tsunami information despite strong shaking from the earthquake, regions like the Cascadia subduction zone are viable for near-field tsunami warning. Other regions, such as proximal to Java, Indonesia, do not have the near-field infrastructure but could benefit from an early warning of this variety- particularly due to their contemporary history of tsunami earthquakes. Chile, while having near-trench open-ocean tsunami data,

is poorly suited for local early warning, given its subducting fault geometry and prohibitive continental shelf geometry. However, those observations are still useful for mid-field warnings within the Peru-Chile trench.

Based on this study, our primary findings are that while some regions are ill-suited for this type of early warning, other localities could incorporate direct tsunami observations into their hazard forecasts with enough lead time to be effective for coastal community emergency response. Particular coastal areas with associated high potential tsunami lead times could have a localized system which may require only one to two open-ocean stations.

We do not advocate to dismantle or delay current tsunami warnings and advisories already in place and rooted in public knowledge for coastal communities. However, the vast majority of tsunami victims are located in the near-field coastal areas. Improvements on near-field tsunami warnings can save lives [*Titov et al.,* 2016a]. The inclusion of additional tsunami data can create an added push for further evacuation if needed in the case of underestimations of the perceived hazard. It can also add confidence to accurate warnings already in place and act as an additional data set for mid- and far-field forecasts.

REFERENCES

Abercrombie, R.E., Antolik M., Felzer K., and Ekström G. (2001), The 1994 Java tsunami earthquake: Slip over a subducting seamount. *Journal of Geophysical Research: Solid Earth*, *106*(B4), pp.6595-6607. doi: 10.1029/2000JB900403

Adriano, B., Y. Fujii, S. Koshimura, E. Mas, A. Ruiz-Angulo, M. Estrada (2018), Tsunami Source Inversion Using Tide Gauge and DART Tsunami Waveforms of the 2017 Mw8. 2 Mexico Earthquake, *Pure and Applied Geophysics*, 1-14. Doi: 10.1007/s00024-017-1760-2

Allgeyer, S., & Cummins, P. (2014). Numerical tsunami simulation including elastic loading and seawater density stratification. *Geophysical Research Letters*, *41*(7), 2368-2375.

Ammon, C.J., Kanamori H., Lay T., and Velasco A.A. (2006), The 17 July 2006 Java tsunami earthquake. *Geophysical Research Letters*, *33*(24). doi: 10.1029/2006GL028005

An, C., I. Sepúlveda, PLF. Liu (2014), Tsunami source and its validation of the 2014 Iquique, Chile Earthquake, *Geophys. Res. Lett.*, 41, 3988–3994, doi:10.1002/2014GL060567.

Atwater, B.F., (1992), Geologic evidence for earthquakes during the past 2000 years along the Copalis River, southern coastal Washington. *Journal of Geophysical Research: Solid Earth*, *97*(B2), pp.1901-1919. doi: 10.1029/91JB02346

Atzori, S., A. Antonioli (2011), Optimal fault resolution in geodetic inversion of coseismic data, *Geophysical Journal International*, *185*(1), 529-538, doi: 10.1111/j.1365-246X.2011.04955.x.

Baba, T., Takahashi N., and Kaneda Y. (2014), Near-field tsunami amplification factors in the Kii Peninsula, Japan for Dense Oceanfloor Network for Earthquakes and Tsunamis (DONET). *Marine Geophysical Research*, 35(3), pp:319-325. doi:10.1007/s11001-013-9189-1

Baba, T., N. Takahashi, Y. Kaneda, K. Ando, D. Matsuoka, T. Kato (2015), Parallel implementation of dispersive tsunami wave modeling with a nesting algorithm for the 2011 Tohoku Tsunami. *Pure and Applied Geophysics* 172.12: 3455-3472.

Barnes, C. R., Best, M. M., Johnson, F. R., Pautet, L., and Pirenne, B. (2013), Challenges, benefits, and opportunities in installing and operating cabled ocean observatories: Perspectives from NEPTUNE Canada. *IEEE Journal of Oceanic Engineering*, *38*(1), 144-157.

Barnhart, W. D., R. B. Lohman (2010), Automated fault model discretization for inversions for coseismic slip distributions, *Journal of Geophysical Research: Solid Earth*, *115*(B10). Doi: 10.1029/2010JB007545

Benavente, R, PR. Cummins, J Dettmer (2016), Rapid automated W-phase slip inversion for the Illapel great earthquake (2015, Mw= 8.3). *Geophys. Res. Lett.,* 43.5: 1910-1917.

Beresnev, I. A. (2003). Uncertainties in finite-fault slip inversions: to what extent to believe? (a critical review). *Bulletin of the Seismological Society of America*, *93*(6), 2445-2458. Doi: https://doi.org/10.1785/0120020225

Bernard, E. N., H. O. Mofjeld, V. Titov, C. E. Synolakis, F. I. González, F. I. (2006), Tsunami: scientific frontiers, mitigation, forecasting and policy implications. *Philosophical Transactions of the Royal Society of London A: Mathematical, Physical and Engineering Sciences*, *364*(1845), 1989-2007.

Bernard, E. N., & Meinig, C. (2011, September). History and future of deep-ocean tsunami measurements. In *OCEANS 2011* (pp. 1-7). IEEE.

Bernard, E.N., Wei Y., Tang L., Titov V.V. (2014), Impact of near-field, deep-ocean tsunami observations on forecasting the 7 December 2012 Japanese tsunami, *Pure and Applied Geophysics*, 171(12), pp:3483-3491. doi:10.1007/s00024-013-0720-8

Bernard, E.N. and Titov V.V. (2015), Evolution of tsunami warning systems and products, *Philosophical Transactions of the Royal Society A* 373, no. 2053: 20140371.

Bilek, S.L. and T. Lay (1999), Rigidity variations with depth along interplate megathrust faults in subduction zones. *Nature*, 400(6743), pp.443-446.

Bilek, S. L., and Ruff L. J. (2002), Analysis of the 23 June 2001 M*w* = 8.4 Peru underthrusting earthquake and its aftershocks, *Geophysical Research Letters*, 29(20), 1960, doi:10.1029/2002GL015543.

Bilek, S. L., and Engdahl E. R. (2007), Rupture characterization and aftershock relocations for the 1994 and 2006 tsunami earthquakes in the Java subduction zone, *Geophysical Research Letters*, 34, L20311, doi:10.1029/2007GL031357.

Bird, P., and Y. Y. Kagan (2004) Plate-tectonic analysis of shallow seismicity: Apparent boundary width, beta, corner magnitude, coupled lithosphere thickness, and coupling in seven tectonic settings, *Bull. Seismol. Soc. Am.*, *94*(6), 2380-2399

Blewitt, G., Kreemer, C., Hammond, W. C., Plag, H. P., Stein, S., & Okal, E. (2006). Rapid determination of earthquake magnitude using GPS for tsunami warning systems. *Geophysical Research Letters*, *33*(11).

Blewitt, G. (2015). GPS and space-based geodetic methods.

Borrero, J. C., McAdoo, B., Jaffe, B., Dengler, L., Gelfenbaum, G., Higman, B., ... and Prasetya, G. (2011), Field survey of the March 28, 2005 Nias-Simeulue earthquake and tsunami. *Pure and applied geophysics*, *168*(6-7), 1075-1088.

Bourgeois, J., C. Petroff, H. Yeh, V. Titov, C.E. Synolakis, B. Benson, J. Kuroiwa, J. Lander, E. Norabuena (1999), Geologic Setting, Field Survey and Modeling of the Chimbote, Northern Peru, Tsunami of 21 February 1996. In *Seismogenic and Tsunamigenic Processes in Shallow Subduction Zones* (pp. 513-540). Birkhäuser Basel. doi:10.1007/s000240050242

Calisto, I., M. Miller, and I. Constanzo (2016), Comparison between tsunami signals generated by different source models and the observed data of the Illapel 2015 earthquake. *Pure and Applied Geophysics*, 173.4: 1051-1061.

Chadwick Jr, W. W., S. L. Nooner, D. A. Butterfield, and M. D. Lilley (2012). Seafloor deformation and forecasts of the April 2011 eruption at Axial Seamount, *Nature Geoscience 5*, (*7)*: 474-477.

Chen, T., A. V. Newman, L, Feng, H. M. Fritz (2009), Slip Distribution from the 1 April 2007 Solomon Islands Earthquake: A Unique Image of Near-Trench Rupture, *Geophys. Res. Lett.*, 36, L16307, doi:10.1029/2009GL039496.

Convers, J. A., A. V. Newman (2011), Global Evaluation of Large Earthquake Energy from 1997 Through mid-2010, *J. Geophys. Res*., 116, B08304, doi:10.1029/2010JB007928.

Crowell, B. W., Bock, Y., & Melgar, D. (2012). Real-time inversion of GPS data for finite fault modeling and rapid hazard assessment. *Geophysical Research Letters*, *39*(9).

DeMets, C., Gordon R.G., and Argus D.F. (2010), Geologically current plate motions. *Geophysical Journal International*, 181(1), pp.1-80. doi: 10.1111/j.1365-246X.2009.04491.x

Ekström, G., M. Nettles, A.M. Dziewoński (2012), The global CMT project 2004–2010: centroid-moment tensors for 13,017 earthquakes. *Physics of the Earth and Planetary Interiors*, 200, pp.1-9. doi:10.1016/j.pepi.2012.04.002

Feng, L., Newman, A. V., Protti, M., Gonzalez, V., Jiang, Y., & Dixon, T. H. (2012). Active deformation near the Nicoya Peninsula, northwestern Costa Rica, between 1996 and 2010: Interseismic megathrust coupling. *Journal of Geophysical Research: Solid Earth*, *117*(B6).

Fritz, H.M., Kongko W., Moore A., McAdoo B., Goff J., Harbitz C., Uslu B., Kalligeris N., Suteja D., Kalsum K., and Titov V. (2007), Extreme runup from the 17 July 2006 Java tsunami. *Geophysical Research Letters*, *34*(12). doi: 10.1029/2007GL029404

Fritz, H.M., C.M. Petroff, P.A. Catalán, R. Cienfuegos, P. Winckler, N. Kalligeris, R. Weiss, S.E. Barrientos, G. Meneses, C. Valderas-Bermejo, C. Ebeling (2011). Field survey of the 27 February 2010 Chile tsunami. *Pure and Applied Geophys*ics, 168(11), pp.1989-2010. doi: 10.1007/s00024-011-0283-5

Fujii, Y., & Satake, K. (2008), Tsunami sources of the November 2006 and January 2007 great Kuril earthquakes. *Bulletin of the Seismological Society of America*, *98*(3), 1559-1571.

Fujii, Y., Satake, K., Sakai, S. I., Shinohara, M., & Kanazawa, T. (2011). Tsunami source of the 2011 off the Pacific coast of Tohoku Earthquake. *Earth, planets and space*, *63*(7), 55.

Funning, G. J., B. Parsons, T. J. Wright (2007), Fault slip in the 1997 Manyi, Tibet earthquake from linear elastic modelling of InSAR displacements. *Geophysical Journal International*, *169*(3), 988-1008. Doi: 10.1111/j.1365-246X.2006.03318.x

Gagnon, K., C. D. Chadwell, and E. Norabuena (2005), Measuring the onset of locking in the Peru-Chile trench with GPS and acoustic measurements, Nature, 434(7030), 205-208, doi:http://dx.doi.org/10.1038/nature03412.

Geist, E., & Yoshioka, S. (1996), Source parameters controlling the generation and propagation of potential local tsunamis along the Cascadia margin. *Natural Hazards*, *13*(2), 151-177.

Geist, E.L., and R. Dmowska (1999), Local tsunamis and distributed slip at the source: *Pure and Applied Geophysics*, v. 154, p. 485-512.

Gica, E., Spillane M.C., Titov V.V., Chamberlin C.D., and Newman J.C. (2008), Development of the Forecast Propagation Database for NOAA's Short-Term Inundation Forecast for Tsunamis(SIFT).

González, F.I., Bernard E.N., Meinig C., Eble M.C., Mofjeld H.O., and Stalin S. (2005), The NTHMP tsunameter network *Natural Hazards 35* (1),25-39.

Grandin, R., E. Klein, M. Métois, C. Vigny (2016), Three-dimensional displacement field of the 2015 *Mw*8.3 Illapel earthquake (Chile) from across- and along-track Sentinel-1 TOPS interferometry, *Geophys. Res. Lett.,* 43, 2552–2561, doi:10.1002/2016GL067954.

Gusman, A. R., Y. Tanioka, T. Kobayashi, H. Latief, and W. Pandoe (2010), Slip distribution of the 2007 Bengkulu earthquake inferred from tsunami waveforms and InSAR data, *J. Geophys. Res., 115*, B12316, doi:10.1029/2010JB007565.

Gusman, A.R., Murotani S., Satake K., Heidarzadeh M., Gunawan E., Watada S., and Schurr B. (2015), Fault slip distribution of the 2014 Iquique, Chile, earthquake estimated from ocean-wide tsunami waveforms and GPS data, *Geophysical Research Letters,* 42(4), pp: 1053-1060. doi: 10.1002/2014GL062604.

Gusman, A. R., Mulia, I. E., & Satake, K. (2018). Optimum sea surface displacement and fault slip distribution of the 2017 Tehuantepec earthquake (Mw 8.2) in Mexico estimated from tsunami waveforms. *Geophysical Research Letters*. Doi: 10.1002/2017GL076070

Harris, R. A., P. Segall (1987), Detection of a locked zone at depth on the Parkfield, California, segment of the San Andreas Fault*, J. Geophys. Res*., 92(B8), 7945–7962, doi:10.1029/JB092iB08p07945.

Hayes, G.P., Wald D. J., and Johnson R.L. (2012), Slab1.0: A three-dimensional model of global subduction zone geometries*, Journal of Geophysical Research,* 117, B01302, doi:10.1029/2011JB008524.

Hayes, G. P., M.W. Herman, W.D. Barnhart, K.P. Furlong, S. Riquelme, H.M. Benz, E. Bergman, S. Barrientos, P. S. Earle, S. Samsonov (2014), Continuing megathrust earthquake potential in Chile after the 2014 Iquique earthquake, *Nature*, 512(7514), 295–298, doi:10.1038/nature13677.

Heidarzadeh, M., Murotani S., Satake K., Ishibe T., and Gusman A.R. (2016), Source model of the 16 September 2015 Illapel, Chile, M_w 8.4 earthquake based on

teleseismic and tsunami data, *Geophysical Research Letters*., 43, 643–650, doi:10.1002/2015GL067297.

Heinrich, P., F. Schindele, S. Guibourg, P.F. Ihmlé, 1998. Modeling of the February 1996 Peruvian tsunami. *Geophysical research letters*, 25(14), pp.2687-2690.

Hobbs, T. E., Kyriakopoulos, C., Newman, A. V., Protti, M., & Yao, D. (2017). Large and primarily updip afterslip following the 2012 Mw 7.6 Nicoya, Costa Rica earthquake. *Journal of Geophysical Research: Solid Earth*.

Hossen, M. J., Cummins P.R., Dettmer J., and Baba T. (2015), Time reverse imaging for far-field tsunami forecasting: 2011 Tohoku earthquake case study, *Geophysical Research Letters,* 42, 9906–9915, doi:10.1002/2015GL065868.

Hsu, Y.J., M. Simons, J.P. Avouac, J. Galetzka, K. Sieh, M. Chlieh, D. Natawidjaja, L. Prawirodirdjo, Y. Bock (2006). Frictional afterslip following the 2005 Nias-Simeulue earthquake, Sumatra. *Science*, 312(5782), pp.1921-1926. DOI: 10.1126/science.1126960

Jónsson, S., H. Zebker, P. Segall, F. Amelung (2002). Fault slip distribution of the 1999 Mw 7.1 Hector Mine, California, earthquake, estimated from satellite radar and GPS measurements. *Bulletin of the Seismological Society of America*, 92(4), pp.1377-1389.

Kajiura, K. (1963) The Leading Wave of a Tsunami, *Bulletin of the Seismological Society of America*.

Kanamori, H., (1972), Mechanism of tsunami earthquakes. *Physics of the earth and planetary interiors*, *6*(5), pp.346-359. doi: 10.1016/0031-9201(72)90058-1

Kanamori, H., and Kikuchi M. (1993), The 1992 Nicaragua earthquake: a slow tsunami earthquake associated with subducted sediments, *Nature* 361(6414), pp:714-716. doi:10.1038/361714a0

Kyriakopoulos, C., A. V. Newman (2016), Structural asperity focusing locking and earthquake slip along the Nicoya megathrust, Costa Rica, *Journal of Geophysical Research: Solid Earth*, *121*(7), 5461-5476. Doi: 10.1002/2016JB012886

Lay, T., Yue H., Brodsky E.E., and An C. (2014), The 1 April 2014 Iquique, Chile, M_w 8.1 earthquake rupture sequence, *Geophysical Research Letters,* 41, 3818–3825, doi:10.1002/2014GL060238.

Lay, T.,(2015), The surge of great earthquakes from 2004 to 2014, *Earth and Planetary Science Letters,* 409, pp: 133-146, doi: 10.1016/j.epsl.2014.10.047

Lee, S.J., T.Y. Yeh, T.C. Lin, Y.Y. Lin, T.R. Song, B.S. Huang (2016), Two-stage composite megathrust rupture of the 2015 M_w8.4 Illapel, Chile, earthquake identified by spectral-element inversion of teleseismic waves, *Geophys. Res. Lett*., 43, doi:10.1002/2016GL068843.

Li, J., Abers, G. A., Kim, Y., & Christensen, D. (2013). Alaska megathrust 1: Seismicity 43 years after the great 1964 Alaska megathrust earthquake. *Journal of Geophysical Research: Solid Earth*, *118*(9), 4861-4871.

Li, L., Lay T., Cheung K.F., and Ye L. (2016), Joint modeling of teleseismic and tsunami wave observations to constrain the 16 September 2015 Illapel, Chile, M_w 8.3 earthquake rupture process, *Geophysical Research Letters*, 43, 4303–4312, doi:10.1002/2016GL068674

Lorito, S., F. Romano, S. Atzori, X. Tong, A. Avallone, J. McCloskey, M. Cocco, E. Boschi, A. Piatanesi (2011), Limited overlap between the seismic gap and coseismic slip of the great 2010 Chile earthquake, *Nature*, 4(3), 173–177, doi:10.1038/ngeo1073.

Luttrell, K. M., Tong, X., Sandwell, D. T., Brooks, B. A., & Bevis, M. G. (2011). Estimates of stress drop and crustal tectonic stress from the 27 February 2010 Maule, Chile, earthquake: Implications for fault strength. *Journal of Geophysical Research: Solid Earth*, *116*(B11).

Malservisi, R., Schwartz, S.Y., Voss, N., Protti, M., Gonzalez, V., Dixon, T.H., Jiang, Y., Newman, A.V., Richardson, J., Walter, J.I. and Voyenko, D., 2015. Multiscale postseismic behavior on a megathrust: The 2012 Nicoya earthquake, Costa Rica. Geochemistry, Geophysics, Geosystems, 16(6), pp.1848-1864. doi:10.1002/2015GC005794.

McCaffrey, R., Qamar, A. I., King, R. W., Wells, R., Khazaradze, G., Williams, C. A., ... & Zwick, P. C. (2007). Fault locking, block rotation and crustal deformation in the Pacific Northwest. *Geophysical Journal International*, *169*(3), 1315-1340.

Meinig, C., Stalin, S. E., Nakamura, A. I., & Milburn, H. B. (2005). Real-time deep-ocean tsunami measuring, monitoring, and reporting system: The noaa dart ii description and disclosure. *NOAA, Pacific Marine Environmental Laboratory (PMEL)*, 1-15.

Melgar, D., LeVeque, R.J., Dreger, D.S., and Allen, R.M. (2016), Kinematic rupture scenarios and synthetic displacement data: An example application to the Cascadia subduction zone. *Journal of Geophysical Research: Solid Earth*, *121*(9), 6658-6674.

Melgar, D., W. Fan, S. Riquelme, J. Geng, C. Liang, M. Fuentes, et al., (2016), Slip segmentation and slow rupture to the trench during the 2015, Mw8. 3 Illapel, Chile earthquake, *Geophysical Research Letters*, *43*(3), 961-966. Doi: 10.1002/2015GL067369

Menke, W. (1989), Geophysical Data Analysis: Discrete Inverse Theory, Academic, San Diego, Calif.

Métois, M., Socquet, A., & Vigny, C. (2012). Interseismic coupling, segmentation and mechanical behavior of the central Chile subduction zone. *Journal of Geophysical Research: Solid Earth*, *117*(B3).

Métois, M., Vigny, C., & Socquet, A. (2016). Interseismic coupling, megathrust earthquakes and seismic swarms along the Chilean subduction zone (38–18 S). *Pure and Applied Geophysics*, *173*(5), 1431-1449.

Moore, G. F., Bangs, N. L., Taira, A., Kuramoto, S., Pangborn, E., and Tobin, H. J. (2007), Three-dimensional splay fault geometry and implications for tsunami generation. *Science*, *318*(5853), 1128-1131.

Moreno, M., Melnick, D., Rosenau, M., Baez, J., Klotz, J., Oncken, O., ... & Socquet, A. (2012). Toward understanding tectonic control on the Mw 8.8 2010 Maule Chile earthquake. *Earth and Planetary Science Letters*, *321*, 152-165.

Moreno, M., D. Melnick, M. Rosenau, J. Bolte, J. Klotz, H. Echtler, J. Baez, K. Bataille, J. Chen, M. Bevis, H. Hase (2011). Heterogeneous plate locking in the South–Central Chile subduction zone: Building up the next great earthquake. *Earth and Planetary Science Letters,* 305(3), pp.413-424. doi:10.1016/j.epsl.2011.03.025

Moreno, M., Rosenau M., and Oncken O. (2010), 2010 Maule earthquake slip correlates with pre-seismic locking of Andean subduction zone. *Nature*, *467*(7312), p.198. doi: 10.1038/nature09349

Mori, N., Takahashi T., Yasuda T., Yanagisawa H. (2011), Survey of 2011 Tohoku earthquake tsunami inundation and run-up, *Geophysical Research Letters,* 38(7), doi: 10.1029/2011GL049210

Mungov, G., Eblé, M., and Bouchard, R. (2013), DART tsunameter retrospective and real-time data: A reflection on 10 years of processing in support of tsunami research and operations. *Pure and Applied Geophysics*, *170*(9-10), 1369-1384.

National Geophysical Data Center database (NGDC). https://www.ngdc.noaa.gov. (accessed: 15.05.16); (accessed: 19.09.17)

Newman, AV., and Okal E.A. (1998), Teleseismic estimates of radiated seismic energy: The E/M 0 discriminant for tsunami earthquakes, *Journal of Geophysical Research: Solid Earth,* 103(B11), pp: 26885-26898, doi: 10.1029/98JB02236

Newman, A.V., Hayes G., Wei Y., and Convers J. (2011), The 25 October 2010 Mentawai tsunami earthquake, from real-time discriminants, finite-fault rupture, and tsunami excitation. *Geophysical Research Letters*, *38*(5). doi: 10.1029/2010GL046498

Newman, A. V., L. Feng, H. M. Fritz, Z. M. Lifton, N. Kalligeris, and Y. Wei (2011), The Energetic 2010 M_W 7.1 Solomon Islands Tsunami Earthquake *Geophys. Journ. Int.*, 186 (2), 775–781, doi:10.1111/j.1365-246X.2011.05057.x.

Newman, A. V. (2011). Hidden depths. *Nature,* 474(7352), 441-443. doi:10.1038/474441a

Nishimura, T., Munekane, H., & Yarai, H. (2011). The 2011 off the Pacific coast of Tohoku Earthquake and its aftershocks observed by GEONET. *Earth, planets and space*, *63*(7), 22.

Okada, Y., (1985). Surface deformation due to shear and tensile faults in a half-space. *Bulletin of the seismological society of America,* 75(4), pp.1135-1154.

Okal, E.A. (2015), The quest for wisdom: lessons from 17 tsunamis, 2004–2014, *Philosophical Transactions of the Royal Society A,* 373(2053), *doi*: 10.1098/rsta.2014.0370

Olson, A. H., R.J. Apsel, R. J. (1982), Finite faults and inverse theory with applications to the 1979 Imperial Valley earthquake. *Bulletin of the Seismological Society of America*, *72*(6A), 1969-2001.

Ozaki, T. (2011), Outline of the 2011 off the Pacific coast of Tohoku Earthquake (M w 9.0). *Earth, planets and space*, *63*(7), 57.

Page, M. T., S. Custódio, R. J. Archuleta, J. M. Carlson (2009), Constraining earthquake source inversions with GPS data: 1. Resolution-based removal of artifacts, *Journal of Geophysical Research: Solid Earth*, *114*(B1). Doi: 10.1029/2007JB005449

Percival, D.B., Denbo D.W, Eblé M.C., Gica E., Mofjeld H.O., Spillane M.C., Tang L., and Titov V.V (2011), "Extraction of tsunami source coefficients via inversion of DART buoy data." *Natural hazards* 58, no. 1, 567-590.

Percival, D. B., Denbo, D. W., Eblé, M. C., Gica, E., Huang, P. Y., Mofjeld, H. O., ... & Tolkova, E. I. (2015). Detiding DART® buoy data for real-time extraction of source coefficients for operational tsunami forecasting. *Pure and Applied Geophysics*, *172*(6), 1653-1678.

Plafker, G. & Savage, J.C. (1970), Mechanism of the Chilean Earthquakes of May 21 and 22, 1960, *Geol. Soc. Am. Bull*., 81, 1001–1030.

Polet, J., and Kanamori H. (2000), Shallow subduction zone earthquakes and their tsunamigenic potential. *Geophysical Journal International*, *142*(3), pp.684-702. doi: 10.1046/j.1365-246x.2000.00205.x

Pollitz, F. F., Brooks, B., Tong, X., Bevis, M. G., Foster, J. H., Bürgmann, R., ... & Campos, J. (2011). Coseismic slip distribution of the February 27, 2010 Mw 8.8 Maule, Chile earthquake. *Geophysical Research Letters*, *38*(9).

Protti, M., González, V., Newman, A. V., Dixon, T. H., Schwartz, S. Y., Marshall, J. S., ... & Owen, S. E. (2014). Nicoya earthquake rupture anticipated by geodetic measurement of the locked plate interface. *Nature Geoscience*, *7*(2), 117.

Rabinovich, A. B., Lobkovsky, L. I., Fine, I. V., Thomson, R. E., Ivelskaya, T. N., & Kulikov, E. A. (2008). Near-source observations and modeling of the Kuril Islands tsunamis of 15 November 2006 and 13 January 2007. *Advances in Geosciences*, *14*, 105-116.

Rabinovich, A. B. and Eblé, M. C. (2015), Deep-ocean measurements of tsunami waves. *Pure and Applied Geophysics*, *172*(12), 3281-3312.

Ritsema, J., Lay, T., and Kanamori, H. (2012), The 2011 Tohoku Earthquake. *Elements*, *8*(3), 183-188.

Rogers, G., and Dragert H. (2003), Episodic tremor and slip on the Cascadia subduction zone: The chatter of silent slip, *Science,* 300(5627), pp: 1942-1943. doi: 10.1126/science.1084783

Romano, F., A. Piatanesi, S. Lorito, N. D'agostino, K. Hirata, et al (2012), Clues from joint inversion of tsunami and geodetic data of the 2011 Tohoku-oki earthquake, *Scientific reports*, *2*, 385. Doi: 10.1038/srep00385

Ruiz, S., Moreno, M., Melnick, D., Campo, F., Poli, P., Baez, J. C., Leyton F., and Madariaga, R. (2017), Reawakening of large earthquakes in South-Central Chile: The 2016 Mw7. 6 Chiloé event. *Geophysical Research Letters*.

Satake, K. (1987). Inversion of tsunami waveforms for the estimation of a fault heterogeneity: Method and numerical experiments. *Journal of Physics of the Earth*, *35*(3), 241-254.

Satake, K., (1994). Mechanism of the 1992 Nicaragua tsunami earthquake. *Geophysical Research Letters*, 21(23), pp.2519-2522.

Satake, K., Shimazaki K., Tsuji Y., and Ueda K. (1996), Time and size of a giant earthquake in Cascadia inferred from Japanese tsunami records of January 1700, *Nature* 379(6562), pp:246-249, doi: 10.1038/379246a0

Satake, K., Wang K., and Atwater B.F. (2003), Fault slip and seismic moment of the 1700 Cascadia earthquake inferred from Japanese tsunami descriptions, *Journal of Geophysical Research: Solid Earth*, 108(B11), doi: 10.1029/2003JB002521

Schurr, B., Asch, G., Hainzl, S., Bedford, J., Hoechner, A., Palo, M., Wang, R., Moreno, M., Bartsch, M., Zhang, Y. and Oncken, O., (2014). Gradual unlocking of plate boundary controlled initiation of the 2014 Iquique earthquake. *Nature*, 512(7514), pp.299-302. doi:10.1038/nature13681

Schmalzle, G. M., McCaffrey, R., & Creager, K. C. (2014). Central Cascadia subduction zone creep. *Geochemistry, Geophysics, Geosystems*, *15*(4), 1515-1532.

Simons, M., Fialko, Y., & Rivera, L. (2002). Coseismic deformation from the 1999 M w 7.1 Hector Mine, California, earthquake as inferred from InSAR and GPS observations. *Bulletin of the Seismological Society of America*, *92*(4), 1390-1402.

Simons, M., & Rosen, P. A. (2015). Interferometric synthetic aperture radar geodesy.

Song, Y.T. (2007), Detecting tsunami genesis and scales directly from coastal GPS stations, *Geophysical Research Letters,* 34(19), doi: 10.1029/2007GL031681

Tang, L., Titov, V. V., Moore, C., and Wei, Y. (2016), Real-time assessment of the 16 September 2015 Chile tsunami and implications for near-field forecast. *Pure and Applied Geophysics*, *173*(2), 369-387.

Tang, L., Titov, V. V., Bernard, E. N., Wei, Y., Chamberlin, C. D., Newman, J. C., et al. (2012), Direct energy estimation of the 2011 Japan tsunami using deep-ocean pressure measurements. *Journal of Geophysical Research: Oceans*, *117*(C8).

Tanioka, Y., and Sataka K. (1996), Fault parameters of the 1896 Sanriku tsunami earthquake estimated from tsunami numerical modeling

Thomson, R., Fine I., Rabinovich A., Mihály S., Davis E., Heesemann M., and Krassovski M. (2011), Observation of the 2009 Samoa tsunami by the NEPTUNE-Canada cabled observatory: Test data for an operational regional tsunami forecast model, *Geophysical Research Letters*, 38, L11701, doi:10.1029/2011GL046728.

Tilmann, F., Y. Zhang, M. Moreno, J. Saul, F. Eckelmann, M. Palo, Z. Deng, A. Babeyko, K. Chen, J.C. Baez, B. Schurr, R. Wang, T. Dahm (2016) The 2015 Illapel earthquake, central Chile: A type case for a characteristic earthquake? Geophysical Research Letters, 43, 574-583, doi:10.1002/2015GL066963.

Titov, V.V. C.E. Synolakis (1998). Numerical modeling of tidal wave run-up. *Journal of Waterway, Port, Coastal, and Ocean Engineering,* 124(4), pp.157-171.

Titov, V.V. and González F.I. (1997). Implementation and testing of the method of splitting tsunami (MOST) model. US Department of Commerce, National Oceanic and Atmospheric Administration, Environmental Research Laboratories, Pacific Marine Environmental Laboratory.

Titov, V.V., Mofjeld H.O., González F.I., and Newman J.C. (2001), Offshore forecasting of Alaskan tsunamis in Hawaii, In *Tsunami Research at the End of a Critical Decade*, pp. 75-90. Springer Netherlands.

Titov, V., Rabinovich, A. B., Mofjeld, H. O., Thomson, R. E., & González, F. I. (2005). The global reach of the 26 December 2004 Sumatra tsunami. *Science*, *309*(5743), 2045-2048.

Titov, V. V. (2009), Tsunami Forecasting//The Sea. Vol. 15/eds. EN Bernard and AR Robinson.

Titov, V.V., Song Y.T., Tang L., Bernard E.N., Bar-Sever Y., and Wei Y. (2016a), Consistent estimates of tsunami energy show promise for improved early

warning, *Pure and Applied Geophysics* 173(12), pp: 3863-3880, doi: 10.1007/s00024-016-1312-1

Titov, V.V., Kânoğlu U., and Synolakis C. (2016b), *Development of MOST for real-time tsunami forecasting*. Diss. American Society of Civil Engineers. doi:10.1061/(ASCE)WW.1943-5460.000035703116004

Vigny, C., A. Rudloff, J.C. Ruegg, R. Madariaga, J. Campos, J. M. Alvarez (2009), Upper plate deformation measured by GPS in the Coquimbo Gap, Chile. *Physics of the Earth and Planetary Interiors,* 175(1), pp.86-95. doi:10.1016/j.pepi.2008.02.013

Wang, K., Hu, Y., & He, J. (2012). Deformation cycles of subduction earthquakes in a viscoelastic Earth. *Nature*, *484*(7394), 327.

Watada, S., S. Kusumoto, K. Satake (2014), Traveltime delay and initial phase reversal of distant tsunamis coupled with the self-gravitating elastic Earth, *Journal of Geophysical Research: Solid Earth* 119.5: 4287-4310.

Wei, Y., Cheung, K. F., Curtis, G. D., & McCreery, C. S. (2003). Inverse algorithm for tsunami forecasts. *Journal of waterway, port, coastal, and ocean engineering*, *129*(2), 60-69.

Wei, Y., Newman A.V., Hayes G.P., Titov V.V., and Tang L. (2014), Tsunami forecast by joint inversion of real-time tsunami waveforms and seismic or GPS data: application to the Tohoku 2011 tsunami, *Pure and Applied Geophysics* 171(12), pp: 3281-3305, doi: 10.1007/s00024-014-0777-z

Wessel, P., Smith W.H.F., Scharroo R., Luis J.F., and Wobbe F. (2013), Generic Mapping Tools: Improved version released, *EOS Trans. AGU*, 94, 409-410

Williamson, A., Newman A.V., and Cummins P.R. (2017), Reconstruction of coseismic slip from the 2015 Illapel earthquake using combined geodetic and tsunami waveform data, *Journal of Geophysical Research: Solid Earth*, 122(3), pp:2119-2130, doi: 10.1002/2016JB013883

Witter, R. C., Zhang, Y. J., Wang, K., Priest, G. R., Goldfinger, C., Stimely, L., English J.T., and Ferro, P. A. (2013), Simulated tsunami inundation for a range of Cascadia

Ye, L., T. Lay, H. Kanamori, KD Koper (2016), Rapidly estimated seismic source parameters for the 16 September 2015 Illapel, Chile M w 8.3 earthquake. *Pure and Applied Geophysics* 173.2: 321-332.

Ye, L., T. Lay, Y. Bai, K. F. Cheung, H. Kanamori (2017), The 2017 Mw 8.2 Chiapas, Mexico, Earthquake: Energetic Slab Detachment, *Geophysical Research Letters*, *44*(23). Doi: 10.1002/2017GL076085

Yin, J., H. Yang, H. Yao, H. Weng (2016), Coseismic radiation and stress drop during the 2015M_w 8.3 Illapel, Chile megathrust earthquake, *Geophys. Res. Lett.,* 43, 1520–1528, doi:10.1002/2015GL067381.

Yoshimoto, M., Watada, S., Fujii, Y., & Satake, K. (2016). Source estimate and tsunami forecast from far-field deep-ocean tsunami waveforms—The 27 February 2010 Mw 8.8 Maule earthquake. *Geophysical Research Letters*, *43*(2), 659-665.

Yue, H., Lay T., Rivera L., An C., Vigny C., Tong X., and Báez Soto J.C. (2014), Localized fault slip to the trench in the 2010 Maule, Chile Mw= 8.8 earthquake from joint inversion of high-rate GPS, teleseismic body waves, InSAR, campaign GPS, and tsunami observations, *Journal of Geophysical Research: Solid Earth* 119(10), pp: 7786-7804. doi: 10.1002/2014JB011340

Yue, H., Lay, T., Li, L., Yamazaki, Y., Cheung, K. F., Rivera, L., ... & Muhari, A. (2015). Validation of linearity assumptions for using tsunami waveforms in joint inversion of kinematic rupture models: Application to the 2010 Mentawai Mw 7.8 tsunami earthquake. *Journal of Geophysical Research: Solid Earth*, *120*(3), 1728-1747.